Self-consistent interaction of fast particles and ICRF waves in 3D applications of fusion plasma devices.

PAR

Jonathan Marc Philippe FAUSTIN

EPFL

ÉCOLE POLYTECHNIQUE
FÉDÉRALE DE LAUSANNE

Suisse
2017

Ti ash i koup gro bwa.
– Proverbe créole réunionnais.

Abstract

Tokamaks and stellarators are the most promising reactor concepts using the magnetic confinement to contain the plasma fuel. Reactors capable of sustaining deuterium-tritium (D-T) fusion reactions requires the confinement of a very high temperature plasma (above 100 millions kelvin). In addition to external heating methods, the slowing down of α particles (helium-4 nuclei) born from D-T fusion reactions on the background plasma represents a significant source of plasma heating. The good confinement of fast particles is therefore one of the most important aspect of magnetic fusion devices. Furthermore, long plasma operation in future fusion reactors requires the control of inherent plasma instabilities. These instabilities are particularly dangerous in tokamaks because of the large plasma current necessary to establish the confining magnetic field. In this thesis we use the numerical code package SCENIC to study the application of Ion Cyclotron Range of Frequency (ICRF) waves to tokamak and stellarator devices. This numerical tool was built to self-consistently solve, in three dimensional configurations, the plasma magnetohydrodynamic (MHD) equilibrium, the ICRF wave propagation and the resonant ion distribution function. SCENIC is used to interpret how the sawtooth instability can be controlled in tokamaks by appropriate application of ICRF waves. This control method was successfully tested in the JET tokamak and it is foreseen to be applied in the future ITER tokamak. Such plasma degrading instabilities are not, however, expected in stellarators because they operate with no plasma current. The recently started stellarator Wendelstein 7-X (W7-X) must however prove experimentally that fast particles can be confined in an optimised quasi-isodynamic magnetic configuration. An efficient auxiliary source of fast ions is required in W7-X since it is not designed to procude α particles via D-T fusion reactions. In this thesis, we address the possibility of generating a significant fast ion population with ICRF waves in W7-X. SCENIC simulations are employed in order to identify relevant fast ion loss channels that may still exist in the W7-X quasi-omnigenous equilibrium. These simulations show that ICRF minority heating may not be suitable for producing fast ions in W7-X plasmas. It is found that a high energy tail is more likely to be developed if a three-ion species scheme is applied.

Key words: Ion-Cyclotron Range of Frequency waves, minority heating, three-ion species scheme, fast particle generation, magnetic confinement, stellarator, quasi-isodynamicity, loss channels.

Résumé

Les concepts les plus prometteurs de réacteurs à fusion utilisant le confinement magnétique du plasma sont les tokamak et stellarator. Des réacteurs capable d'entretenir des réactions de fusion de type deutérium-tritium (D-T) doivent pouvoir confiner des plasmas à très haute température (au-delà de 100 millions de kelvin). Des méthodes de chauffage auxiliaires peuvent être appliquées mais le ralentissement sur les ions et les électrons du plasma des particules α (noyaux d'atomes d'helium-4 produits par les réactions de fusion D-T) représente une source cruciale de chauffage du plasma. Le confinement des particules rapides est par conséquent l'un des aspects essentiels de la viabilité des réaction à fusion par confinement magnétique. De plus, le fonctionnement des futurs réacteurs à fusion sur de longues durée requiert le contrôle des instabilités inhérentes au plasma. Ces instabilités sont d'autant plus nombreuses dans les plasmas de tokamak en raison du très fort courant plasma nécessaire à l'établissement du champ magnétique confinant. Dans ce travail de thèse, la suite de code nommée SCENIC est utilisé afin d'étudier les applications des ondes à Fréquence Cyclotronique Ionique (FCI) aux plasmas de tokamak et de stellarator. Cet outil numérique a été conçu dans le but de résoudre de manière auto-cohérente l'équilibre magnétohydrodynamique (MHD) du plasma, la propagation de l'onde FCI et la fonction de distribution des ions résonants. Des simulations obtenus avec SCENIC sont présentées et permettent de comprendre comment l'instabilité de type dent-de-scie peut être contrôlée dans les tokamaks par une application adéquate de l'onde FCI. Cette méthode de contrôle a été utilisé avec succès dans le tokamak JET et il également prévu de l'appliquer dans le future tokamak ITER. Les stellarators ne développent pas de telles instabilités car ils ne nécessite pas l'induction de courant plasma. Le stellarator Wendelstein 7-X (W7-X) qui a récemment été démarré, doit cependant apporter la preuve expérimentale que la configuration magnétique isodynamique est capable de confiner efficacement les particules rapides. Aucune réaction de fusion de type D-T n'aura lieu dans W7-X et par conséquent aucune particle α ne pourra y être produite. Ainsi, une source auxiliaire et efficace d'ions rapides doit être développée pour cette machine. Dans cette thèse, nous étudions la possibilité de générer une importante population d'ions rapides dans W7-X par le truchement d'ondes FCI. Des calculs obtenus avec SCENIC permettent d'identifier des canaux pertes d'ions rapides pouvant subsister en dépit du caractère quasi-omnigène de l'équilibre MHD de W7-X. Ces simulations montrent également que le schéma de chauffage FCI dit "minoritaire" ne semble pas être adapté pour la production efficace d'ions rapides dans les plasmas de W7-X. Cependant, des ions à hautes énergies sont plus susceptibles d'apparaître si le schéma de chauffage FCI dit "à trois ions" est appliqué.

Contents

Contents

1 Introduction

1.1 The plasma state and fusion reactions

An increasing amount of scientific research has been focused in the past decades towards production of energy that does not produce greenhouse gases. At the beginning of the 20th century, physicists discovered that an incredible amount of energy is stored in the nuclei of atoms. It was found that, if brought sufficiently close to each other, two light atom nuclei can fuse into a heavier nucleus. The mass of the daughter nucleus is lower that the sum of the two parents nuclei so that, following Einstein's famous equation $\Delta E = \Delta m c^2$, the missing mass has been converted into energy. Stars, such as the sun, are powered by these nuclear reactions and produce the first elements in the Mendeleev period table up to iron. Physicists have been trying for the past sixty years to reproduce in a controlled manner these nuclear reactions in order to harvest fusion energy. Fusion reactions are possible if nuclei, having positive electric charge, have sufficient kinetic energy in order to overcome the Coulomb barrier that pushes them apart. This condition is reached when a sufficient amount of fuel is brought to very high temperature. In these conditions the fuel reaches the plasma state which is often called the fourth state of matter and which was well defined by F.F. Chen [1] as:

> *A plasma is a quasineutral gas of charged and neutral particles which exhibits collective behavior.*

The conception of a fusion reactor on Earth is a very challenging task because it requires forcing the plasma into favourable conditions for fusion reactions to occur. These conditions can be written in terms of the product of three crucial quantities (plasma density n_e, plasma temperature T_e and plasma energy confinement time τ). The fusion reaction that requires the least constraints to occur in a man-made fusion reactor involves deuterium and tritium (isotopes of hydrogen) nuclei:

$$\begin{smallmatrix}2\\1\end{smallmatrix}D + \begin{smallmatrix}3\\1\end{smallmatrix}T \rightarrow \begin{smallmatrix}4\\2\end{smallmatrix}He(3.5\,\text{MeV}) + n(14\,\text{MeV}) \tag{1.1}$$

In this equation, the kinetic energy of the reaction products are given in parenthesis. Neutrons

born from fusion reactions are free to escape the magnetic confinement and will heat up the reactor coolant, for example liquid water, that will generate electricity following a thermodynamic cycle commonly used in today's thermal power plant. Practically, the $_2^4He$ nuclei (also called α particle) will contribute to heat up the plasma and help to sustain the fusion reactions. Lawson derived a criterion [2] which gives the conditions for which a fusion reactor is self-sustained by the energy produced from α particles:

$$n_e T_e \tau \geqslant 10^{21} \mathrm{m}^{-3} \mathrm{keVs}. \tag{1.2}$$

Above this threshold, ignition is reached: no external heating sources are required to maintain the plasma at fusion relevant temperature. The confinement time is probably the most difficult parameter to control. The plasma in the core of the sun is confined by the considerable gravitational field generated by the sun's mass. On Earth, most of the fusion energy research is focused on inertial confinement (which involves powerful lasers to implode a target containing the fuel) and magnetic confinement (which uses magnetic field to confine the plasma). In this thesis we focus on the two main reactor concepts from the magnetic confinement branch: the tokamak and the stellarator. In fusion reactor-sized tokamak and stellarator machines, the typical order of magnitude that are aimed in terms of plasma parameters are: $n_e \simeq 10^{20} \mathrm{m}^{-3}$, $T_e \simeq 10 \, \mathrm{keV}$, $\tau \simeq 1 \, \mathrm{s}$.

1.2 Fusion device concepts

In fusion reactor machines, the core temperature is sufficiently high so that the plasma is fully ionised. According to Chen's definition, a fusion plasma is only formed of charged particles: electrons and ions. Electromagnetic fields exhert net forces on these particles which can be used to contain the plasma. Two main reactor concepts have been developed on this basic principle.

1.2.1 The tokamak

The tokamak is a toroidally symmetric donut shaped machine as shown in Fig. 1.1. The tokamak vacuum vessel designed to contain the plasma, is surrounded by planar coils which generate a toroidal magnetic field (green arrows in Fig. 1.1). As it will be mathematically described in chapter 1.4, charged particles that compose the plasma are sensitive to the external magnetic fields and gyrate around the magnetic field lines. This is the basic principle behind magnetic confinement. However, the inherent toroidal shape of the machine causes inhomogeneities in the magnetic field that in turn make the particles drift vertically out of the vessel. This vertical drift can be cancelled by an additional poloidal magnetic field which is generated by the flowing of a toroidal current inside the plasma (large red arrows in Fig. 1.1). The sum of the poloidal and toroidal magnetic fields is a helical confining magnetic field (yellow arrows in Fig. 1.1). The magnetic fusion research has been mainly focused on the tokamak concept so that most of the fusion plasma physics laboratories in the world have
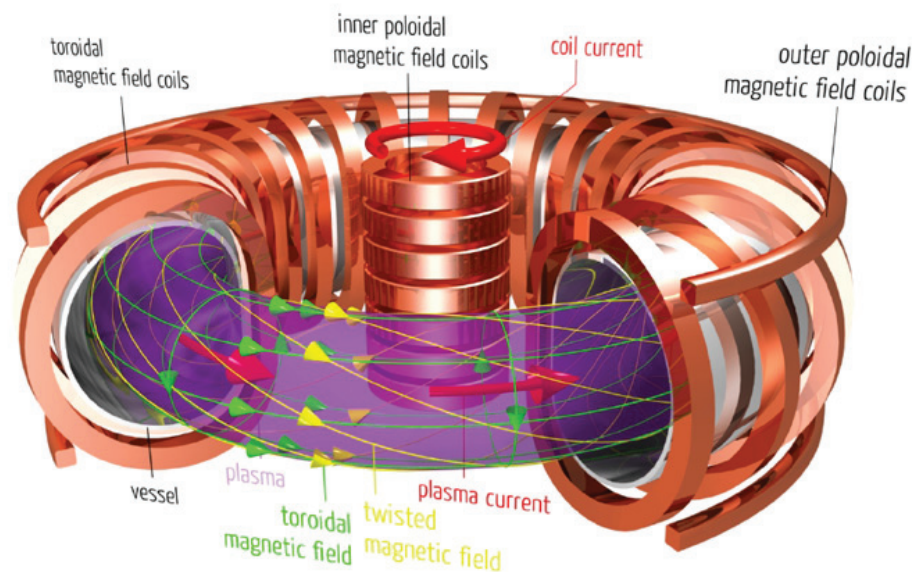
Figure 1.1: Schematic view of the tokamak concept. The main coil system and the confining magnetic field are shown. Courtesy of Max-Planck Institut für Plasmaphysik.

built their own tokamaks such as: TCV (Tokamak à Configuration Variable) in Switzerland, Tore Supra in France, ASDEX in Germany, NSTX (National Spherical Torus eXperiment) in the USA, etc. The largest tokamak now in operation is JET (Joint European Torus) in the UK. A larger experimental machine called ITER is a joint international effort and is now under construction in France. In tokamaks, the generation of the plasma current is crucial to the confinement of the plasma and is ensured by an external transformer. Physical constraints on the toroidal coils and the finite capacity of the transformer impose a time limit on tokamak operations. For example, TCV which uses copper coils can generate plasma for up to 2 seconds. The plasma duration can be extended by the use of superconducting coils and the induction of plasma current by launching lower hybrid waves in the plasma. Tore Supra was equipped with these technologies and was able to produce 6- minute plasmas (which counts among the longest tokamak plasmas). ITER benefits from all the accumulated tokamak knowledge and technology and is designed to produce plasmas for up to 600 seconds. However the plasma current is a source of instabilities that must be externally controlled in order to preserve plasma confinement. These inherent instabilities and the need for the generation of plasma current are the main drawbacks of tokamak technology.

1.2.2 The stellarator

The stellarator concept is similar to the tokamak in the sense that it aims at magnetically confining a plasma in a toroidal machine. However, the goal here is to generate the confining helical magnetic field without the use of the plasma current which is a source of instability
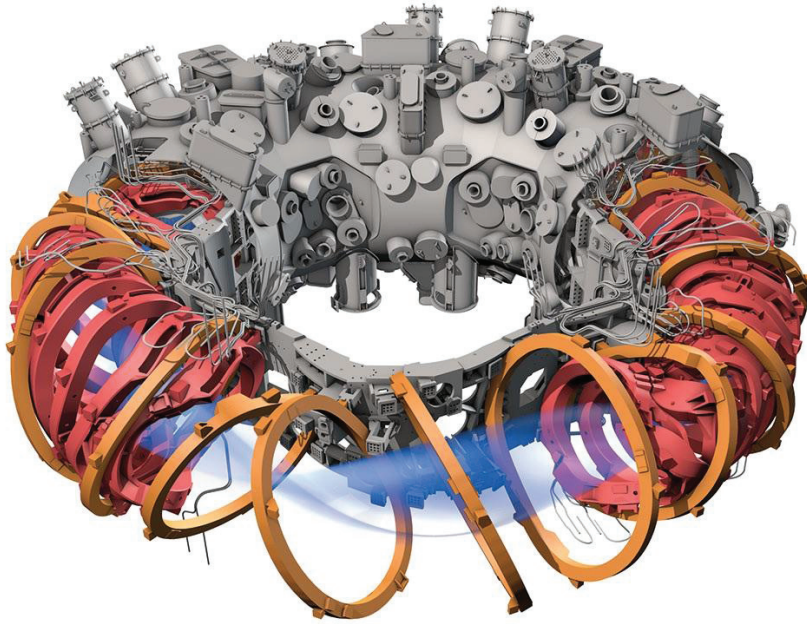
Figure 1.2: Schematic view of the stellarator concept. Courtesy of *www.sciencemag.org*.

and also technologically limits the duration of machine operation. The confining magnetic field of a stellarator is solely generated by external field coils so that no net toroidal plasma current flows in the plasma. The magnetic field coils are therefore shaped in three dimensions so that the resulting twisted magnetic field lines confine the plasma. A illustration of the Wendelstein 7-X (W7-X) stellarator that started operation in 2016 is shown in Fig. 1.2. W7-X is equipped with superconducting coils. The engineering and the manufacturing of such a coil system is one of the main reasons that make stellarator machines more complicated and more coslty to build compared than tokamaks. However future stellarators of the type of W7-X will be able to produce energy in steady state since no current induction is required. Also, since no net plasma current flows in the plasma, most of the deleterious instabilities occuring in tokamaks are avoided. The technical and economical difficulties brought by the intrinsic three-dimensional nature of stellarators have long hindered to the development of these machines. Theoretical progress, in particular the elaboration of the quasi-isodynamic stellarator concept, and consequently the construction of W7-X, renewed the interest of the scientific community in stellarators. A short review of the stellarator history and current state will be presented in chapter 3.6.

1.3 Thesis contribution

Sustaining reactions in a fusion device requires heating the plasma to high temperatures, typically above 10 keV. For particles to reach such energies, different heating schemes have to be combined. In tokamaks, the plasma temperature is increased partly via ohmic heating generated by the plasma current. This source of heating is however not sufficient to reach
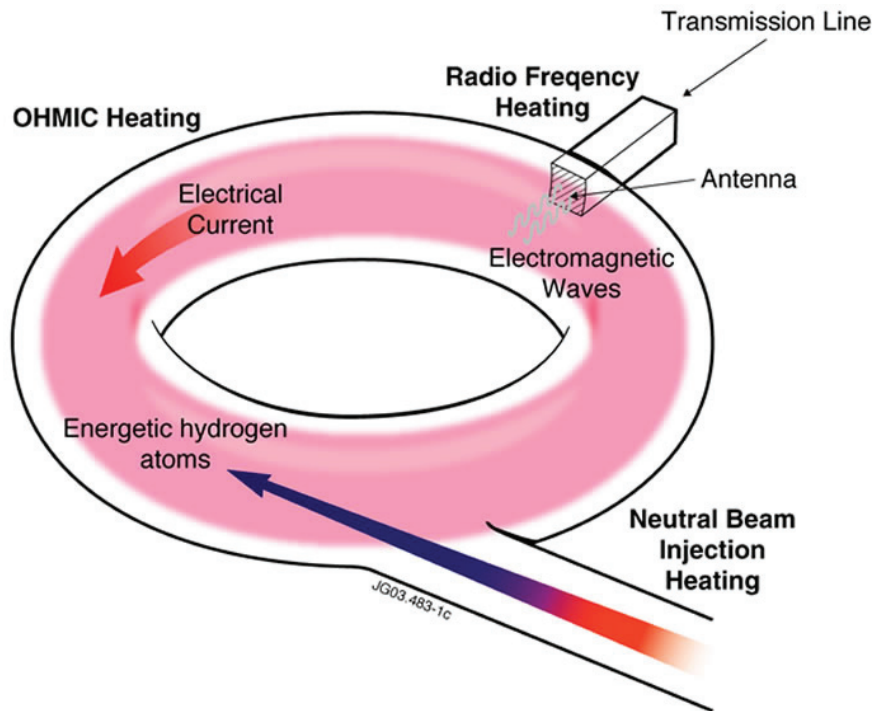
Figure 1.3: Auxiliary heating sources applied to fusion devices. Courtesy of *www.euro-fusion.org.*

fusion relevant temperatures, plus, stellarators cannot in principle beneficit from this method. Additional auxiliary heating sources must therefore be applied. Figure 1.3 illustrates the various heating methods that have been developed to efficiently heat fusion plasmas. Neutral Beam Injection (NBI) consists of injecting highly energetic neutral atoms that will transfer their energy to the plasma via charge exchange processes and Coulomb collisions. In addition, electromagnetic waves tuned at the ion and/or electron cyclotron frequency can be used to accelerate the plasmas charged particle population and consequently raise the plasma temperature. This method is commonly referred to as Radio Frequency (RF) heating. Once fusion relevant temperature is reached and fusion reactors are initiated, a significant amount of plasma heating is ensured by fast α particles, born from fusion reactions (eq. 1.1) at 3.5 MeV, that slow down on the background electrons and ions via Coulomb collisions. Future fusion reactors producing electricity must therefore be able to confine α particles during their slowing down time in order to increase the machine efficiency. In tokamaks, the toroidal symmetry in the magnetic field allows in general good fast particle confinement. However, α particles are known to interact with the so-called sawtooth instability in tokamaks that not only degrades the plasma performance but can trigger secondary instabilities which can lead to the complete loss of the plasma confinement. This instability can however be externally controlled. Indeed, the energy transfer from the RF waves to the resonant particles not only increases their energy but also modifies significantly the particles distribution in phase-space. This can cause for example an increase in the fraction of so-called mirror trapped particles, asymmetries in the

particle velocity distribution, or generate strong local current densities. Consequently, RF wave scenarios have been developed in order to use these kinds of redistribution to control the sawtooth instability and limit its impact on the plasma performance. In the work presented here, we address, using the appropriate numerical tool `SCENIC`, the following problems:

- the physical interpretation for the experimental observations of the JET plasmas where ICRF waves were used to control the sawtooth instability,

- the relevant physical mechanism at stake for the observed triggering of the sawtooth instability,

- the resonant ion distribution function related to this mechanism.

In stellarators, most of the plasma instabilities that are encountered in tokamaks are non-existent because no plasma current is required. However the intrinsic three-dimensional structure of the magnetic field does not guarantee good confinement of fast particles over their slowing down time. Stellarator fields must therefore be conceived to take this major constraint into account. In this thesis we study the magnetic configuration of the W7-X stellarator that has been optimised for the confinement of fast particles. We try to answer the following questions.

- Are there still particle loss channels in W7-X despite the optimisation procedure that led to its design?

- Since one of the main experimental goals of W7-X is to prove the capacity of the quasi-isodymanic concept to confine efficiently fast particles such as α particles, this thesis addresses whether a significant fast ion population can be generated in the machines high density plasma.

- A final question addressed is whether Ion-Cyclotron Range of Frequency (ICRF) wave absorption scenarios can generate distributions with confined fast ion tails in W7-X in advance of a future isodynamic nuclear fusion reactor.

1.4   Outline

The remainder of this thesis is organised as follows. In chapter 1.4, the relevant plasma physics concepts for the understanding of the results presented in the next chapters are explained. The numerical code package `SCENIC` that is used throughout this thesis is also presented.

`SCENIC` simulations applied to JET experimental plasmas where sawtooth instabilities were actively controlled by application of ICRF waves are presented in chapter 2.4. The fast ion mechanism most likely responsible for the triggering of sawteeth is presented.

Chapter 3.6 is dedicated to the study of the W7-X stellarator. Standard W7-X magnetic configurations are analysed in terms of collisionless particle confinement. Fast particle loss channels are identified and illustrated with relevant simulations of an NBI-like population. The ion distribution function obtained in a typical W7-X plasma under ICRF heating conditions is analysed. The confined fast ion and lost particle distributions are discussed. The inclusion of a neoclassically resolved radial electric field in the fast ion simulations is addressed.

The so-called minority heating scheme is most commonly applied to tokamak and stellarator plasmas. As shown in chapter 4.6, this scenario is quite inefficient in W7-X high plasma density, at least for generating long fast ion tails. To address this, an alternative three ion species scheme is modelled with the SCENIC tool in chapter 4.6. The fast ion distribution obtained with this scheme applied to a JET plasma is analysed. Three ion species simulations in a W7-X plasma are then presented. The results indicate that this scheme would be more suitable than standard minority heating schemes for generating a significant fast ion population in W7-X.

Finally, the results gathered throughout this thesis are summarised in chapter 5.4. Many possible improvements of the SCENIC code package are also discussed. Some potential physical questions that remain to be solved are also mentioned.

2 Equilibrium, heating and fast particles: the basis of the `SCENIC` package

The basic principle of plasma equilibrium, charged particle orbits in a magnetic field and the propagation of electromagnetic waves in a plasma are briefly reviewed. Important considerations are reviewed on particle orbits and transport in stellarators. The working principles of the codes comprising the `SCENIC` package which is the modelling tool used throughout this thesis are also presented.

2.1 Magnetic confinement: equilibrium and particle orbits

2.1.1 Ideal MagnetoHydroDynamic equations

The basic working principle of tokamak and stellarator machines is to magnetically confine a plasma. As the plasma is composed of particles of opposite signs which have collective behaviour, it can reasonably be regarded on a macroscopic scale as a mixture of two charged fluids. In tokamaks, an electrical current is generated in the plasma to create the poloidal magnetic field. In stellarators, there is no such plasma current, however local current densities arise. Therefore the auxiliary generated magnetic field will exert Lorentz forces $\boldsymbol{J} \times \boldsymbol{B}$ on the plasma. As in neutral fluids, pressure gradients arise and apply also forces on the plasma fluid elements. Ignoring the electrical resistivity of the plasma, the balance of the Lorentz and pressure forces is written by virtue of the Newton's second law as:

$$\boldsymbol{J} \times \boldsymbol{B} - \nabla p = 0. \tag{2.1}$$

The confining field and the current density flowing in the plasma must verify Maxwell's equations:

$$\nabla \cdot \boldsymbol{B} = 0, \tag{2.2}$$

$$\nabla \times \boldsymbol{B} = \mu_0 \boldsymbol{J}. \tag{2.3}$$

Equations 2.1 to 2.3 form the basis of the plasma ideal MagnetoHydroDynamic (MHD) equilibria. Solutions of this system of equations can be obtained for prescribed current density and

pressure profiles. A certain number of crucial assumptions help the calculation of such solutions. It is useful to introduce now a curvilinear coordinate system which relies on quantities derived from the magnetic field. Let us consider for the sake of simplicity a tokamak device which has the advantage of being (nearly) toroidally symmetric. As it was briefly discussed in the previous chapter, the magnetic field must be helical in order to compensate vertical drifts that would lead to rapid loss of the plasma. This magnetic field can be written as a sum toroidal and poloidal components:

$$\boldsymbol{B} = \boldsymbol{B}_t + \boldsymbol{B}_p. \tag{2.4}$$

The magnetic axis is defined as the locus where the magnetic field is purely toroidal, i.e. where $\boldsymbol{B}_p = 0$. The magnetic axis defines the origin of surfaces that measure the flux of poloidal magnetic field:

$$\psi_p = \int_S \boldsymbol{B} \cdot \mathrm{d}\boldsymbol{S}. \tag{2.5}$$

An example of one such surface is illustrated in Fig. 2.1. A system of flux coordinates (ψ_p, u, v) can be conveniently defined such that ψ_p is considered as the radial variable, and u and v are respectively the poloidal and toroidal angles. v is taken here as the cylindrical angle. The magnetic field can then be written in a covariant and contravariant form:

$$\boldsymbol{B} = B_{\psi_p} \nabla \psi_p + B_u \nabla u + B_v \nabla v, \tag{2.6}$$

$$\boldsymbol{B} = B^u \boldsymbol{e}_u + B^v \boldsymbol{e}_v. \tag{2.7}$$

It can be shown that the component B^{ψ_p} vanishes by invoking the Maxwell's equation $\nabla \cdot \boldsymbol{B} = 0$ and the conservation of the poloidal flux. This gives the fundamental result: $\boldsymbol{B} \cdot \nabla \psi_p = 0$, which means that the magnetic field lines lies on surfaces of constant ψ_p called magnetic flux surfaces.
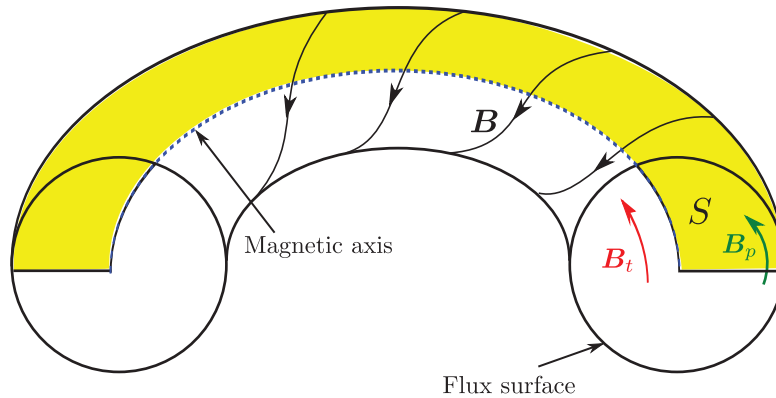

Figure 2.1: Illustration of the confining magnetic field components and an example of surface S that measures the poloidal magnetic flux.

Additionally, the magnetic flux encapsulated by these magnetic flux surfaces defines the toroidal magnetic flux ψ_t which can alternatively be used as a radial variable. The fluxes ψ_t and ψ_p define the local pitch of the magnetic field lines on a given flux surface, which is commonly called the local safety factor:

$$q_l = \frac{B^v}{B^u} = \frac{\mathrm{d}\psi_t}{\mathrm{d}\psi_p}. \tag{2.8}$$

The flux surface average of q_l gives the safety factor $q(\psi_p)$ which is most commonly used. Note that it is possible to define the flux coordinate system (ψ_p, u, v) such that the magnetic field lines are straight in the $u - v$ planes, in which case $q_l = q$. In Reverse Field Pinch (RFP) machines, the magnetic field reverses direction on a certain flux surface causing $q \to 0$, so that the most commonly used radial variable is based on ψ_p. In stellarators however, currents and poloidal fields are usually weak, so that radial variables are often based on ψ_t, and the commonly used winding index is $\iota = 1/q$.

The assumption of axisymmetric geometry gives for any scalar quantity A the property: $\frac{\partial A}{\partial v} = 0$. The projection of eq. 2.1 on $\boldsymbol{B}$ gives:

$$\boldsymbol{B} \cdot \nabla p = 0 \Rightarrow \left(B^u \boldsymbol{e}_u + B^v \boldsymbol{e}_v \right) \cdot \left(\frac{\partial p}{\partial \psi_p} \nabla \psi_p + \frac{\partial p}{\partial u} \nabla u \right) = 0 \tag{2.9}$$

$$\Rightarrow B^u \frac{\partial p}{\partial u} = 0. \tag{2.10}$$

Since the magnetic field must possess a non-zero poloidal component, the plasma fluid pressure must therefore only be a function of the flux variable: $p = p(\psi_p)$. Equivalently, one can say that the pressure is a flux surface quantity and that the flux surfaces are iso-pressure surfaces. It is also seen that the hypothesis of having a toroidally symmetric system ensures that the flux surfaces are nested around the magnetic axis. Based on this result, the ideal MHD balance equation 2.1 can be projected in the $\nabla \psi_p$ direction in order to obtain the famous Grad-Shafranov [3, 4] equation for axisymmetric (or 2D) MHD equilibrium:

$$R \frac{\partial}{\partial R} \left(\frac{1}{R} \frac{\partial \psi_p}{\partial R} \right) + \frac{\partial^2 \psi_p}{\partial Z^2} = -R^2 \frac{\mathrm{d}p}{\mathrm{d}\psi_p} - B_v \frac{\mathrm{d}B_v}{\mathrm{d}\psi_p}. \tag{2.11}$$

In Eq. 2.11, the left-hand side and the term $\frac{\mathrm{d}B_v}{\mathrm{d}\psi_p}$ are related to the current density flowing in the plasma. Given some hypothesis on the analytic form of the pressure and toroidal magnetic field B_v profiles, analytic solutions of the Grad-Shafranov such as the Solov'ev equilibrium can be derived. More solutions can be found numerically by the use of computer codes. These tools allow the prescription of more general pressure and current density profiles. Boundary conditions on the shape of the flux surfaces are also usually to be provided. For example, the EFIT code [5, 6] solves the Grad-Shafranov equation in order to reconstruct the 2D equilibrium based on experimental measurements of the pressure, the current density and of the plasma shape. The CHEASE code [7] is another Grad-Shafranov solver which is widely used to provide equilibrium solutions to other codes which solve for example MHD stability or low frequency

wave propagation.

If one relaxes the axisymmetric assumption, the equilibrium state cannot be analytically described by the Grad-Shafranov equation. More importantly, in three-dimensional equilibria such as stellarator plasmas, the existence of the nested flux surfaces cannot necessarily be ensured throughout the whole plasma volume. Some equilibrium codes such as `PIES` [8] and `SPEC` [9] are able to converge to equilibrium states where regions of nested flux surfaces are surrounded by a domain where the magnetic field lines are stochastic or form magnetic islands. Nevertheless, numerical calculations and experimental observations confirm that regions of nested flux surfaces can be found even in 3D systems. Therefore it is valid to solve the ideal MHD equilibrium while prescribing the existence of nested flux surfaces. A re-formulation of the MHD force balance equation is found to render this task more tractable. It can be shown that equation 2.1 is strictly equivalent to minimising the plasma energy functional defined as:

$$\mu_0 W = \int dV \left(\frac{B^2}{2} + \frac{\mu_0 p(\psi_p)}{\Gamma - 1} \right) \tag{2.12}$$

where Γ is the adiabatic index. The `VMEC` code [10] uses a steepest-gradient method in order to find the minimum of this functional. This code is part of the `STELLOPT` package designed for the optimisation of the 3D MHD equilibria which helped the design of the Wendelstein 7-X stellarator. The `ANIMEC` code is an extension of `VMEC` that takes into account the pressure anisotropy, typically arising from fast particles has been developed [11], and this will be described lated in section 2.3.2. One of the most important outputs of MHD codes is the equilibrium magnetic field amplitude since it characterises the plasma device. Figures 2.2 and 2.3 show examples of the B distribution for the JET tokamak and the W7-X stellarator configurations.
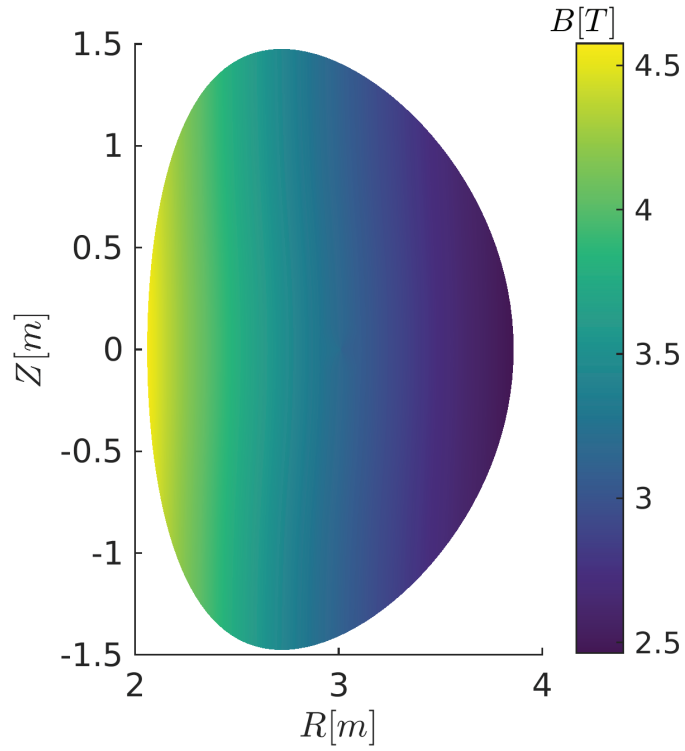
Figure 2.2: Magnetic field amplitude profile for a typical JET-like equilibrium.
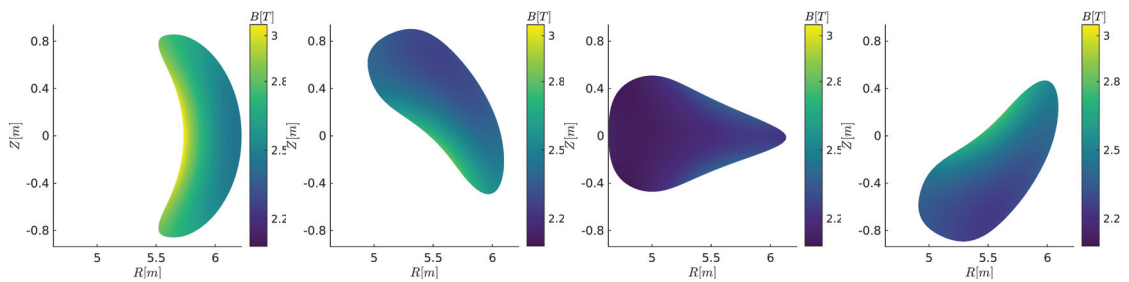
Figure 2.3: Magnetic field amplitude profiles at various toroidal positions for a W7-X high-mirror equilibrium.

2.1.2 Charged particle orbit in a magnetic field

Cyclotron motion

The ideal MHD equation gives a framework for the calculation of magnetic equilibria which can be used to study the trajectory of fast particles. This is a fundamental notion used in this thesis and we shall therefore describe the basis of the motion of charged particles bathing in a magnetic field. Let us first consider a uniform and static magnetic field $\boldsymbol{B}$ pointing in the $\hat{\boldsymbol{z}}$ direction in a Cartesian frame. Using Newton's second law, one can derive the equations of motion of a single particle considered initially at rest with charge Ze and mass m. This derivation can be found in numerous plasma physics textbooks such as in Chapter 2 of Ref. [1]. Therefore only the main relevant results are discussed here. The Lorentz force acting on the particle will set it into a gyro-motion in the $x - y$ plane which can be described as:

$$x - x_0 = r_L \sin \omega t \tag{2.13}$$
$$y - y_0 = r_L \cos \omega t. \tag{2.14}$$

It is seen that the gyro- or cyclotron motion of the charged particle is characterised by:

$$\omega_c = \frac{ZeB}{m} \quad \text{the cyclotron frequency,} \tag{2.15}$$

$$(x_0, y_0) \quad \text{the trajectory of the guiding centre,} \tag{2.16}$$

$$r_L = \frac{|\boldsymbol{v} \times \boldsymbol{B}/B|}{\omega_c} = \frac{v_\perp}{\omega_c} \quad \text{the Larmor radius.} \tag{2.17}$$

If the charged particle possesses an initial velocity $\boldsymbol{v}_0$, i.e. before the magnetic field is switched on, then the guiding centre will move along the magnetic field line with the parallel velocity: $v_\parallel = \boldsymbol{v}_0 \cdot \boldsymbol{B}/B$ as shown in Fig. 2.4:

Figure 2.4: Schematic of the gyro-motion of a charged particle around a magnetic field line. Courtesy of *www.euro-fusion.org*.

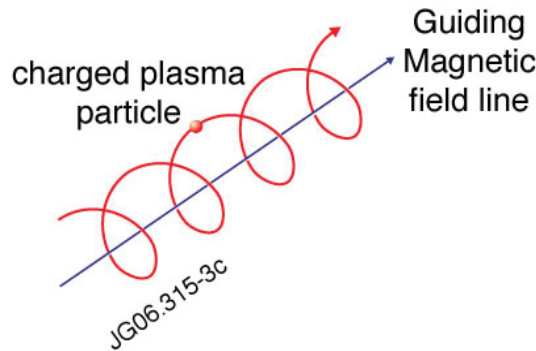The perpendicular velocity can be used to defined the magnetic moment μ:

$$\mu = \frac{1}{2}mv_\perp^2/B. \tag{2.18}$$

This quantity can be shown to be an adiabatic invariant associated with the cyclotron motion of the particles for slowly time (and spatially) varying magnetic fields. In the particular case of a static magnetic field, μ is a constant of motion. Moreover the main forces that acts on the plasma charged particles are purely electromagnetic. The electric force causing the $\boldsymbol{E} \times \boldsymbol{B}$ drift is conservative and the Lorentz force does not produce any work on the particle. Therefore the particles total energy

$$E = E_{kin} + E_{pot} = \frac{1}{2}m\left(v_\parallel^2 + v_\perp^2\right) + Ze\Phi, \tag{2.19}$$

with the electric potential Φ, is conserved along its trajectory. As illustrated in Figs. 2.2 and 2.3, the confining magnetic field of fusion plasma devices exhibits the appearance of regions of stronger and weaker magnetic field. We shall see that these spatial variations have a strong effect on the particles trajectory.

Guiding centre trajectory

It is seen that if one chooses to fully resolve the cyclotron motion of the charge particle, the corresponding phase-space is comprised of 6 dimensions (3 for the particles position and 3 for its velocity). However, in most plasma applications the Larmor radius is small compared to the characteristic length of the magnetic field variation. Therefore the single particle motion can be approximated by the motion of the guiding centre. Therefore the particles phase-space can be reduced to 4 dimensions: only the guiding centre position and parallel velocity need to be resolved. This very convenient framework, discussed in Ref. [12], is known as the guiding centre drift formalism and is the basis of the numerical simulations presented in this thesis. The guiding centre dynamics is therefore dictated by the variables $\left(\boldsymbol{X}_{gc}, \rho_\parallel = mv_\parallel/qB\right)$: the guiding centre position and the parallel gyro-radius.

In an unbounded homogeneous magnetic field, the guiding centre trajectory will stick to the magnetic field lines. However, drifts of the guiding centre appear if the magnetic field amplitude is inhomogeneous and/or if an electric field is present. We shall now discuss the relevant sources of drifts and define the corresponding guiding centre drift velocities at the first order. In tokamaks, the equilibrium magnetic field amplitude varies strongly in the poloidal direction, mainly because the toroidal field coils are closer to each other on the inboard side of the torus compared to the outboard side. Stellarators do not possess toroidal symmetry, so that the magnetic field amplitude varies also in the toroidal direction. In both type of machines, charged particles experience gradients of B which translates into a guiding centre

velocity drift:

$$\boldsymbol{v}_{\nabla B} = \frac{\mu}{q}\frac{\boldsymbol{B} \times \nabla B}{BB_{\parallel}^*}, \tag{2.20}$$

where $B_{\parallel}^* = \frac{\boldsymbol{B}}{B} \cdot \left(\boldsymbol{B} + \rho_{\parallel}\nabla \times \boldsymbol{B}\right)$ is the modified magnetic field as discussed in Ref. [13]. In addition, because of the toroidal geometry of these machines the magnetic field lines are intrinsically curved. The magnetic field lines curvature can be written as [14]:

$$\boldsymbol{\kappa} = -\frac{\boldsymbol{B}}{B} \times \left(\nabla \times \frac{\boldsymbol{B}}{B}\right). \tag{2.21}$$

This other form of inhomogeneity gives rise to a curvature drift:

$$\boldsymbol{v}_{\kappa} = v_{\parallel}\rho_{\parallel}\frac{\boldsymbol{B} \times \boldsymbol{\kappa}}{BB_{\parallel}^*}. \tag{2.22}$$

Inspection of the combination of these two drifts already shows that a guiding centre orbit does not stick to the magnetic field lines but instead crosses flux surfaces. The cross field drifts of eqs. 2.20 and 2.22 line increase with the particles energy.

Finally, electric fields may arise in fusion plasmas which in turn act upon the particles trajectory via $\boldsymbol{E} \times \boldsymbol{B}$ velocity drifts:

$$\boldsymbol{v}_{E \times B} = \frac{\boldsymbol{E} \times \boldsymbol{B}}{BB_{\parallel}^*} \tag{2.23}$$

It will be shown in section 2.1.4 and in chapter 3.6 that this drift is expected to play a significant role in particle confinement in the W7-X stellarator. This guiding centre drifts of eqs. 2.20, 2.22 and 2.23 are not exhaustive but already contain the relevant physics for the scope of this thesis.

The resolution of the fast ion distribution requires solving in time the guiding centre trajectories, and is consequently a computationally demanding task which usually involves numerical tools. Many computer codes have been written in order to tackle this task. The toroidal symmetry of tokamak plasma can be exploited in order to invoke the conservation of a third quantity known as the toroidal angular momentum P_{φ}. The `FIDO` [15] code uses the 3 constants of motion $\left(E, \mu, P_{\varphi}\right)$ that uniquely define orbits to resolve fast ion distributions. This approach reduces the required numerical resources but is however restricted to axisymmetric configurations. Other codes implement algorithms that directly solves in time the guiding centre equations of motion and are able to deal with both 2D and 3D magnetic configurations. This applies to the codes `ASCOT` [16], `SPIRAL` [17], `ANTS` [18] and `VENUS-LEVIS` [19].

2.1.3 Trapped particles trajectories

Consider a single-particle motion in a static tokamak or stellarator magnetic field, and for simplicity assume that there is no electric field. The particle kinetic energy E and magnetic magnetic moment μ, in the approximation of slowly varying fields, are constant along the free guiding centre trajectory. The magnetic field spatial dependency for a typical tokamak and stellarator was illustrated in Figs. 2.2 and 2.3. It is therefore expected that particles will experience varying magnetic field amplitude along their trajectory. Since μ is a constant of motion, as a particle sees an increasing magnetic field amplitude along its trajectory, the particles perpendicular velocity must increase in order to keep μ (adiabatically) constant at all times. Consequently, by virtue of the conservation of the kinetic energy E, the parallel velocity must decrease. Depending on the particles initial position in phase-space (position and velocity) and the strength of the magnetic field, the parallel velocity may vanish and change sign. The particle is therefore reflected by the magnetic field. This effect is often called magnetic mirroring and gives rise to trapped particle orbits. One can introduce the notion of a critical magnetic field for particle reflection B_{ref} which is essential to classify the classes of particle orbit. This quantity defines the value that the ambient magnetic field must reach so that a particle is reflected. If a particle is trapped then its parallel velocity $v_\parallel$ vanishes at the bounce points. B_{ref} is the magnetic field amplitude at the bounce point. Therefore the particle energy at this location is:

$$E = \frac{1}{2}mv_{\perp,bounce}^2 = \frac{1}{2}mv_{\perp,bounce}^2 \frac{B_{ref}}{B_{ref}} = B_{ref}\mu. \tag{2.24}$$

It then follows:

$$B_{ref} = \frac{E}{\mu}. \tag{2.25}$$

B_{ref} is a function of constants of motion and is used to classify orbits in tokamaks and stellarators. Trapped particles therefore refer to particles for which the parallel velocity eventually vanishes along their trajectory because $B = B_{ref}$ at a given position. On the other hand passing particles possess sufficiently high parallel velocity such that they never encounter the situation $B = B_{ref}$. These particles are able to circulate around the machine without being reflecting.

In tokamaks, trapped particles will mainly visit the low-field side (LFS) of the machine because the iso-surfaces of B are approximately vertical lines in the $R - Z$ plane projection (see Fig. 2.2). An example of the resulting trajectory is shown by the red lines in Fig. 2.5 which indicates two important features of trapped particle orbits in axisymmetric tokamaks. Firstly, the particle does not take the same path after one bounce: the ∇B and curvature drifts result in a net vertical drift which gives a width to the trapped particles orbit. After two bounces, trapped particle orbits do repeat in the $R - Z$ plane of an axisymmetric configuration. The trapped orbits are more commonly called banana orbits because of their shape. Let us mention that passing particles also experience this vertical drift and also possess a finite orbit width. The particles orbit width has crucial consequences, e.g. on particles and heat transport as
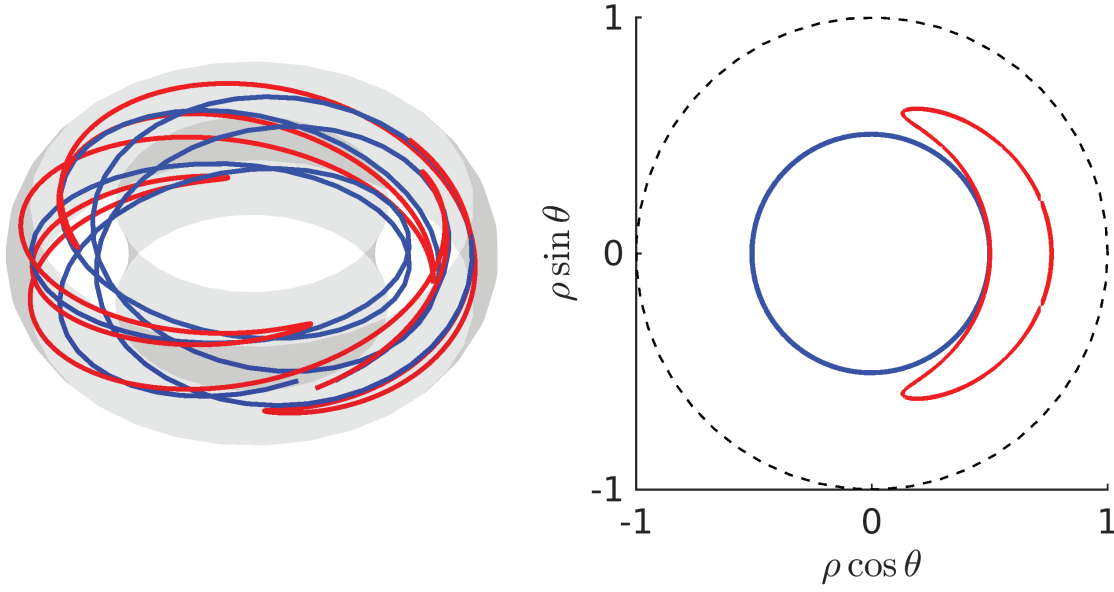
Figure 2.5: Passing (blue) and trapped (red) particles orbit in an axisymmetric equilibrium. Right: projections of the orbits in the pseudo-Cartesian system obtained via the magnetic flux coordinate system $\left(\rho = \sqrt{\psi_t/\psi_{edge}}, \theta, \varphi\right)$. Dashed line: last closed flux surface.

discussed in the following section. Secondly, the symmetry of the magnetic field equilibrium causes the banana orbit to be symmetric with respect to the mid-plane: the toroidal symmetry of tokamak magnetic field causes the vertical ∇B drift on each banana leg to compensate. Therefore collisionless trapped particles are well confined in tokamaks. The trajectory coloured in red in the left panel of Fig.2.5 suggests that trapped particles possess a net toroidal motion around the machine. The straight-field line Boozer coordinate system (discussed in section 2.3.2) (s, θ, φ) is used for the computation of the orbits shown in Figs. 2.5 to 2.8. Inspecting the projection of a banana orbit in the $\theta - \varphi$ plane, Fig.2.6 shows that the motion is not toroidally bounded but instead the trapped particles experience a net toroidal precession drift. The toroidal precession is similar to the motion of a spinning top around the vertical axis and corresponds to the change in time of the toroidal position of the trapped particles banana tips. A toroidal precession frequency ω_φ is usually associated to this bounce averaged toroidal motion.

This discussion indicates that in tokamaks, particle orbits fall into two main categories: passing and trapped. A more detailed classification of particle orbits in tokamaks can be found in Ref. [20]. In stellarators, the three-dimensional variation of B complicates this picture. Analysis and classification of particle orbits in stellarators are found in Refs. [21, 22]. In mirror machine type stellarators such as W7-X, a classification of the particle orbits can be made following the particle trajectory in a given toroidal period. The terminology introduced in Ref. [21] is now used. Three types of orbits are identified on the basis of their trajectory around the whole torus.
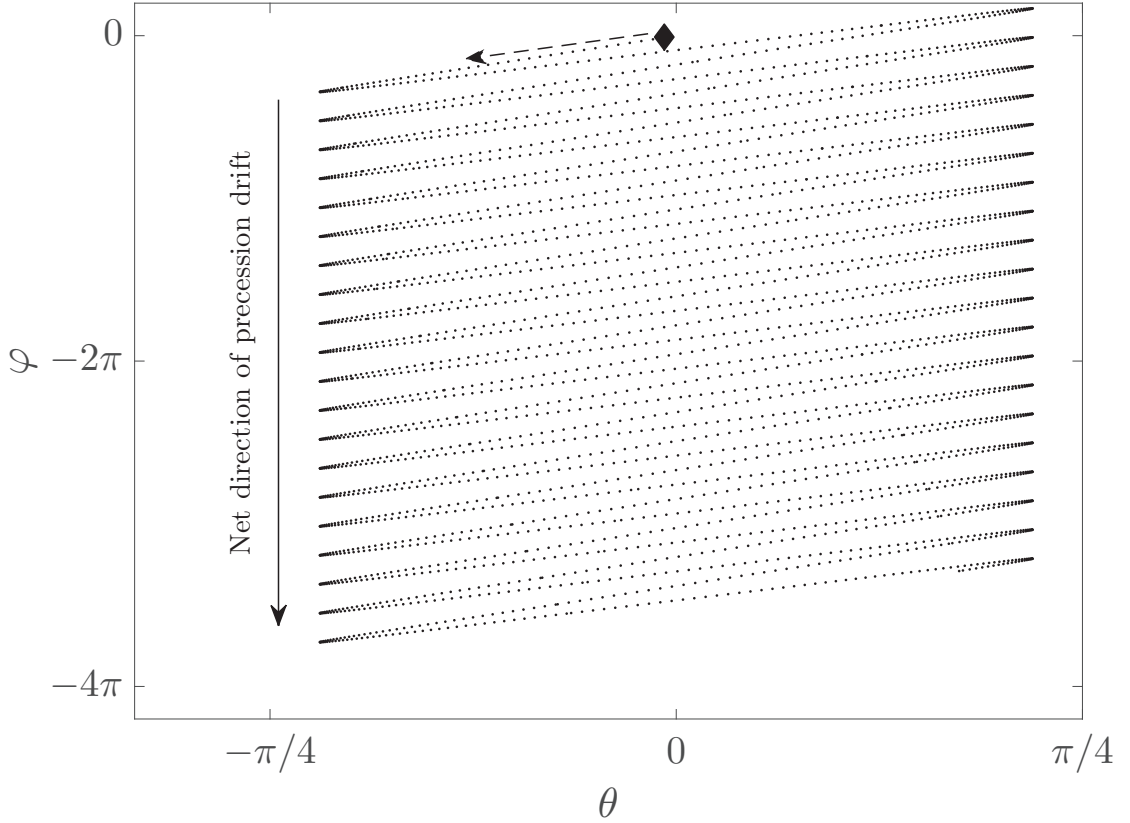
Figure 2.6: Projection in the $\theta - \varphi$ plane of a trapped particle trajectory (dotted line) in a tokamak equilibrium.◆: initial particles position. --→: initial drift direction.

Passing particles: These particles are able to complete a full toroidal revolution around the machine without ever being reflected (assuming no collisions). Passing particles are charac- terised by a B_{ref} value higher than the maximum value of the equilibrium magnetic field on the particle trajectory.

Localised or toroidally trapped particles: Depending on the mirror ratio value, there can exist a population of particles that will remain locally trapped by the toroidal magnetic mirror and can never travel to the next toroidal period. In this case, the particle trajectory is toroidally bounded by two iso-surfaces $B = B_{ref}$. These iso-surfaces are poloidally closed and are located between two consecutive bean shaped cross sections in the case of W7-X.

Blocked or helically trapped particles: These particles are located in the region of phase space near the locally trapped-passing boundary. These particles may be regarded as locally trapped for a few bounces but they are able to de-trap collisionlessly. A blocked particle's trajectory is not restricted to a single toroidal segment but extends to neighbouring sections. Such particles are also called transitioning [23]. An illustration of these three types of orbits and a comparison with particle orbits in an axisymmetric plasma is given in Fig. 2.7. Orbits are drawn in a full torus and in a poloidal cross section.
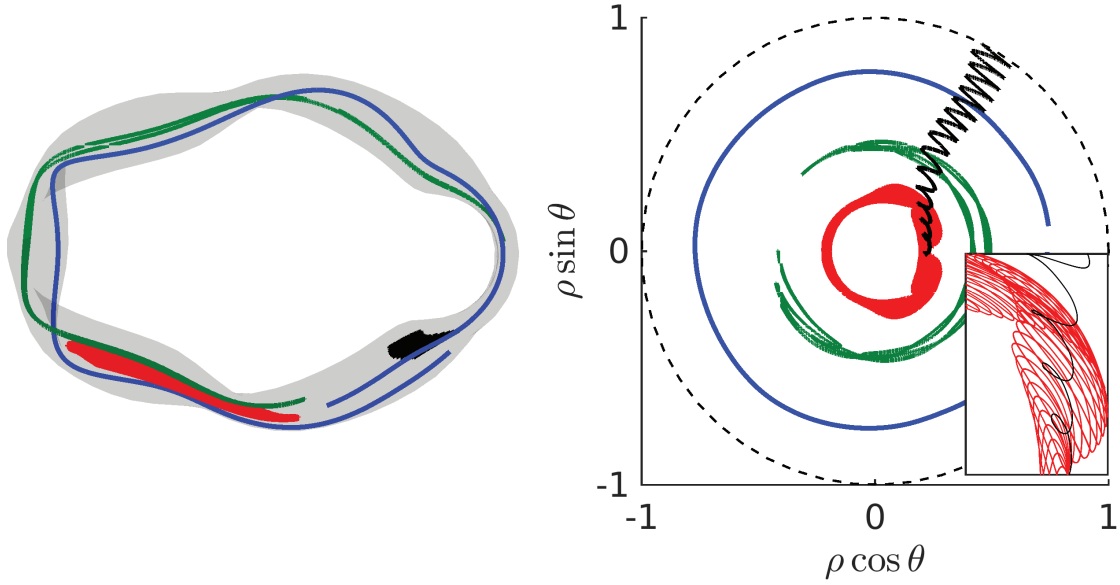
Figure 2.7: Passing (blue, $B_{ref} = 4.5T$), blocked (green, $B_{ref} = 2.5T$) and localised (red, $B_{ref} = 2.22T$) particles orbit in a W7-X high-mirror equilibrium. Another example of a localised particle orbit with $B_{ref} = 2.22T$ is shown in black. In this case the particle drifts rapidly outside the plasma.

Localised particles are of concern is W7-X because, contrary to the tokamak case, the magnetic drift may not compensate along the trapped trajectory due the three-dimensional structure of the magnetic field. Indeed, particles trapped in the main magnetic field wells may drift rapidly out of the plasma (see black line in Fig. 2.7). In order to better characterise a confined localised particle motion, one can inspect its projection in the $\theta - \varphi$ plane as shown in Fig. 2.8. It is seen that confined particles trapped between main mirrors possess a bounded toroidal motion and a net poloidal precession drift. This poloidal drift is associated with a poloidal precession frequency ω_θ which can be seen as the equivalent of the toroidal precession frequency for trapped particles in axisymmetric tokamaks. The poloidal precession is of most importance for localised particles in W7-X. Indeed it shall be shown that such particles remain confined if the poloidal precession is strong enough to restore a certain symmetry in the magnetic field amplitude "seen" by the particle. Some degree of quasi-symmetry can be achieved in order to increase the poloidal drift frequency of localised particles. These aspects and the resulting consequences on the design of W7-X will be further discussed in section 4.2.1. However, in certain regions of stellarators, ω_θ vanishes for some particles. The resulting trajectories have a dominant radial contribution and the particles escape quickly from the plasma. These so-called super-banana orbits are mostly seen in low collisionality regimes. This kind of orbit also appears because of the presence of local minima in the magnetic field as is the case for the black orbit in Fig. 2.7. Similar orbits are seen in the edge region of rippled tokamaks which also exhibits local minima of B. These ripple losses can be reduced in tokamaks by increasing the number of toroidal coils or by using ferritic inserts.
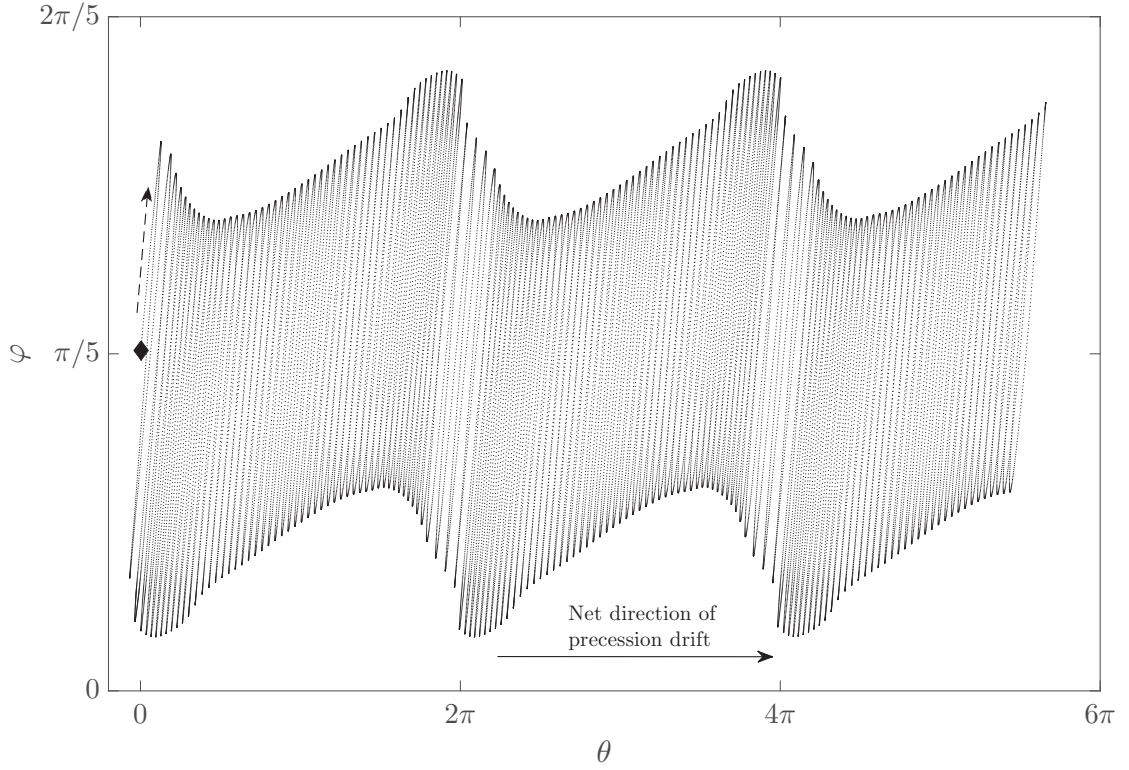
Figure 2.8: Projection in the $\theta - \varphi$ plane of a confined trapped particles trajectory (dotted line) in a W7-X equilibrium.♦: initial particles position. - - →: initial drift direction.

2.1.4 Confinement and transport in toroidal devices

Transport mechanisms

Despite the magnetic field being designed in part for improved plasma confinement, particle and energy loss is observed in tokamaks and stellarators. Several mechanisms are responsible for these deleterious phenomena. Coulomb interactions, i.e. short-range electromagnetic interactions, between the plasma species partly explains this transport. Coulomb collisions can be described as a diffusive process and follows with good accuracy a random walk model. Inter-species Coulomb collisions cause the outward diffusion of electrons and ions. The diffusion coefficients that dictate the flux of particles and heat depend on the temperature and density profiles applied to the plasma. This classical transport model however overestimates the confinement level in toroidal machines. The first reason comes from the orbit width of trapped particles which can be quite large and participate significantly in the transport process. Neoclassical transport theory aims at including the effect of the toroidal magnetic geometry and therefore of trapped particles to the collisional transport description. A third form of transport in fusion devices is caused by plasma turbulence mechanisms. This is also referred to as anomalous transport and is beyond the scope of this thesis. In tokamaks, turbulence is known to be the most significant particle and heat transport mechanism. However in stellarators, neoclassical fluxes can be comparable or higher than fluxes generated by

anomalous transport [24]. Neoclassical effects are associated with particle diffusion coefficients that take different forms depending on the plasma collisionality v^*. This normalised quantity corresponds to the ratio between the particles bounce time and the effective collision time for de-trapping. Figure 2.9 shows how the neoclassical particle diffusion coefficient scales with the collisionality in tokamaks and stellarator. Trapped fast particles such as alphas and ICRF heated ions will usually bounce a few times before becoming passing because of Coulomb collisions and are subjected to low collisionality regimes ($v^* << 1$). It is seen that stellarators possess very high transport level for these types of particle ($\sqrt{v^*}$ and $1/v^*$ regimes). In comparison, for the same collisionality, neoclassical transport in tokamaks (banana regime) is quite low.
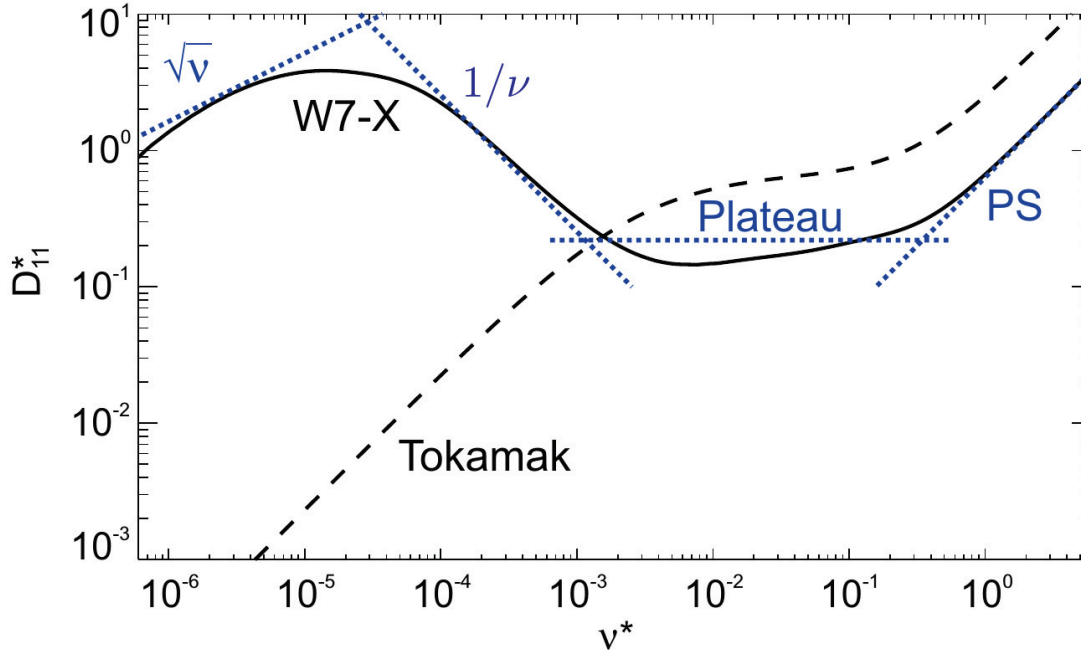
Figure 2.9: Particle diffusion coefficient in tokamak (dashed line) and in W7-X (solid line) with respect to the plasma collisionality. Courtesy of Ref. [24].

Ambipolar particle diffusion in tokamaks and stellarators

Fick's law can be invoked in order to write down the diffusion equation for particles and energy. Consider a plasma volume with temperature T and density n, the particle and energy fluxes for ions (i) and electrons (e) read:

$$\mathbf{\Gamma_{i,e}} = -D_{i,e}\nabla n_{i,e} \quad \text{(particle flux)}, \tag{2.26}$$

$$\mathbf{Q_{i,e}} = -\chi_{i,e}\nabla T_{i,e} \quad \text{(energy flux)}. \tag{2.27}$$

In these equations, $D_{i,e}$ is the particle diffusion coefficient and $\chi_{i,e}$ is the heat diffusivity. In this thesis we focus on the transport of particles in toroidal devices. In tokamaks, ions and electrons diffuse at the same rate. This can be shown as in Chapter 8 of Ref. [25] by invoking the conservation of toroidal momentum, therein defined as $P_\varphi = \psi_p - \rho_\parallel$, ensured by the equilibrium axisymmetry. On each flux surface, the total toroidal momentum, i.e. over all species, must be conserved. This can be written as:

$$\frac{\mathrm{d}}{\mathrm{d}t} \sum_s \int \mathrm{d}^3 v P_\varphi f_s(\boldsymbol{x}, \boldsymbol{v}) = 0$$
$$\Rightarrow \sum_s \int \mathrm{d}^3 v P_\varphi \frac{\mathrm{d}}{\mathrm{d}t} f_s(\boldsymbol{x}, \boldsymbol{v}) = 0 \qquad (2.28)$$

Moreover, as the guiding centre drift can be put in a Hamiltonian form, the particle trajectories follow Liouville's equation. The effect of collisions on the distribution function of species "s" is given by the collision operator: $C[f_s]$. A review of the properties of this collision operator can be found in Chapter 2 of Ref. [26]. The time evolution of the distribution function f_s is written as:

$$\frac{\mathrm{d}}{\mathrm{d}t} f_s = C[f_s]. \qquad (2.29)$$

Therefore eq. 2.28 becomes:

$$\sum_s \int \mathrm{d}^3 v \left(\psi_p - \rho_\parallel \right) C[f_s] = 0. \qquad (2.30)$$

The first term can be eliminated because, as shown in Ref. [26], collisions conserve the number of particles: $\int \mathrm{d}^3 v C[f_s] = 0$. Therefore we are left with:

$$\sum_s \int \mathrm{d}^3 v \rho_\parallel C[f_s] = 0. \qquad (2.31)$$

Let us now consider the radial particle flux for each species across a flux surface ψ_p. It is flux averaged as [25]:

$$\overline{\Gamma}_s = \int \int \frac{\mathrm{d}\theta}{2\pi} \mathrm{d}^3 v \frac{f_s \boldsymbol{v} \cdot \nabla \psi_p}{|\nabla \psi_p|} = \pm \frac{1}{4\pi} q \int \int \mathrm{d}\theta \mathrm{d}^3 v \rho_\parallel C[f], \qquad (2.32)$$

where q corresponds to the safety factor and the $\pm$ sign is related to the sign of the particle charge. Combining eqs. 2.31 and 2.32, one shows that electrons and ions indeed diffuse at the same rate. Hence the important result: neoclassical diffusion of species across flux surfaces in tokamaks is intrinsically ambipolar.

Now, in stellarators the toroidal angular momentum is not a constant motion because the equilibrium is not toroidally symmetric. Therefore an electric field must arise in order to restore the ambipolarity and prevent charge separation. Early theoretical derivations pre-

sented in Ref. [27] showed that a purely radially dependent electric potential $\Phi(\psi_p)$ can restore ambipolarity. It was also shown in the latter that on each flux surface, the diffusion of ions and electrons do not necessarily occur at the same rate for all values of Φ. However it was suggested that one can impose on each flux surface the ambipolar condition:

$$\Gamma_e = Z_i \Gamma_i, \tag{2.33}$$

in order to solve for a self-consistent ambipolar potential Φ. Solving for the roots of this equation allows determination of possible ambipolarity regimes, and determination of self-consistent particle and heat transport coefficients. In Ref. [28], the calculation of such regimes was extended by considering several collisionality regimes (e.g. $1/\nu^*$, $\sqrt{\nu^*}$, ν^*). In general, eq. 2.33 has three roots as indicated in Fig. 2.10. The first and negative root Φ_1 generates an inward pointing electric field and corresponds to the so-called ion-root regime where ions are held back in the plasma by electrons. The second large positive root Φ_2 yields the opposite regime to that of Φ_1, producing the electron-root regime. There exists a third root Φ_3 for slightly positive potential. As mentioned in Ref. [28], but also in [29] where the topic of ambipolar diffusion in non-axisymmetric devices is discussed at length, this root is thermodynamically unstable: a small decrease (respectively increase) in the positive charges in the considered local volume will cause the electric potential to bifurcate towards the negative (resp. positive) root. The electron-root regime is typically achieved in relatively low density and high electron temperature plasma, i.e. with a strong central ECRH power applied. This is the regime expected in the present early operation phase of W7-X. On the other hand, the ion-root requires high ion temperature and is expected to dominate with NBI and ICRF heating. Indeed the dominantly poloidal $\boldsymbol{E} \times \boldsymbol{B}$ drift caused by the radial electric field helps to restore some symmetry in the trapped particles orbit and improve their confinement. It will be seen in Chapter 3.6 that the radial electric arising in this regime appears crucial in simulations of fast ions generation scenarios in W7-X.
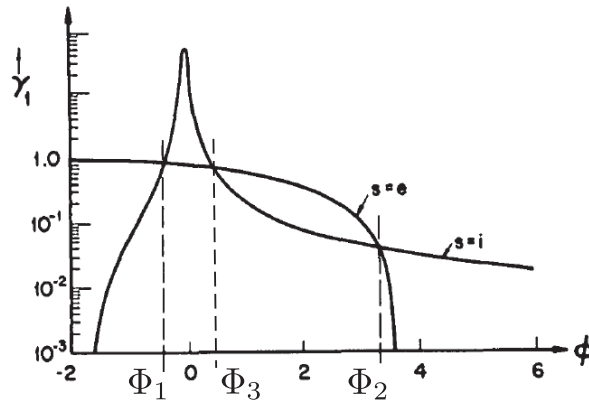

Figure 2.10: Normalised ion and electron particle flux ($\gamma_{i,e}$) as a function of the radial electric potential. Courtesy of Ref. [28].

2.2 Plasma interaction with waves in the Ion-Cyclotron Range of Frequency

One of the main topics of this thesis is the plasma interaction with electromagnetic waves in the Ion-Cyclotron Range of Frequency (ICRF). In this section, the basic principles of the propagating waves in plasmas and the absorption regimes of ICRF waves are reviewed.

2.2.1 Waves in plasmas

Magnetised plasmas can carry different types of electromagnetic or electrostatic waves. The accessible modes that can be carried by the plasma can be found by determining the corresponding dispersion relation that relates the wave frequency ω and wave number k. As they propagate, plasma waves typically induce oscillations of the plasma species and of the confining magnetic field lines. Therefore plasma waves are classified based on the oscillating plasma species (electrons or ions) and on the direction of propagation (determined by the wave vector $\boldsymbol{k}$) with respect to the equilibrium magnetic field. Such classifications can be found for example in Ref. [30].

Dispersion relations for plasma waves can be obtained using Maxwell's equations:

$$\nabla \cdot \boldsymbol{D} = \rho_{ant} \tag{2.34a}$$

$$\nabla \cdot \boldsymbol{B} = 0 \tag{2.34b}$$

$$\nabla \times \boldsymbol{E} = -\frac{\partial \boldsymbol{B}}{\partial t} \tag{2.34c}$$

$$\nabla \times \boldsymbol{B} = \mu_0 \left(\frac{\partial \boldsymbol{D}}{\partial t} + \boldsymbol{j}_{ant} \right). \tag{2.34d}$$

In these equations, ρ_{ant} and $\boldsymbol{j}_{ant}$ are respectively the charge and current density on the antenna, i.e. the source of the wave excitation outside the plasma. The electric displacement field $\boldsymbol{D}$ is related to the waves electric field $\boldsymbol{E}$ by an internal plasma current term generated by the wave propagation:

$$\boldsymbol{D} = \epsilon_0 \boldsymbol{E} + \frac{i}{\omega} \boldsymbol{j}. \tag{2.35}$$

In this equation, for stationary and homogeneous plasmas, the current density is linearly related to the waves electric field by the Ohm's:

$$\boldsymbol{j} = \overline{\overline{\sigma}} \cdot \boldsymbol{E}, \tag{2.36}$$

where $\overline{\overline{\sigma}}$ is the conductivity tensor. Combining eqs. 2.35 and 2.36, one can define the dielectric tensor $\overline{\overline{\varepsilon}}$:

$$\boldsymbol{D} = \epsilon_0 \left(\overline{\overline{I}} + \frac{i}{\epsilon_0} \overline{\overline{\sigma}} \right) \cdot \boldsymbol{E} = \epsilon_0 \overline{\overline{\varepsilon}} \cdot \boldsymbol{E}, \tag{2.37}$$

where $\overline{\overline{I}}$ is the unit dyadic. The dielectric tensor is a crucial quantity in plasma wave physics because it contains all the information about the wave propagation and absorption by the plasma. The wave equation is obtained by the standard procedure, i.e. Fourier decomposing Maxwell's equations and manipulating the curl of eq. 2.34c:

$$\left(\boldsymbol{kk} - k^2 \overline{\overline{I}} + \frac{\omega^2}{c^2} \overline{\overline{\varepsilon}} \right) \cdot \boldsymbol{E} = \overline{\overline{M}} \cdot \boldsymbol{E} = 0. \tag{2.38}$$

The general dispersion relation is finally obtained by looking for the solution of the equation:

$$Det \left[\overline{\overline{M}} \right] = 0. \tag{2.39}$$

The dielectric tensor elements are then derived according to the chosen plasma model. The plasma wave modes "allowed" to propagate are obtained by inserting the dielectric tensor elements in eq. 2.39. The dispersion relation is usually manipulated in order to write $k_\perp^2$ as a function of the wave frequency and the plasma parameters. This equation captures the crucial interaction between the plasma and the wave, i.e. cut-offs ($k_\perp^2 = 0$) and resonances ($k_\perp^2 \to 0$). A quite exhaustive classification of the plasma waves can be found in Ref. [30]. Here we will briefly discuss the low frequency waves, i.e. below and around the ion-cyclotron frequency. For a very good review on low frequency waves in plasmas, the reader is referred to Ref. [31]. In the cold plasma model, the ideal two-fluid (electrons and one ionic species) MHD equations are used. In the Alfvén range of frequencies ($\omega < \omega_{ci}$), two modes co-exist: the fast magneto-sonic wave and the shear Alfvén wave. As the wave frequency approaches ω_{ci}, only the fast magneto-sonic wave can propagate and is the relevant mode for interactions with plasma ions.

The cold plasma model does not take into account the particles velocity distribution. The warm plasma model can then be used in order to take into account some kinetic effects. In the warm plasma model, the dielectric tensor elements have to be derived using the distribution function of each species. The distribution is approximated by a Maxwellian with characteric temperature T:

$$\mathscr{F}_M(\boldsymbol{x}, \boldsymbol{v}) = n(\boldsymbol{x}) \left(\frac{2m}{\pi T} \right)^{3/2} e^{-\frac{2mv^2}{T}}, \tag{2.40}$$

where $n(\boldsymbol{x})$ is the particle density. The warm plasma model allows the description of additional physical phenomena such as, for example, the Landau damping.

2.2.2 Plasma heating with ICRF waves

The absorption of RF waves by the plasma species occurs via a wave-particle resonant interaction. This interaction may take place where the relevant resonance condition is valid. The

general cyclotron resonance we are interested in reads:

$$\omega - k_\parallel v_\parallel - n\omega_c = 0. \tag{2.41}$$

In this equation, $k_\parallel = \boldsymbol{k} \cdot \boldsymbol{B}/B$, and n is an integer. Landau damping will occur for the resonance condition with $n = 0$. In this work we will focus on the fundamental resonance $n = 1$. The second harmonic $n = 2$ and higher harmonic resonances are beyond the scope of this thesis.

Let us focus on the question of heating ions with a fast wave at the fundamental resonance. Following the seminal paper by Stix [32] which contains a broad discussion of ICRF heating, the electric field components perpendicular to the magnetic field can be decomposed into two circularly polarised components noted: E^+ and E^-. The E^+ component is of most importance for ICRF heating because it is the component that rotates in the same direction as the ion cyclotron motion and is therefore responsible for ion acceleration. Indeed, as the fundamental resonance condition is met, the resonant ions and the E^+ field rotate in phase in the wave frame of reference. It is shown in this case that the E^+ field accelerates the particle in the perpendicular direction as illustrated in Fig. 2.11. A very good review of the many wave-particle interactions is found in Ref. [33].
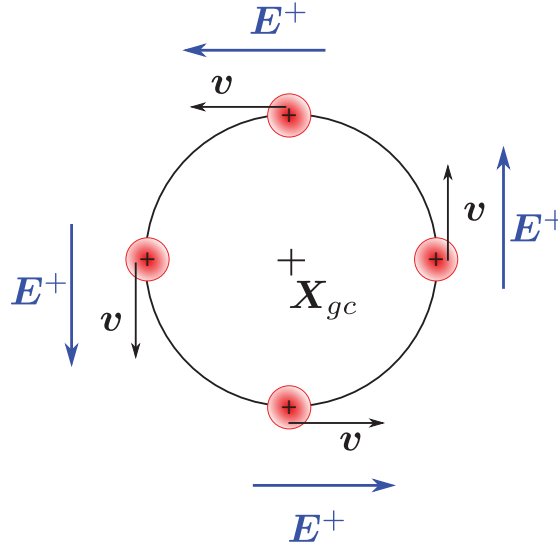
Figure 2.11: Schematic of a positive ion being accelerated by the E^+ field at the fundamental cyclotron resonance.

However, efficient ICRF heating also depends on the wave polarisation, i.e. the ratio E^+/E^- at the wave-particle resonance position. It can be shown that the wave polarisation for cold plasma model can be written as:

$$\left| \frac{E^+}{E^-} \right| = \left| \frac{\omega - \omega_{ci}}{\omega + \omega_{ci}} \right|. \tag{2.42}$$

Therefore it seen that at the resonance position $E^+ = 0$, first harmonic ICRF heating of a

single ion species plasma is not possible within the cold plasma model. Let us recall that the cold plasma model does not take into account thermal effects. Therefore moving to the warm plasma model, it would be possible (with a hot enough plasma) to Doppler shift the resonance position away from the "bad" polarisation position and still get some wave absorption. However the amplitude of E^+ still remains low for efficient bulk plasma heating. Nevertheless, this scheme can be used ICRF acceleration of Neutral Beam Ions which possess a very high parallel velocity (in the case of tangential injection).

An alternative scheme for plasma heating with ICRF waves, which is most commonly applied in plasma devices, is the so-called minority heating scenario. It consists of introducing in the plasma a second ionic species in low concentration. In that situation, the existence of the so-called mode conversion layer and the ion-ion hybrid resonance near the minority cyclotron resonance dictates the polarisation of the wave such that it is no longer exactly wrong at the minority ion resonance position. Good absorption of the wave energy by the minority species is therefore possible. The heating energy is then transferred to the bulk electrons and ions by Coulomb collisions with the minority ions. In deuterium or deuterium-tritium plasmas, good candidates for playing the role of the minority species are hydrogen or helium-3. This scheme is commonly used in present tokamaks (e.g. JET [34] and ASDEX upgrade [35]) and in stellarators (e.g. LHD [36, 37]) and is foreseen as the main ICRF heating scheme in ITER [38]. In Chapter 3.6, we investigate the possibility of using this scheme in the W7-X stellarator. The minority heating scheme is usually elaborated such that most of the wave is absorbed by the minority species. This occurs for relatively low concentrations, e.g. $n_H/n_e \sim 5\%$ or less. At high concentration, the wave is not efficiently absorbed by the minority species, and travels through the mode conversion layer. In this region the fast wave becomes evanescent and is converted into short wave length modes such as the Ion Bernstein Wave (IBW), hence the name. These waves are usually absorbed by electrons and experimental exploration of the mode conversion scheme for bulk electron heating can be found for example in Ref. [39, 40]. Finally, a new ICRF scheme, similar to minority heating but involving three ionic species, has recently been developed [41]. This scheme aims at maximising the power absorption by the species introduced at very low concentration (< 0.1%). A more detailed explanation and some modelling of this scenario is presented in chapter 4.6.

2.3 Self-consistent solution to a non-linear problem

In the previous section we briefly described the many interactions between charged particles that form the plasma and the confining magnetic field and waves in the Ion-Cyclotron Range of Frequency. Fusion devices must employ carefully designed magnetic fields in order to confine drifting particles, and maintain the plasma in the vacuum vessel. In addition, the plasma must be heated up to several keV in order to reach fusion relevant temperatures. Considering the number of particles involved in such a system, it is convenient to describe the plasma using statistical tools in order to understand and predict experimental observations. In the case of a minority heating scheme, the distribution function in phase-space (position and

velocity) $f(\boldsymbol{x}, \boldsymbol{v})$ is used for the mathematical description of the minority ion population. The Vlasov-Boltzmann equation describes the time evolution of this distribution function while taking into account the ambient magnetic equilibrium, the ICRF wave and Coulomb collisions with the background species:

$$\frac{\partial f}{\partial t} + \boldsymbol{v} \cdot \frac{\partial f}{\partial \boldsymbol{x}} + \frac{q}{m} (\boldsymbol{E} + \boldsymbol{v} \times \boldsymbol{B}) \cdot \frac{\partial f}{\partial \boldsymbol{v}} = \left. \frac{\partial f}{\partial t} \right|_C . \tag{2.43}$$

In this equation, the $\boldsymbol{E}$ and $\boldsymbol{B}$ contain contributions from equilibrium fields (radial electric field arising from neoclassical transport in 3D plasmas and confining magnetic field) and the ICRF electromagnetic wave. Under the influence of this wave the resonant particles distribution develops a fast ion tail. The ions forming this part of the distribution are known to reach energies above a few hundred of keV in typical JET plasmas. The Coulomb collisions between these energetic particles and the background species are known to be dominated by slowing down interaction with electrons. Since pitch-angle scattering is quite inefficient and since wave-particle interaction occurs mainly in the perpendicular direction, it follows that the tail of the minority distribution contains more perpendicular than parallel energy. An example of a heated minority distribution in a JET plasma with 3 MW of ICRF power is illustrated in Fig. 2.12. The thermal and the fast components of this distribution are clearly distinguishable in this example and they cannot be described with the same distribution model. A Maxwellian model, as given in eq. 2.40 is appropriate for the modelling of the thermal part. However, another model must be used for the fast tail in order to take into account the anisotropy caused by ICRF heating.
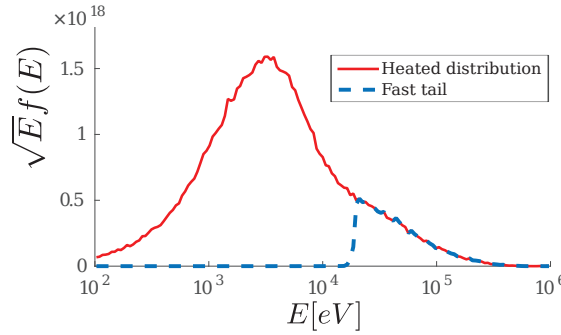
Figure 2.12: ICRF heated distribution function (red line). The fast tail component (highlighted by the dashed blue line) appears clearly.

2.3.1 A nearly bi-Maxwellian distribution

A suitable way to describe the fast tail of the minority distribution is to use the so-called bi-Maxwellian distribution. This model was introduced in Ref. [42–44] and reads:

$$\mathscr{F}_h \left(\overline{\psi}_p, E, \mu \right) = \mathscr{N}(\overline{\psi}_p) \left(\frac{m}{2\pi T_\perp(\overline{\psi}_p)} \right)^{3/2} e^{-\left(\frac{\mu B_c}{T_\perp(\overline{\psi}_p)} + \frac{|E - \mu B_c|}{T_\parallel(\overline{\psi}_p)} \right)}, \tag{2.44}$$

where $\overline{\psi}$ corresponds to the average flux surface occupied by the particles along their unperturbed trajectories. B_c is a critical value of the magnetic field that in the context of ICRF heating is equal to the resonant magnetic field. $\mathcal{N}$ is a function related to the density of fast particles, $T_\perp$ and $T_\parallel$ are respectively temperature in the perpendicular and parallel direction to the magnetic field. The definition of these quantities are also found in Ref. [44]. This model allows inclusion of on one the hand of the anisotropy previously mentioned via $T_\perp$ and $T_\parallel$ but also its localisation. Indeed, the B_c parameter introduces a spatial dependency in the bi-Maxwellian function which attempts to model the wave power deposition that predominantly occurs in the Doppler broadened resonance layer. This bi-Maxwellian function (eq. 2.44) was constructed in order to verify the lowest order Vlasov equation $\boldsymbol{B} \cdot \nabla \mathscr{F}_H = 0$. The model therefore appears to contain the essential parameters to describe an ICRF generated fast ion distribution. As it shall be seen in the following, moments of $\mathscr{F}_h$ can be used in order to correct the MHD equilibrium and the wave propagation.

2.3.2 The `SCENIC` package

The fast ion population develops significant localised pressure which can be of the order of the bulk plasma pressure and current densities. The magnetic equilibrium is therefore expected to be influenced by the formation of the fast tail. In addition, the localisation of particles along the resonance layer due to ICRF trapping and the development of pressure predominantly in the direction perpendicular to the magnetic field influences the plasma dielectric tensor, which in turn dictates the ICRF wave propagation and absorption. Equation 2.43 therefore appears as a highly non-linear problem. Hence, development of a self-consistent numerical tool for the precise description of ICRF heated plasma scenarios while taking into account the interplay between the wave field, distribution function and magnetic equilibrium is required. The `SCENIC` package has been built for that purpose. The main codes that comprise this package and the iterative procedure required for the calculation of the self-consistent solution are discussed hereafter.

The `ANIMEC` code

The ideal MHD equilibrium is solved by the `ANIMEC` code [11]. As mentionned earlier, this is an extension of the `VMEC` code [10] which aims at including the contribution from the fast particles typically generated by ICRF heating. The `ANIMEC` code uses a steepest-descent method in order to minimise the plasma energy functional (eq. 2.12), but with a generalisation to include anisotropic pressure:

$$W = \int_V \mathrm{d}^3 x \left(\frac{B^2}{2\mu_0} + \frac{p_\parallel}{\Gamma - 1} \right) \tag{2.45}$$

The calculation grants access to crucial equilibrium quantities such as the spatial magnetic field amplitude and flux surface geometry. These quantities are obtained by their Fourier

series decomposition in the poloidal and toroidal variables. For example, assuming stellarator symmetry (up-down symmetry in tokamaks for the case $n = 0$):

$$B(s, u, v) = \sum_{mn} B_{mn}(s) \cos(mu - nv), \tag{2.46a}$$

$$R(s, u, v) = \sum_{mn} R_{mn}(s) \cos(mu - nv), \tag{2.46b}$$

$$Z(s, u, v) = \sum_{mn} Z_{mn}(s) \sin(mu - nv). \tag{2.46c}$$

In `ANIMEC` , a magnetic flux coordinate system (s, u, v) is used, where the radial variable $s = \rho^2 = \psi_t / \psi_{t,edge}$ is the normalised toroidal magnetic flux, u is a poloidal angle that minimises the number of poloidal modes in the equilibrium decomposition, and v is the geometric toroidal angle. The contribution of both the thermal (Maxwellian) and hot (bi-Maxwellian) species are included in the equilibrium calculation. Moments of the corresponding distribution functions (eqs. 2.40 and 2.44) are therefore needed. In the presence of ICRF heating for example, the anisotropy develops predominantly in the Doppler broadened resonance layer. Therefore the parallel pressure (eq. 2.45) is not a flux surface quantity and reads:

$$p_\parallel(\bar{s}, B) = p(\bar{s}) + p_\parallel^h(\bar{s}, B). \tag{2.47}$$

The $\bar{s}$ notation is adopted for consistency with the bi-Maxwellian model given by eq. 2.44. In eq. 2.47, $p(\bar{s})$ denotes the thermal pressure derived from the isotropic Maxwellian background species distribution, and $p_\parallel^h(\bar{s}, B)$ is the parallel pressure moment derived from the anisotropic bi-Maxwellian hot species distribution. This moment can be analytically derived from eq. 2.44:

$$p_\parallel^h(\bar{s}, B) = \mathcal{N}(\bar{s}) T_\parallel(\bar{s}) H(\bar{s}, B), \tag{2.48}$$

where $\mathcal{N}(\bar{s})$ and $T_\parallel(\bar{s})$ are flux surface functions that parametrise the bi-Maxwellian distribution function. Defining the temperature anisotropy $A(\bar{s}) = \frac{T_\perp(\bar{s})}{T_\parallel(\bar{s})}$, one has for $H(\bar{s}, B)$:

$$H(\bar{s}, B) = \begin{cases} \dfrac{B/B_c}{1 - A\left(1 - \frac{B}{B_c}\right)} & \text{if } B > B_c, \\ 1 & \text{if } B = B_c, \\ \dfrac{B}{B_c} \dfrac{1 + A\left(1 - \frac{B}{B_c}\right) - 2A^{5/2}\left(1 - \frac{B}{B_c}\right)^{5/2}}{1 - \left(A\left(1 - \frac{B}{B_c}\right)\right)^2} & \text{if } B < B_c. \end{cases} \tag{2.49}$$

It is recalled that in the context of ICRF heating studies, B_c is constant and equals the resonant magnetic field value B_{res} given by the unshifted cyclotron resonance condition: $\omega_c = \frac{ZeB_{res}}{m}$. However B_c can in general be a three-dimensional function. The density factor $\mathcal{N}(\bar{s})$ is related to the hot particle physical density function $N_h(\bar{s}, B)$ by:

$$n^h(\bar{s}, B) = \mathcal{N}(\bar{s}) A(\bar{s})^{-1/2} \mathcal{C}(\bar{s}, B). \tag{2.50}$$

Here again, the hot particle density is allowed to contain a spatial dependence in order to represent the resonant trapped particles alignment with the resonance layer. It is important to note that the functions H and $\mathscr{C}$ depend intrinsically on $|B|$ (i.e. on the three spatial variables) and are well suited for the modelling of anisotropic ICRF distributions in both two- and three-dimensional equilibria. Finally, the so-called hot pressure scale factor is introduced:

$$p_h(\overline{s}) = \frac{\mathscr{N}(\overline{s})\,T_\parallel(\overline{s})}{p(\overline{s})},$$ (2.51)

which can also be related to the hot particle parallel pressure using eq. 2.48:

$$p_\parallel^h(\overline{s}, B) = p(\overline{s})\,p_h(\overline{s})\,H(\overline{s}, B).$$ (2.52)

Note that the same formulation with arguably more intuitive variables definition is given in Ref. [45]. As `ANIMEC` solves anisotropic equilibria, it also verifies the fire-hose and mirror stability relations [11, 46] as part of the convergence check:

$$\sigma = \frac{1}{\mu_0} - \frac{1}{B}\frac{\partial p_\parallel}{\partial B}\bigg|_s = \frac{1}{\mu_0} - \frac{p_\parallel - p_\perp}{B^2} > 0,$$ (2.53)

$$\tau = \frac{\partial \sigma B}{\partial s}\bigg|_s = \frac{1}{\mu_0} + \frac{1}{B}\frac{\partial p_\perp}{\partial B}\bigg|_s > 0.$$ (2.54)

The `ANIMEC` code typically takes as inputs $p(\overline{s})$, $p_h(\overline{s})$, $A(\overline{s})$, B_c, and the current density $J(\overline{s})$ or the rotation transform $\iota(\overline{s})$. A discussion on the usage J and ι will be found in section 3.2. In this thesis we focus on fixed boundary calculation of the MHD equilibrium which requires a prescription of the shape of the last closed flux surface (LCFS) in terms of its Fourier decomposition (see eqs 2.46b and 2.46c).

Transformation to Boozer coordinates

The coordinate system for the resolution of the self-consistent ICRF distribution function has to be carefully chosen because it can ease the evaluation of certain analytic expressions. In particular the parallel wave vector $k_\parallel$ which is identified with the magnetic operator:

$$i k_\parallel = \frac{1}{B}\boldsymbol{B}\cdot\nabla.$$ (2.55)

So-called straight field lines coordinate systems are particularly well suited for the calculation of this operator since the number of analytic terms are reduced. The magnetic field lines in the `ANIMEC` coordinate system (s, u, v) unfortunately do not show this property, as seen in Fig. 2.13a. In the `LEMan` and `VENUS-LEVIS` codes the Boozer coordinate system (s, θ, φ) [47] is adopted. The mapping of the `ANIMEC` MHD equilibrium onto the Boozer coordinate system is perform by the `TERPSICHORE` code. The primary purpose of `TERPSICHORE` is to compute the stability of 3D ideal MHD equilibria [48]. This problem is more tractable in straight-

field line coordinates and therefore a module to convert the MHD equilibrium computed by `ANIMEC` to Boozer coordinates was implemented. In the `SCENIC` package, `TERPSICHORE` is consequently only used for coordinate transformation. The radial variable s is here the same as the one defined in the `ANIMEC` code, and θ and φ are poloidal and toroidal angles that do not match with the corresponding geometrical angles. Instead, as it is seen in Fig. 2.13b, θ and φ are constructed such that the magnetic field lines appear straight on flux surfaces. Some advantages concerning the expression of the safety factor in such coordinate system was already mentioned (and this is related to the simpler definition of $\boldsymbol{B} \cdot \nabla$. The equilibrium magnetic field can be conveniently written in Clebsch form:

$$\boldsymbol{B} = \nabla\varphi \times \nabla\psi_p(s) + \nabla\psi_t(s) \times \nabla\theta. \tag{2.56}$$

The covariant form of the magnetic field is:

$$\boldsymbol{B} = B_s \nabla s + J(s)\nabla\theta - I(s)\nabla\varphi, \tag{2.57}$$

where $J(s)$ and $I(s)$ are respectively the toroidal and poloidal current fluxes. Introducing the coordinate system jacobian $\sqrt{g} = (\nabla s \times \nabla\theta \cdot \nabla\varphi)^{-1}$ and noting that ∇s, $\nabla\psi_t$, $\nabla\psi_p$ all lie in the same direction, then forming the dot product of eqs. 2.56 and 2.57 gives:

$$B^2 = \frac{\psi'_p J - \psi'_t I}{\sqrt{g}}. \tag{2.58}$$

Note that $\sqrt{g}\, B^2$ is a flux surface quantity in this coordinate system. Moreover it follows from eq. 2.56 that the parallel wave vector now takes the simple form:

$$i k_\parallel = \frac{\psi'_t}{\sqrt{g}\, B} \left(\iota \frac{\partial}{\partial\theta} + \frac{\partial}{\partial\varphi} \right) \tag{2.59}$$

The `TERPSICHORE` code outputs the equilibrium quantities as Fourier decomposition in the poloidal and toroidal direction, i.e. under the form as eqs. 2.46. Note that this representation is constrained by the so-called stellarator symmetry [49] to which the Boozer coordinate system employed here is restricted.
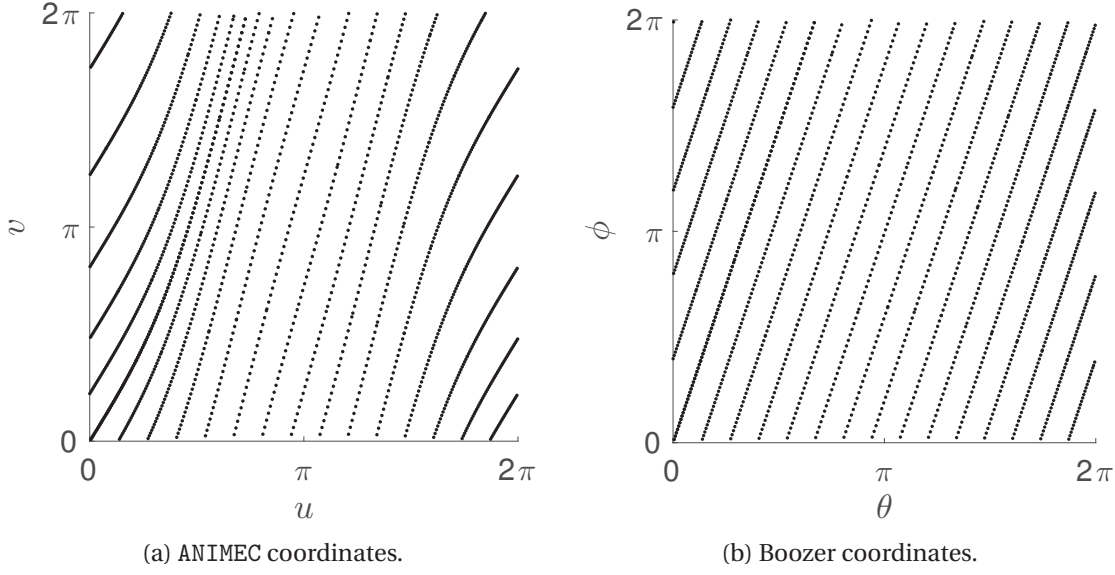
(a) `ANIMEC` coordinates.

(b) Boozer coordinates.

Figure 2.13: Comparison of field lines trajectories on a given flux surface of a tokamak equilibrium in `ANIMEC` and Boozer coordinates systems.

The `LEMan` code

The 3D full wave code `LEMan` (Low-frequency ElectroMagnetic wAve propagatioN) was written in order to solve the propagation of low frequency MHD waves. `LEMan` covers the Alfvén domain up to the ion cyclotron frequency ($\omega \leq \omega_{ci}$). The electromagnetic wave propagation problem mentioned in section 2.2.1 is reformulated in this code in terms of vector and scalar potentials (resp. $\boldsymbol{A}$ and $\tilde{\phi}$) under the Coulomb Gauge choice ($\nabla \cdot \boldsymbol{A} = 0$):

$$\nabla^2 \boldsymbol{A} + k_0^2 \bar{\bar{\epsilon}} \cdot \boldsymbol{A} + i k_0 \hat{\epsilon} \cdot \tilde{\phi} = -\frac{4\pi}{c} \boldsymbol{j}_{ant} \tag{2.60a}$$

$$\nabla \cdot \left(\bar{\bar{\epsilon}} \cdot \nabla \tilde{\phi} \right) - i k_0 \nabla \cdot (\hat{\epsilon} \cdot \boldsymbol{A}) = -4\pi \rho_{ant} \tag{2.60b}$$

In these equations, $\boldsymbol{j}_{ant}$ and ρ_{ant} are the source terms appearing in eqs. 2.34a and 2.34d. As introduced in section 2.2.1, $\bar{\bar{\epsilon}}$ refers to the plasma dielectric tensor. In the first version of the `LEMan` code, the dielectric tensor elements were derived from the cold plasma model [50]. The code was then extended in order to compute the dielectric tensor with the warm plasma model [51]. The contribution of the hot particles modelled by the bi-Maxwellian function to the dielectric tensor was later added [52, 53] and made possible self-consistent inclusion of the `LEMan` code into the `SCENIC` package. It is clear that, in this framework, the dielectric tensor elements carrying the contribution of the hot particles depend on the characteristic parameters of the bi-Maxwellian model, namely $\mathcal{N}(s)$, $T_\perp(s)$, $T_\parallel(s)$ and B_c. Detailed derivation of the dielectric tensor elements for these various models can be found in Ref. [30] and in the appendices of Refs. [52, 54]. In the derivation of the warm and hot dielectric tensor elements the expansion has been truncated to the lowest order in Larmor radius. Therefore only electron Landau damping and fundamental ion cyclotron resonance are resolved.

The wave field computed by `LEMan` is then used by the `VENUS-LEVIS` code to resolve wave-particle interactions via Monte Carlo operators. These operators require in particular the electric field components $E^{+,-}$ and the wave numbers $k_{\parallel,\perp}$. The parallel wave number is usually well approximated in tokamaks by the relation $k_{\parallel} \simeq \frac{n_{\varphi}}{R}$, where R is the major radius and n_{φ} is the considered toroidal mode for the wave description. The mode spectrum of ICRF waves in tokamaks will be further discussed in section 3.1. However such an expression does not take into account the upshift due to the poloidal magnetic field. Also, as it shall be discussed, this relation assumes decoupling between the toroidal modes comprising the wave spectrum. This assumption is however not valid in three-dimensional configurations. A method to evaluate $k_{\parallel}$ which is valid in 3D and consistently include the poloidal upshift was proposed in Ref. [53]. Remembering that in Fourier space $k_{\parallel}$ is a differential operator that can be applied to the scalar potential $\tilde{\phi}$, one can show that:

$$|k_{\parallel}|^2 = \left| \frac{\psi'_t}{\tilde{\phi} B \sqrt{g}} \left(\iota \frac{\partial \tilde{\phi}}{\partial \theta} + \psi'_t \frac{\partial \tilde{\phi}}{\partial \varphi} \right) \right|^2 \tag{2.61}$$

It is also convenient to derive with the same method the perpendicular wave vector:

$$|k_{\perp}|^2 = \left| g^{ss} \frac{1}{\tilde{\phi}} \frac{\partial \tilde{\phi}}{\partial s} \right|^2 + \left| \frac{1}{g^{ss}} \frac{1}{\tilde{\phi} \sigma B \sqrt{g}} \left(\mu_0 J \frac{\partial \tilde{\phi}}{\partial \varphi} + \mu_0 I \frac{\partial \tilde{\phi}}{\partial \theta} \right) \right|^2 \tag{2.62}$$

The `VENUS-LEVIS` code

The `VENUS-LEVIS` code [19] implements a formulation of the first order guiding centre drift equations (GCDE) [12] in general curvilinear coordinates. The GCDE are a system of four equations for the guiding centre position $\boldsymbol{X}_{gc}$ and the parallel gyro-radius $\rho_{\parallel}$:

$$\boldsymbol{X}_{gc} = v_{\parallel} \frac{\boldsymbol{B}^*}{B^*_{\parallel}} + \frac{\boldsymbol{E}^* \times \boldsymbol{B}}{B B^*_{\parallel}}, \tag{2.63a}$$

$$\rho_{\parallel} = \frac{\boldsymbol{E}^* \cdot \boldsymbol{B}^*}{B B^*_{\parallel}}, \tag{2.63b}$$

where:

$$\boldsymbol{B}^* = \boldsymbol{B} + \rho_{\parallel} \nabla \times \boldsymbol{B}, \tag{2.64a}$$

$$\boldsymbol{E}^* = \boldsymbol{E} - \left(\frac{\mu}{q} + v_{\parallel} \rho_{\parallel} \right) \nabla B - \rho_{\parallel} \frac{\partial \boldsymbol{B}}{\partial t}. \tag{2.64b}$$

The `VENUS-LEVIS` code employs a Runge-Kutta method of order 4 to solve these equations in time. In the `SCENIC` framework the curvilinear Boozer coordinates are employed in `VENUS-LEVIS` for consistency with the ICRF wave field given by `LEMan`. In eq. 2.64b, $\boldsymbol{E}$ contains contributions from a slowly varying electric field arising from plasma rotation, neoclassical transport in stellarators or MHD waves. The evaluation of the equilibrium magnetic field in eq. 2.64a and other equilibrium quantities required solving the GCDE by employing a special spline-Fourier

representation using explicitly the Fourier coefficients computed by `TERPSICHORE` , and a cubic spline representation for the radial variable. This method, explained in detail in Ref. [19], brings a level of numerical accuracy and computer resources optimisation which are crucial for the stellarator simulations presented in Chapters 3.6 and 4.6. The `VENUS-LEVIS` code is typically used to evolve minority species ions in a background plasma composed of majority species ions and electrons. The minority ion markers interact with the background species via Coulomb collisions and with the ICRF wave field via resonant wave-particle interaction. These interplays are modelled with Monte Carlo operators. The collision operator is derived from the Fokker-Planck equation and is consistent with the operator introduced in Ref. [55]. The slowing down and pitch angle scattering of the markers on the Maxwellian background species s is implemented by kicks in kinetic energy and pitch angle $\lambda = v_{\parallel}/v$:

$$\Delta\lambda = -\sum_s \nu_\lambda^s \lambda \Delta t + \mathcal{R}_\lambda \sqrt{(1-\lambda^2)\sum_s \nu_\lambda^s \Delta t}, \tag{2.65a}$$

$$\Delta E = -\sum_s 2\nu_E^s \Delta t \left(E - \left(\frac{3}{2} + \frac{E}{\nu_E^s}\frac{\mathrm{d}\nu_E^s}{\mathrm{d}t}T_s\right)\right) + 2\mathcal{R}_E\sqrt{\sum_s \nu_E^s T_s E \Delta t}. \tag{2.65b}$$

In these equations, $\nu_{\lambda,E}^s$ denote the pitch angle scattering and slowing down frequencies respectively, T_s is the temperature of the species s and $\mathcal{R}_{\lambda,E} = \pm 1$ are random signs. The Monte Carlo operator for the resonant ICRF wave-particle interaction is similar to the one described in Ref. [37]. This operator models the heating of resonant particle as a quasi-linear diffusion in velocity space and is consistent with the initial work found in Ref. [56]. The ICRF operator implemented in the `VENUS-LEVIS` code is the same as the one used in the former `VENUS` code [53]. If the Doppler shifted resonance condition 2.41 (with $n \neq 0$) is fulfilled, the marker receives kicks in perpendicular and parallel velocity:

$$\Delta v_\perp = \frac{\langle\Delta v_\perp^2\rangle}{2v_\perp} + \mathcal{R}\sqrt{2\langle\Delta v_\perp^2\rangle}, \tag{2.66a}$$

$$\Delta v_\parallel = \frac{k_\parallel}{\omega_c}v_\perp\Delta v_\perp, \tag{2.66b}$$

with:

$$\langle\Delta v_\perp^2\rangle = \alpha\frac{q^2}{m^2}\tau^2\left|E^+ J_0\left(\frac{k_\perp v_\perp}{\omega_c}\right) + E^- J_2\left(\frac{k_\perp v_\perp}{\omega_c}\right)\right|^2. \tag{2.67}$$

Equation 2.67 is the standard expression for the absolute squared of the change in the perpendicular velocity resulting from the wave-particle interaction, and is directly derived from the quasi-linear theory. In this equation, $E^{+,-}$ are the wave electric field polarised components introduced in section 2.2.2, $J_{0,2}$ are Bessel functions of the first kind, α is a constant factor ensuring a constant power deposition. $\mathcal{R}$ is a uniformly distributed random number in the interval $[0,1]$. The interaction time between the wave and particle is given by τ. A discussion on this parameter is found in Ref. [57] and is taken into account in `VENUS-LEVIS` implementation. It is important to mention here that the form of the Monte Carlo operator allows modelling not only of the heating of the resonant particles (which involves a predominant increase of the

perpendicular energy (eq. 2.66a)), but also the change in the particles orbit due to interaction in the parallel direction (eq. 2.66b). The latter is responsible for radial transport of resonant particles. This effect was introduced in Ref. [58] and will be further discussed in sections 3.4 and 5.2.2.

Fitting on the bi-Maxwellian and the iteration process

The `VENUS-LEVIS` code evolves the minority species ion markers in time and takes into account the confining magnetic field computed by `ANIMEC /TERPSICHORE` , the ICRF wave field computed by `LEMan` and the inter-species Coulomb collisions. In typical minority heating scenarios (e.g. a D rich plasma with 5% H minority), a fast ion tail arises in the energy distribution, above a few hundred keV for tokamak plasmas, because of the ICRF wave-particle interaction. In addition, a large fraction of the markers remains thermal under the predominant influence of slowing down by collisions. An example of the total distribution obtained at the end of a `VENUS-LEVIS` run under these conditions was shown earlier in Fig. 2.12. It is reminded here that because of the large anisotropy developed by the fast tail, the markers forming this part of the distribution are best represented with a bi-Maxwellian model. Therefore, a splitting method is required in order to separate the markers in the thermal part of the distribution from the fast tail. The splitting procedure was introduced in Ref. [53] and consists of comparing the kinetic energy E_i of each marker with the electron temperature at the markers radial position s_i:

$$\text{if: } E_i > x T_e(s_i) \Rightarrow \text{marker } i \text{ is in fast tail,}$$
$$\text{else: marker } i \text{ is in thermal bulk.}$$

In this criterion, x is a constant which is must be adjusted for each simulation. The thermal bulk distribution is well modelled by a Maxwellian distribution. Therefore the contribution to the MHD equilibrium and wave field from the thermal minority markers is accounted for by introducing the density, pressure and temperature of the thermal bulk into the MHD balance equation and the dielectric tensor. The 0th (density n_{th}) and 2nd (pressure p_{th}) order velocity moments of the Maxwellian distribution are computed with a Particle-In-Cell method applied to the thermal marker distribution:

$$n_{th}(s) = 2\pi \int_\theta \int_\varphi \int_E \int_\lambda \mathrm{d}\theta \mathrm{d}\varphi \mathrm{d}E \mathrm{d}\lambda \sqrt{g}_v \mathscr{F}_M\left(s,\theta,\varphi,E\right) \bigg/ \int_\theta \int_\varphi \mathrm{d}\theta \mathrm{d}\varphi \sqrt{g} \tag{2.68a}$$

$$= \sum_{i \in \Upsilon_t} \frac{w_i}{\Delta V} \tag{2.68b}$$

$$p_{th}(s) = 2\pi \int_\theta \int_\varphi \int_E \int_\lambda \mathrm{d}\theta \mathrm{d}\varphi \mathrm{d}E \mathrm{d}\lambda \sqrt{g}_v E \mathscr{F}_M\left(s,\theta,\varphi,E\right) \bigg/ \int_\theta \int_\varphi \mathrm{d}\theta \mathrm{d}\varphi \sqrt{g} \tag{2.69a}$$

$$= \sum_{i \in \Upsilon_t} \frac{E_i w_i}{\Delta V} \tag{2.69b}$$

where $\sqrt{g}$ and $\sqrt{g_v}$ are respectively the configuration and velocity space jacobian, w_i is the numerical weight of the considered marker, Υ_t defines the ensemble of markers in thermal bulk ($E_i < x T_e(s_i)$), radially located in the interval $[s - \frac{\Delta s}{2}; s + \frac{\Delta s}{2}]$ with Δs the radial bin width, and ΔV is the plasma volume contained in this interval. The temperature of the thermal bulk T_{th} is simply obtained by the relation $p_{th} = n_{th} T_{th}$ which is valid for Maxwellian distribution. The numerical evaluation of the moments of the bi-Maxwellian distribution is also based on a Particle-In-Cell method. However it is not as straightforward to obtain the relevant quantities that will be read by `ANIMEC` and `LEMan` , namely the anisotropy $A(\overline{s}) = T_\perp(\overline{s}) / T_\parallel(\overline{s})$, $p_h(\overline{s})$, $T_\parallel(\overline{s})$ and $\mathcal{N}(\overline{s})$. First the hot particle density, as well as parallel and perpendicular pressures are needed:

$$n^h\left(\overline{s}, \theta, \varphi\right) = \sum_{i \in \Upsilon_f} \frac{w_i}{\delta V}, \tag{2.70}$$

$$p_\parallel^h\left(\overline{s}, \theta, \varphi\right) = \sum_{i \in \Upsilon_f} \frac{v_\parallel^2 w_i}{\delta V}, \tag{2.71}$$

$$p_\perp^h\left(\overline{s}, \theta, \varphi\right) = \sum_{i \in \Upsilon_f} \frac{v_\perp^2}{2} \frac{w_i}{\delta V}. \tag{2.72}$$

In these equations, Υ_f denotes the ensemble of fast particles ($E_i > x T_e(\overline{s}_i)$) which are located in the three-dimensional bin of volume δV defined by the intervals $[\overline{s} - \frac{\Delta \overline{s}}{2}; \overline{s} + \frac{\Delta \overline{s}}{2}]$, $[\theta - \frac{\Delta \theta}{2}; \theta + \frac{\Delta \theta}{2}]$, $[\varphi - \frac{\Delta \varphi}{2}; \varphi + \frac{\Delta \varphi}{2}]$. The temperature anisotropy is found by inverting the relation [53]:

$$\frac{p_\perp^h}{p_\parallel^h} = M(\overline{s}, A, B), \tag{2.73}$$

with:

$$M(\overline{s}, A, B) = \begin{cases} A\frac{B}{B_c}\left(1 - A(1 - B/B_c)^{-1}\right) & \text{if } B > B_c, \\ A\frac{B}{B_c}\frac{(1+A(1-B/B_c))^2 - 5(A(1-B/B_c))^{3/2} + (A(-B/B_c))^{7/2}}{(1-A^2(1-B/B_c)^2)(1+A(1-B/B_c)-2(A(1-B/B_c)))^{5/2}} & \text{if } B < B_c. \end{cases} \tag{2.74}$$

The result of this inversion has to be flux surface averaged so that A is a flux function. The anisotropy A and the parallel pressure $p_\parallel^h$ can be injected in eqs 2.50, 2.51 and 2.52 to obtain:

$$p_h(\overline{s}) = \left\langle \frac{p_\parallel^h\left(\overline{s}, \theta, \varphi\right)}{p(\overline{s}) H(\overline{s}, B)} \right\rangle, \tag{2.75a}$$

$$\mathcal{N}(\overline{s}) = \left\langle \frac{p_\parallel^h\left(\overline{s}, \theta, \varphi\right)}{p(\overline{s}) C(\overline{s}, B)} \right\rangle, \tag{2.75b}$$

$$T_\parallel(\overline{s}) = \left\langle \frac{p_\parallel^h\left(\overline{s}, \theta, \varphi\right)}{\mathcal{N}(\overline{s}) H(\overline{s}, B)} \right\rangle, \tag{2.75c}$$

where the angular brackets stand for flux surface averaging. There parameters, along with a choice of B_c, completely determine the model of the anisotropic distribution function. Equa-

tions 2.73 (inversion for A), and 2.75 are computed by a dedicated routine in the `VENUS-LEVIS` code and are then read by `ANIMEC` and `LEMan` . The MHD equilibrium and wave field are updated to take into account the heating of the minority distribution. Several iterations between `ANIMEC` /`TERPSICHORE` , `LEMan` , and `VENUS-LEVIS` are performed until a self-consistent distribution function is obtained, i.e. until no reasonable change in the heated distribution function appears between successive iterations. This iterative process will be more clearly illustrated in chapters 2.4 and 4.6.

2.4 Summary

In this chapter, the plasma physics principles relevant for the understanding and usage of the `SCENIC` code package was presented. The `SCENIC` modelling tool is probably unique in the sense that it can resolve fundamental ICRF heating scenarios including consistent finite orbit width effects, warm plasma effects and fully three-dimensional configurations.

In the following chapters, the modelling capabilities of the `SCENIC` package will be demonstrated. It should also appear that, throughout this thesis, no significant development in the physical basis `SCENIC` has been made, but the code has been used successfully to explore novel three-dimensional equilibrium configurations, in particular the W7-X stellarator, and ICRF fundamental heating scenarios.

3 Two-Dimensional configurations: ICRF for sawtooth control experiments in the JET tokamak

In this chapter we present how `SCENIC` has been used for the interpretation of experimental scenarios. The experiments at stake were conducted in the JET tokamak where ICRF minority heating was mainly used for controlling MHD activity. An important aspect of using ICRF waves in these experiments was the question of the antenna phasing. This terminology relates to the working of the physical RF antenna, which is the actual heating source, and the preferred direction of propagation of the excited wave in the plasma. The concept and the corresponding modelling method employed in this work will be described in detail in section 3.1. The experimental signals obtained during the JET experimental pulse #84497 where sawteeth were controlled by ICRF heating serve as the basis of our modelling presented here. The corresponding numerical profiles and equilibrium will be discussed in section 3.2. We study a deuterium rich plasma where the resonant species is Hydrogen introduced at 5% concentration $\left(\frac{n_H}{n_e}\right)$. In section 3.3, the self-consistent distribution function of the heated H ions obtained for various antenna phasings are presented. As it shall be seen, the antenna phasing may result in an asymmetric wave power spectrum which in turn causes a radial displacement of resonant ions. This so-called RF particle pinch, introduced in Ref. [58] and further discussed in Refs. [57, 59, 60], will be presented in section 3.4. The generation of ICRF fast ion population in these experiments were aimed at controlling the amplitude and the period of the sawtooth instability. A brief description of this MHD instability and an explanation of the control method employed will be given in section 3.5.

3.1 Antenna setup

The fast wave used for ICRF applications is coupled to the plasma by an external excitation source. The ICRF antenna system which generates this excitation is composed of straps on which a current density flows. Tokamak antennae are usually located on the LFS of the machine for better accessibility to power sources. As desribed in 2.2.2, the fast wave dispersion relation predicts a cutoff at the LFS. Therefore, the excited wave must first tunnel through an evanescent layer before propagating into the plasma. The plasma-wave coupling can be optimised by placing the antenna as close as possible to the plasma boundary or by puffing

some gas in front of the antenna. The physics of the plasma-wave coupling is complicated not only by the interaction with the edge plasma but also by the antenna structure (e.g. housing, Faraday screen) and geometry. This active field of research usually involves sophisticated modeling tools such as `TOPICA` [61] in order to describe precisely the 3D antenna elements. The antenna solution is then are either coupled to a reduced plasma model or to a full-wave code such as `TORIC` [62]. A somewhat opposite approach is adopted in `SCENIC` and similar other codes (e.g. `SELFO` [57], `EVE` [63]). A simplified antenna model is implemented and the wave propagation and absorption, and the fast ion response is carefully treated. In the following we shall describe how one can take advantage of the toroidal symmetry to conveniently represent the antenna excitation, how this procedure is practically implemented in the `LEMan` code and how various antenna configurations commonly used in tokamak plasma scenarios can be resolved.

General antenna model

The antenna system can be simplified as a current sheet flowing on a metallic strap located at $s = s_{ant}$. This radial position can be realistically viewed as a pseudo-flux surface outside the last closed flux surface. The spatial extension of the antenna can therefore be described independently in all directions (radial, poloidal and toroidal). This convenient representation is adopted for example in the `EVE` code [63] and reads:

$$\boldsymbol{j}_{ant} = \frac{I_0}{\sqrt{g}} \delta\left(s - s_{ant}\right) \sigma_\theta(\theta) \sigma_\varphi(\varphi) \boldsymbol{e}_{ant}. \tag{3.1}$$

In eq. 3.1, I_0 is a constant dictating the excitation amplitude, $\sqrt{g}$ is the coordinate system jacobian. The antenna poloidal and toroidal properties are respectively described by $\sigma_\theta(\theta)$ and $\sigma_\varphi(\varphi)$. $\boldsymbol{e}_{ant}$ is the direction in which the current density flows. This antenna description becomes useful when one considers the mode coupling of the fast wave which depends on the equilibrium plasma geometry. In tokamak plasmas the poloidal modes of the fast wave are strongly coupled because of the inherent poloidal asymmetry of the equilibrium. This coupling is taken into account by the introduction of a poloidally localised simulated antenna as explained in the following. Tokamak plasmas can be approximated to be axisymmetric allowing no coupling between the toroidal modes of the fast wave. In this case, it is therefore valid to consider each toroidal mode of the excitation spectrum independently from one another. Each of these modes can be computed by letting the antenna surround the plasma in the toroidal direction such that one can make use of the Fourier series decomposition of the σ_φ function:

$$\sigma_\varphi(\varphi) = \sum_{n=-\infty}^{\infty} \sigma_n e^{in\varphi}. \tag{3.2}$$

The σ_n coefficients contain all the toroidal features of the antenna such as the geometry and the phasing, which will be detailed in the following. The antenna current density can therefore

be written as:

$$\boldsymbol{j}_{ant} = \frac{I_0}{\sqrt{g}} \delta\left(s - s_{ant}\right) \sigma_\theta(\theta) \sum_{n=-\infty}^{\infty} \sigma_n e^{in\varphi} \boldsymbol{e}_{ant} \tag{3.3}$$

$$= I_0 \sum_{n=-\infty}^{\infty} \sigma_n \overline{\boldsymbol{j}}_{ant,n} e^{in\varphi} \tag{3.4}$$

$$= I_0 \sum_{n=-\infty}^{\infty} \boldsymbol{j}_{ant,n} e^{in\varphi}. \tag{3.5}$$

The decoupling of toroidal modes also allows for the Fourier decomposition of the wave electric field:

$$\boldsymbol{E}(s,\theta,\varphi) = I_0 \sum_{n=-\infty}^{\infty} \boldsymbol{E}_n(s,\theta) e^{in\varphi} = I_0 \sum_{n=-\infty}^{\infty} \sigma_n \overline{\boldsymbol{E}}_n(s,\theta) e^{in\varphi}. \tag{3.6}$$

In 3.6, $\overline{\boldsymbol{E}}_n$ is the electric field that is usually from wave code calculation. Moreover the power coupled by the antenna to the plasma can be written as [50]:

$$\begin{aligned}
P_{ant} &= \frac{i}{2} \int_s \int_\theta \int_\varphi \mathrm{d}s\mathrm{d}\theta\mathrm{d}\varphi \sqrt{g}\, \boldsymbol{j}_{ant} \cdot \boldsymbol{E}^* \\
&= \frac{i}{2} \int_s \int_\theta \int_\varphi \mathrm{d}s\mathrm{d}\theta\mathrm{d}\varphi \sqrt{g} \sum_{n=-\infty}^{\infty} I_0 \sigma_n \overline{\boldsymbol{j}}_{ant,n} e^{in\varphi} \cdot \sum_{n'=-\infty}^{\infty} I_0 \sigma_{n'}^* \overline{\boldsymbol{E}}_{n'}^* e^{-in'\varphi} \\
&= I_0^2 \sum_{n=-\infty}^{\infty} \sum_{n'=-\infty}^{\infty} \frac{i}{2} \int_s \int_\theta \int_\varphi \mathrm{d}s\mathrm{d}\theta\mathrm{d}\varphi \sqrt{g} \, |\sigma_n|^2 \overline{\boldsymbol{j}}_{ant,n} \cdot \overline{\boldsymbol{E}}_{n'}^* e^{i(n-n')\varphi}.
\end{aligned} \tag{3.7}$$

After integrating over φ in 3.7, only the $n = n'$ terms remain because of the oscillating term $e^{i(n-n')\varphi}$ so that:

$$P_{ant} = I_0^2 \sum_{n=-\infty}^{\infty} |\sigma_n|^2 \frac{i}{2} \int \mathrm{d}s\mathrm{d}\theta \sqrt{g}\, \overline{\boldsymbol{j}}_{ant,n} \cdot \overline{\boldsymbol{E}}_n^* = I_0^2 \sum_{n=-\infty}^{\infty} |\sigma_n|^2 P_{ant,n}. \tag{3.8}$$

The imaginary component of P_{ant} corresponds to the resistive coupled power, i.e. the actual absorbed power by the plasma. Eq. 3.8 is relevant for identifying a particular toroidal mode that contributes dominantly to the wave spectrum. Each antenna configuration can be characterised by the values of the $|\sigma_n|^2$ coefficients as we shall see in Fig. 3.2.

Implementation in LEMan

This procedure appears to allow a straightforward computation of each Fourier component of the electric field via a wave code, including a consistent reconstruction of the antenna configuration, i.e. using the σ_n coefficients. However it is not convenient to implement directly in LEMan the σ_φ function as given by eq. 3.2. The first reason is that if one wants to compare different antenna geometry and/or phasing, a direct implementation will imply that all toroidal modes have to be re-computed for each investigated antenna configuration. Secondly, the representation of the antenna current density given by eq. 3.1 cannot be easily implemented

into the LEMan code. Indeed, eq. 3.1 assumes that the current sheet flowing on the antenna straps is located in the vacuum region surrounding the plasma. This representation requires the implementation of feeders which take into account the circulation of the excitation current and ensures charge conservation. The LEMan code is written in the Boozer flux coordinate system which limits the investigated domain to span from the magnetic axis up the plasma last closed flux surface, i.e. the vacuum region between the plasma and the wall is not accessible. The modelled antenna is therefore artificially placed inside the last few closed surface of the plasma volume and a perfect plasma-wave coupling is assumed. The antenna is defined in LEMan by the current density $\boldsymbol{j}_{ant}$ in (2.60a). The general expression for $\boldsymbol{j}_{ant}$ is obtained by assuming zero charge accumulation in the antenna circuit, and thus takes the following divergence-free form [50]:

$$\boldsymbol{j}_{ant} = \nabla s \times \nabla \varsigma(s,\theta,\varphi). \tag{3.9}$$

In eq. (3.9), $\varsigma(s,\theta,\varphi)$ is a function describing the localisation and the extension of the antenna excitation and reads :

$$\varsigma\left(s,\theta,\varphi\right) = \varsigma_s\left(s\right)\varsigma_\theta\left(\theta\right)\varsigma_\varphi\left(\varphi\right). \tag{3.10}$$

Eq. (3.10) allows one to define the antenna localisation and extension in each direction independently:

$$\varsigma_s(s) = \left(1 - \left(2\frac{s-s_1}{s_2-s_1}-1\right)^2\right)^2 \mathscr{B}\left(\frac{s-s_1}{s_2-s_1}\right) \tag{3.11a}$$

$$\varsigma_\theta(\theta) = \left(1 - \left(2\frac{\theta-\theta_1}{\theta_2-\theta_1}-1\right)^2\right)^2 \mathscr{B}\left(\frac{\theta-\theta_1}{\theta_2-\theta_1}\right) \tag{3.11b}$$

$$\varsigma_\varphi(\varphi) = e^{in\varphi}. \tag{3.11c}$$

In eq. (3.11), $s_{1,2}$, $\theta_{1,2}$ define the antenna spatial boundaries, n is the considered antenna toroidal mode and $\mathscr{B}$ is the box function defined as:

$$\mathscr{B}(x) = \begin{cases} 1 & \text{if } x \in [0,1] \\ 0 & \text{elsewhere.} \end{cases} \tag{3.12}$$

The amplitude of the raw electric field $\tilde{E}_n$ computed by LEMan for each n has to be to rescaled so that the total electric field given by eq. 3.6 is consistent with the antenna toroidal properties and the desired input RF power. A possible rescaling method consists of considering that the electric for each mode n couples 1 W of power to the plasma:

$$\overline{E}_n = \frac{\tilde{E}_n}{\sqrt{\Im\left(\int \mathrm{d}V\, \boldsymbol{j}_{ant} \cdot \tilde{E}_n^*\right)}}. \tag{3.13}$$

Each electric field amplitude $\overline{E}_n$ is multiplied the coefficient $I_0 \sigma_n e^{in\varphi}$ given by Eq. 3.6. The

summation of these fields give the total electric. This method will be applied in the next paragraph to illustrate the difference between the commonly used antenna phasing (see Fig. 3.2). It is also important to mention that this separation of the toroidal mode numbers is not possible when dealing with a three-dimensional equilibrium. An appropriate method will be explained in section 4.5.1.

Modelling of the JET A2 antenna system

The JET tokamak is equipped with the so-called A2 antennae [64]. Each of these antennae are composed of localised straps carrying currents of the same amplitude but of different phases. The phase shift ϕ_i applying to i^{th} strap of width $\Delta\varphi_i$ located at φ_i is used to change the dominant direction of the wave vector with respect to the plasma current. The main phasing patterns applied to the JET A2 antenna in plasma heating scenarios are the so-called dipole, +90° and -90° phasings. These designations correspond to the phase shift introduced between two adjacent current straps as illustrated in Fig. 3.1.
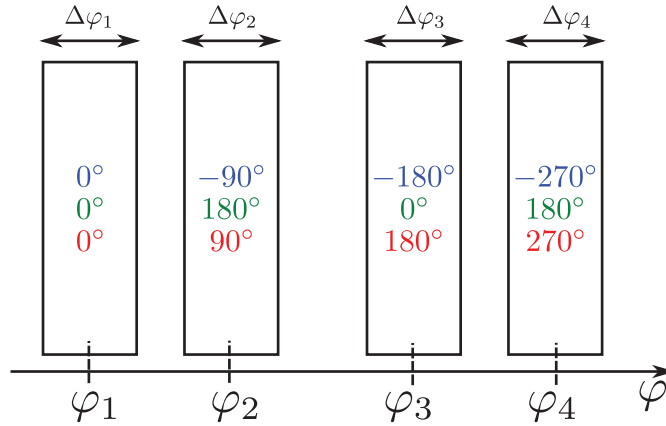
Figure 3.1: Schematic view of the A2 antenna geometry and current straps phasings.

Based on the simplified model of the A2 antenna given in Fig. 3.1, the toroidal variation of the current density can be written:

$$\sigma_\varphi = \sqrt{\frac{2\pi}{4}} \sum_{i=1}^{4} \frac{1}{\sqrt{\Delta\varphi_i}} \mathscr{B}\left(\frac{\varphi - \varphi_i}{\Delta\varphi_i}\right) e^{i\phi_i}. \tag{3.14}$$

The Fourier decomposition of this expression gives the σ_n coefficients introduced in eq. 3.2 and necessary for the wave field reconstruction of a given antenna configuration. By virtue of

the Fourier series decomposition:

$$\sigma_n = \frac{1}{2\pi} \int \sigma_\varphi e^{-in\varphi} \mathrm{d}\varphi$$

$$\sigma_n = \sum_{i=1}^{4} \sqrt{\frac{\Delta\varphi_i}{8\pi}} \operatorname{sinc}\left(\frac{n\Delta\varphi_i}{2}\right) e^{i(\phi_j - n\varphi_i)}, \tag{3.15}$$

equation 3.15 leads to the excitation spectra illustrated in Fig. 3.2. It should be pointed out that this corresponds to the excitation spectra in the vacuum. It is possible to take into account the evanescence of the excitation modes in the scrape-off layer with a back-of-the-envelope correction. The corresponding plasma spectra depend on the scrape-off layer physical properties and can be obtained by wave-plasma coupling calculations. A simplified but yet satisfactory approach to approximate the plasma spectra consist of weighting the contribution of each toroidal mode with a decaying factor $e^{-k_\parallel d}$ ($k_\parallel \simeq n_\varphi / R_{ant}$, with R_{ant} the antenna radial position in the cylindrical coordinate system, and d is the antenna-plasma distance), i.e.:

$$\sigma_\varphi^{plasma}(\varphi) = \sigma_\varphi(\varphi) e^{-k_\parallel d}. \tag{3.16}$$

Moreover, note that +90° and -90° phasings display asymmetric excitation spectrum as suggested by the large peaks around respectively $n_\varphi = -13$ and $n_\varphi = 13$. These phasings are used in order to produce an ICRF wave travelling respectively in the co- and counter- direction with respect to the magnetic field. Considering the plasma spectra seen in Fig. 3.2 (dashed lines), it is reasonable for the sake of this illustration to only retain the modes $|n| < 53$. Figures 3.2b, 3.2d and 3.2f show a reconstruction of the left-handed electric field around the midplane for the different phasings. It is seen that the antenna localisation is retrieved and a privileged direction of propagation, i.e. sign of $k_\parallel$, arises for the +90° and -90° phasings. In practice, only one or two modes which contribute the most to the power spectrum are often sufficient. For SCENIC calculations such as those illustrated here for +90°, -90° and dipole phasings, the wave can be sufficiently modelled for many applications with only, $n_\varphi = -13$, $n_\varphi = 13$, $n_\varphi = \pm 27$. In section 3.4 the impact of the wave directivity on the particle orbits will be discussed.
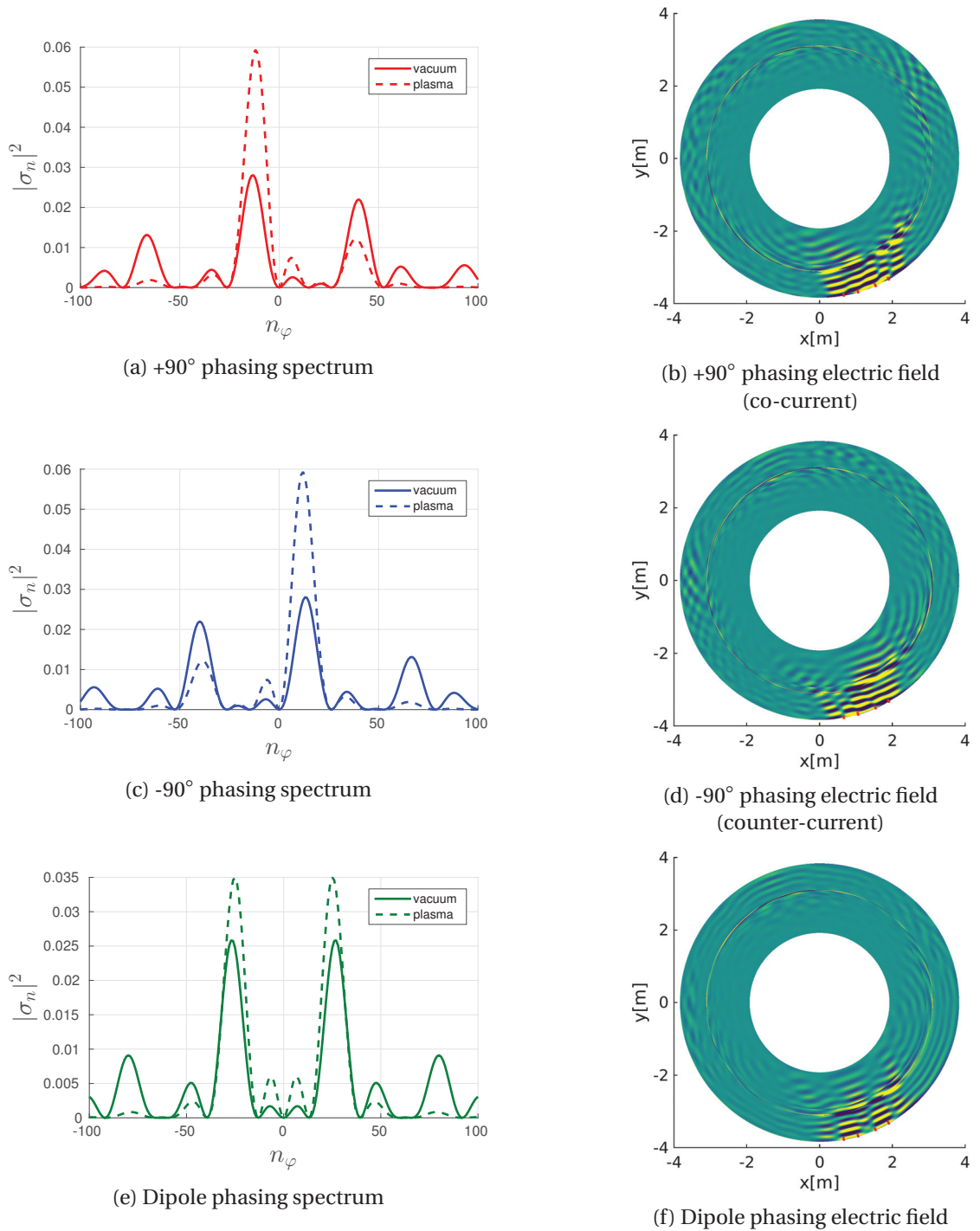
(a) +90° phasing spectrum

(b) +90° phasing electric field (co-current)

(c) -90° phasing spectrum

(d) -90° phasing electric field (counter-current)

(e) Dipole phasing spectrum

(f) Dipole phasing electric field

Figure 3.2: Left: Vacuum and plasma spectra for +90°, dipole and -90° phasings normalised to 1W of input power. Right: Left-handed electric field component E^+ [a.u.] around the torus midplane.

3.2 JET pulse #84497: profiles and equilibrium

The sawtooth control experiments conducted in the JET tokamak in 2013 demonstrated shortening of the sawtooth period with the three phasings discussed in section 3.1. The equilibrium reconstruction which is the basis for the following SCENIC simulations used experimental data for JET pulse #84497. This pulse employed +90° but the plasma configuration is very similar to the other pulses for which −90° and dipole phasings were used. The thermal temperature and density profiles used here were obtained experimental measurement averaged between 54.7s and 55.7s, and are displayed in Fig. 3.3. The assumptions and limitations intrinsic of the

(a) Temperature.
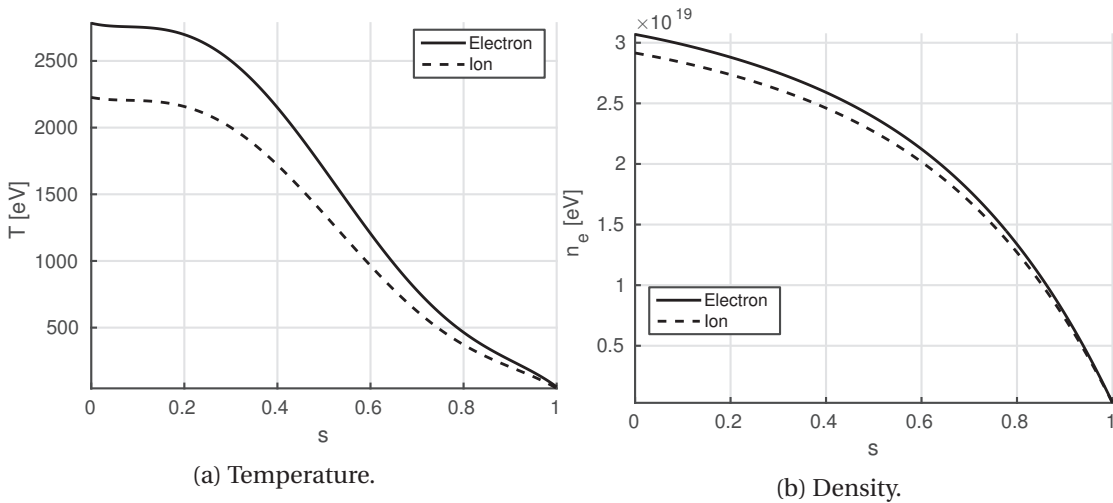
(b) Density.

Figure 3.3: Density and temperature radial profiles of the background deuterium ions and electrons.

SCENIC package led to certain adaptation of the data. In particular as discussed in Chapter 1.4, SCENIC does not allow for an up-down asymmetric plasma, therefore the plasma equilibrium shape that was first obtained from EFIT [5, 6] had to be reshaped. Figure 3.4a compares the LCFS as given by EFIT and the one used in the SCENIC simulations. The SCENIC LCFS matches the EFIT solution as close as possible while maintaining the up-down symmetry. Moreover the MHD equilibrium reconstruction with ANIMEC may bring some difficulties if one wants to use the exact same profiles as given by EFIT, depending on whether the rotational transform or the toroidal current density profile is used. In JET experiments, the latter can be estimated with reasonable accuracy via Motional Stark Effect spectroscopy diagnostic. However this diagnostic was not available for the pulses investigated here and consequently only an estimation of the safety factor profile is available. ANIMEC can of course compute the MHD equilibrium corresponding to an input q profile, but the SCENIC iterative procedure requires inclusion of the fast ion contribution in order to update the MHD state with the fast ions contributions. It does not seem feasible to compute directly the effect of the minority ion distribution function on the safety factor. On the other hand, a direct output of the VENUS-LEVIS code is the correction to the toroidal current density which corresponds to the following moment of the

minority ion distribution function:

$$\boldsymbol{j}_h = \int Z_h q v^{\varphi} f(\boldsymbol{x}, \boldsymbol{v}) \mathrm{d}\boldsymbol{v} \tag{3.17}$$

It is therefore more convenient to use the background toroidal current density as an input for the equilibrium calculation and to correct it by this moment at each iteration. Another advantage of using the toroidal current density over the q profile is the possibility to account for the drag effect from the background electrons and ions on the fast ion generated current. Indeed, and as discussed in Refs. [65, 66], the background electrons and ions respond to the collisions with fast ions by the generation of current densities. In that case, a drag current must be subtracted from the fast ion current obtained with eq. 3.17. An estimation of the resulting fast ion current can be found in Refs. [65, 66] and reads:

$$\boldsymbol{j}_{drag} = \boldsymbol{j}_h \left(1 - \frac{Z_h}{Z_{eff}} - \frac{m_h \sum_i Z_i n_i (1 - \frac{Z_i}{Z_{eff}})}{Z_h \sum_i n_i m_i} + 1.46\sqrt{\frac{r}{R_0}} A(Z_{eff}) \left(\frac{Z_h}{Z_{eff}} - \frac{m_h \sum_i n_i Z_i^2}{Z_h Z_{eff} \sum_i n_i m_i} \right) \right) \tag{3.18}$$

In eq. 3.18, the index h refers to the fast ion species, and index i designates the background ion species (i.e. main ionic species and impurities, etc). The corresponding EFIT calculation for the q profile, shown in Fig. 3.4b, increases rapidly towards the separatrix. The `ANIMEC` code has to be first run with this q profile in order to compute the corresponding toroidal current density which is displayed in Fig. 3.4c (dotted line).

(a) Shape of the last closed flux surface.

(b) Safety factor.

(c) Toroidal current density.
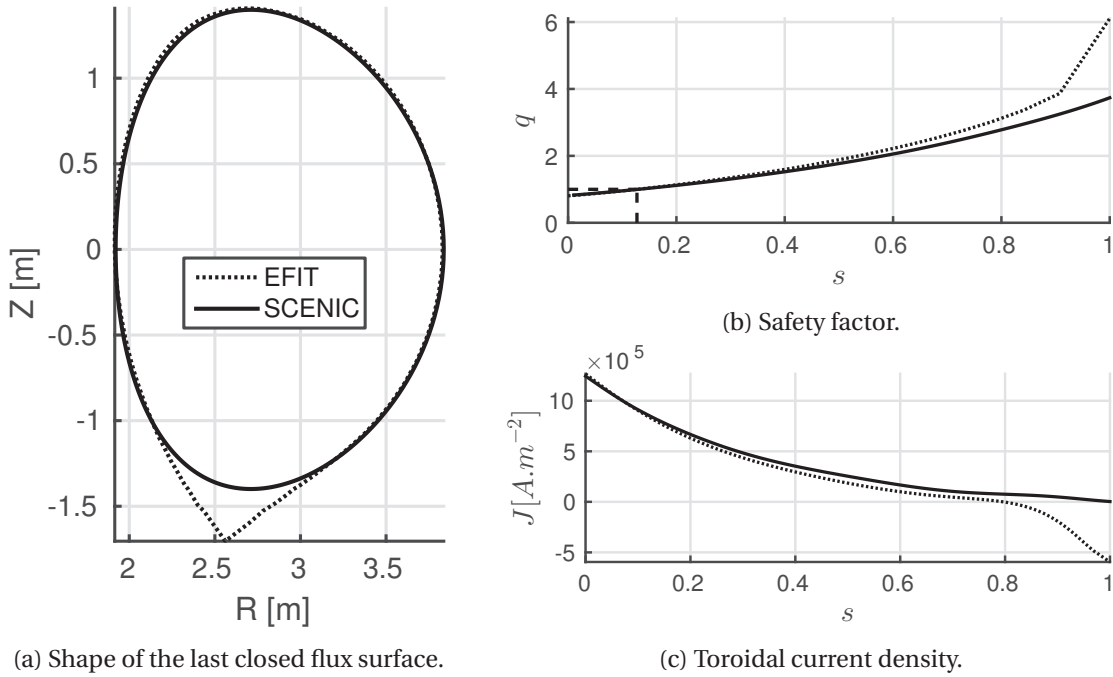
Figure 3.4: Comparison of the main equilibrium data given by EFIT and used for the SCENIC simulations. The current density plotted with a dotted line in (c) was obtained by ANIMEC calculations based on the EFIT q profile.

It is seen that this toroidal current density profile takes negative values throughout a significant portion of the plasma volume. This change of sign may be due to the constraint imposed on the LCFS for the equilibrium calculation. It is assumed in the modelling reported here that this change in sign is not physical and the toroidal current density in this region is artificially reshaped so that it remains positive in the confined volume and reaches 0 at $s = 1$. This fine-tuning of the current density is made under the constraint of keeping the q=1 surface approximatively at the same radial position as in the EFIT calculation. The resulting current density is displayed by the solid line in Fig. 3.4c. The ICRF wave frequency is set to 37.2 MHz such that the unshifted fundamental cyclotron resonance of Hydrogen ions is slightly located on the HFS of the $q = 1$ surface. This configuration is representative of the experiments in which in the resonance position was swept through the $q = 1$ surface. A different antenna setup relative to the one illustrated in section 3.1 has been used. The corresponding mode numbers that have been employed to represent the phasing configurations are given in table 3.1. Using the same mode number in absolute value between dipole and the asymmetric phasings ensures that the Doppler broadened resonance layer is comparable in all three cases. It was seen in Fig. 3.2, that a dipole phasing typically that the dominant on each side of the spectrum is about twice as much as the dominant mode of the $\pm 90°$ phasings. However, a dipole phased wave can be, theoretically at least, generated by the use of the two antennae: one set at $+90°$ and the other at $-90°$.

Phasing	-90°	+90°	Dipole
Mode number	+17	-17	+17,-17

Table 3.1: Mode numbers used for the following SCENIC simulations.

3.3 Self-consistent distribution functions

In this section the self-consistent distribution functions obtained by SCENIC simulations and the effect of antenna phasing are described. Figure 3.5 shows for each phasing the time evolution of the mean energy per particle which is defined as:

$$\langle E \rangle = \frac{1}{N} \int \frac{1}{2} m v^2 f(\boldsymbol{x}, \boldsymbol{v}) \mathrm{d}\boldsymbol{x} \mathrm{d}\boldsymbol{v} \tag{3.19}$$

where N is the total number of H ions:

$$N = \int f(\boldsymbol{x}, \boldsymbol{v}) \mathrm{d}\boldsymbol{x} \mathrm{d}\boldsymbol{v} \tag{3.20}$$

As described in [53], the saturation of this quantity in time is a measurement of the converged state of the minority ion distribution function. In this figure, the coloured squared illustrate the SCENIC iterative procedure: the markers time evolution is stopped, the fast component of the distribution is fitted on the bi-Maxwellian model, the corresponding moments are used by ANIMEC and LEMan to update the ideal MHD equilibrium and the fast wave propagation properties. The time during which the markers are evolved between each iteration is taken in this case as 2/3 of the slowing down time on electrons. This characteristic time appears as a convenient time scale for simulation of fast ions since it is almost constant for ions up to few MeV and it is also the shortest Coulomb interaction time with the background species. It is seen in Fig. 3.5 that around 10 to 12 iterations are required for good convergence of the minority distribution function. The self-consistent solutions are obtained in the present calculations after 5 simulated slowing down time. Let us point out that shorter iterations may lead to the self-consistent solution after a smaller simulated time t/τ_{se} and this does not correspond to the physical taken for the establishment the ICRF heated ion distribution. More physical quantities can be extracted from the simulated markers distribution. The physical energy distribution is obtained by integrating the numerical markers distribution over configuration space and pitch-angle so that:

$$\sqrt{E} f(E) \mathrm{d}E = \int_s \int_\theta \int_\varphi \int_\lambda f(s, \theta, \varphi, E, \lambda) \sqrt{g} \mathrm{d}s \mathrm{d}\theta \mathrm{d}\varphi \sqrt{g}_v \mathrm{d}\lambda \mathrm{d}E \tag{3.21}$$

where $\sqrt{g}$ and $\sqrt{g}_v$ are respectively the configuration and velocity space jacobian. Numerically, this function is obtained by binning the energy domain and summing the weight contribution w_j of each marker. An energy bin $\mathscr{E}$ is defined by an energy grid point E_i and a width $\mathrm{d}E$:
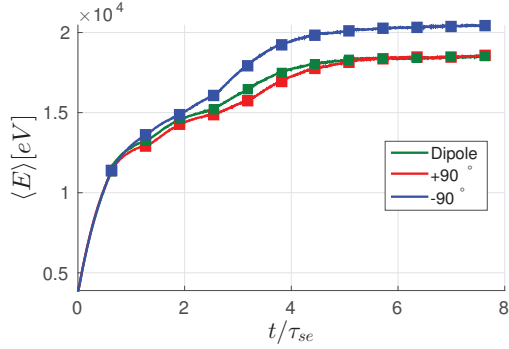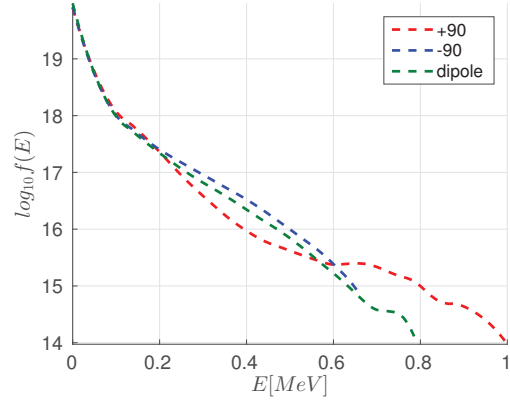
Figure 3.5: Mean energy per H ions with respect to time.

Figure 3.6: Energy distribution functions of H ions.

$$\mathscr{E} = [E_i - \frac{dE}{2}, E_i + \frac{dE}{2}]$$

$$\sqrt{E_i} f(E_i) \mathrm{d}E = \sum_{j; E_j \in \mathscr{E}} w_j \tag{3.22}$$

Denoting N the number of modelled physical particles, the markers numerical weight is normalised so that:

$$\int_0^\infty \sqrt{E} f(E) \mathrm{d}E = N \tag{3.23}$$

Fig. 3.6 shows the tail energy distribution functions obtained for the three phasing cases. It is seen that a longer fast ion tail is generated with the +90° phased wave: the distribution function contains a non-negligible fraction of ions above 600 keV and up to 1 MeV. However, a the -90° phasing case shows a larger fraction of ions within 200 keV − 600 keV. This explains the ordering of the curves of the mean energy per particle in Fig. 3.5. However, the consequence of the employed phasing on the mean energy reached by the fast ions is not necessarily easy to predict because other parameters in particular the resonance position and the thermal profile complicates the picture.

3.4 RF induced particle pinch

As presented in section 3.1, the phase shift between the current densities flowing in the antenna straps can be used to produce a wave that propagates toroidally in the co- (+90°) or counter-current direction (−90°). It was shown in Ref. [58] that toroidally propagating ICRF waves induce a net radial drift of resonant particles which can be summarised as follows. The RF wave-particle interaction causes a change in the magnetic moment (equivalently $v_\perp$) of resonant particles such that on average these particles become trapped and their bounce tips align with the resonant layer. To understand the RF-pinch mechanism, let us consider a resonant trapped particle being reflected at the resonance position. The bounce

tip position, i.e. where the parallel velocity vanishes, can be expressed as a function of the toroidal momentum P_φ:

$$|\psi_b| = -\psi_b = \frac{P_\varphi}{q}. \tag{3.24}$$

As previously mentionned, one can approximate the problem by considering only the dominant mode number in order to calculate the effect of the wave on the particle distribution function. The wave's electric field takes the simple form: $\boldsymbol{E} = \tilde{\boldsymbol{E}} e^{i(n_\varphi \varphi - \omega t)}$. Following Ref. [58] the change in the toroidal momentum δP_φ after each wave-particle interaction can be related to the change in energy δE:

$$\delta P_\varphi = \frac{n_\varphi}{\omega} \delta E \simeq \frac{k_\parallel R_{ant}}{\omega} \delta E. \tag{3.25}$$

In Eq. 3.25, ω is the RF wave frequency. After many interactions, the change in the toroidal momentum subsequently results, on average, in a radial displacement of the trapped particles bounce tips along the resonant layer. It is seen from eq. 3.24 and 3.25 that co-current (resp. counter-counter) travelling waves for which $k_\parallel < 0$ ($k_\parallel > 0$) cause an inward (outward) radial displacement of the trapped particles bounce tips. Note that we considered a trapped particle for the sake of this description, but the toroidal momentum of passing resonant particles are also affected by interaction with the wave, and therefore also experience the pinch effect. An indication of the RF-pinch phenomenon is seen from pressure distribution along the vertical direction (and integrated along the radial direction) in Fig. 3.7 which shows that in the $+90°$ case, the pressure profile is more peaked towards the mid-plane. Moreover, $-90°$ phased wave produces a broader profile than the other phasings. In addition, since dipole phasing employs both a co- and a counter-travelling waves, both effects are present and the corresponding moments show a mixture of these two ambivalent effects. These features are also retrieved on Fig. 3.8 which show the flux surface averaged fast ion pressures.
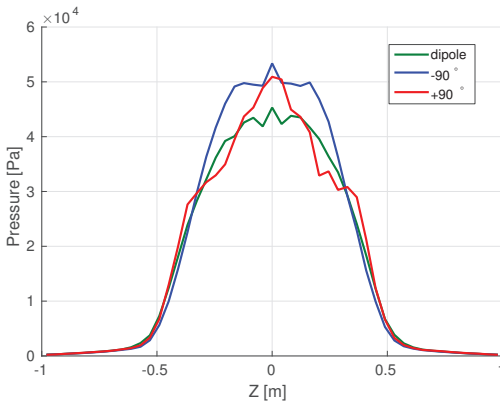
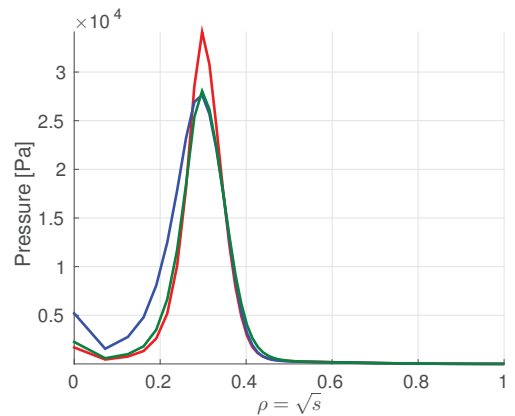Figure 3.7: Fast ion pressure along the vertical direction.

Figure 3.8: Flux surface averaged fast ion pressure.

The resonant particles type of orbit can be strongly affected depending on the employed phasing. In particular, as a co-current travelling wave will push the bounce tips closer to each other, it is expected that the orbit of some trapped resonant particles will convert into passing orbits. On the contrary, the resonant trapped particle bounce tips are moved radially outward under the influence of a counter-current travelling wave, which may cause the outer leg of banana orbits to intersect the wall, leading to fast particle losses. It is expected that these effects may be more or less pronounced depending on the resonance position but also the energy transmitted to the resonant particles which typically depends on the minority concentration and the RF input power. This will be discussed and illustrated in more detail in Chapter 4.6 in which the Three-Ion species scheme, involving resonant species at very low concentrations (0.1%), is discussed.

3.5 Sawtooth control

Plasma core MHD instabilities can cause severe degradation of the magnetic confinement of tokamak plasmas. This is the case of the internal kink mode which is located at $q = 1$ surface. It can be shown that the plasma resistivity is then responsible for the diffusion of the magnetic flux beyond the $q = 1$ surface which is associated with magnetic lines reconnection and redistribution of the plasma contained within the $q = 1$ surface through a larger plasma volume. This redistribution occurs on very short time scale. Even though models have been established (e.g. [67, 68]), the exact dynamics of the sawtooth crash remain unclear. However the consequences of this event are well known and was first reported in Ref. [69]. In particular, the thermal and the safety factor profiles are strongly affected. Some experimental observations show that after the sawtooth crash the safety factor is above unity throughout the whole plasma volume, and temperature and density profile are flattened in the core region. These sudden changes are followed by a relaxation phase which tends to restore the equilibrium profiles and in particular the $q = 1$ surface. Favourable conditions for the driving of the internal kink mode are met again and the periodic phenomenon of sawtooth cycles is observed. The length of the sawtooth period is of concern because long sawteeth are known [70, 71] to often end in triggering of large Neoclassing Tearing Modes and eventually plasma disruption. In ITER, these events are predicted to be very large and have to be avoided because ITER is designed to tolerate only a few large disruptions throughout its lifetime. It was pointed out in Ref. [72] that possible sources of stabilisation or de-stabilisation of the internal kink mode, i.e. lengthening or shortening of the sawtooth period, involve energetic ion populations. It is expected that trapped fusion born alpha particles will have a stabilising effect in ITER and future fusion reactors. Auxiliary control methods for destabilising the internal kink mode and avoiding the deleterious consequences of large sawtooth crashes in these machines are then required. Experiments showed that a possible method is to use ICRF waves in order to generate a fast ion population which shortens the sawtooth period. To understand the role of fast ions on the internal kink mode and sawteeth, one can write in the

ideal limit [73] the growth rate of the internal kink mode γ_I, which defines its stability:

$$\gamma_I/\omega_A = -\pi\delta\hat{W}/s_1, \tag{3.26}$$

where ω_A is the Alfvén frequency and s_1 the magnetic shear at the $q = 1$ surface. $\delta\hat{W}$ is the normalised energy functional associated with the internal kink mode. An early interpretation for the experimental observations was given in Ref. [74]. According to this model, the onset of the sawtooth instability requires an increase of the magnetic shear at the $q = 1$ such that:

$$s_c < s_1, \tag{3.27}$$

where s_c is a critical shear value proportional to $\delta\hat{W}$. SCENIC allows the calculation of the shear profile affected by the fast ion driven current. Such calculations take into account the drag current in eq. 3.18 and are displayed in Fig. 3.9. It is seen, regardless of the employed antenna phasing, that the shear value at the $q = 1$ surface is in fact decreased. In that case the shear mechanism predicts a stabilisation of the internal kink mode. However this is in contradiction with the experimental results reported in [75] which are the basis of the modelling presented in this chapter. Indeed it was observed that the sawtooth period was efficiently shortened and their amplitude decreased with all three phasings. Therefore the mecanism of Eq. 3.27 cannot be invoked here to explain the observed change in the sawtooth activity.

(a) Fast current density.
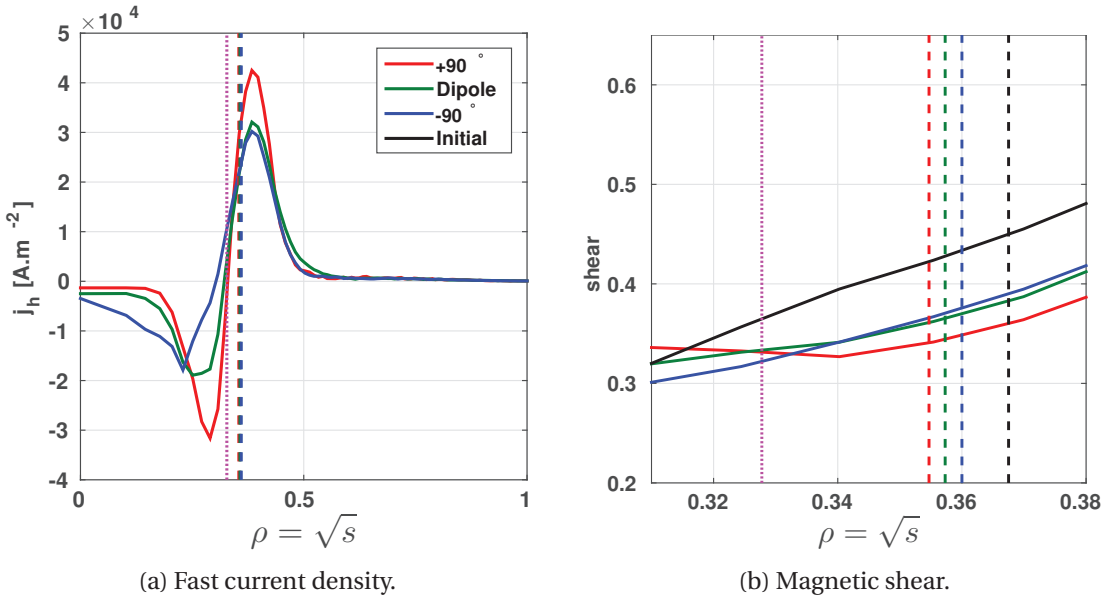
(b) Magnetic shear.

Figure 3.9: ICRF induced fast ion current profiles and the corresponding magnetic shear near the resonance layer. The dotted line refers to the resonance position mapped onto the outer midplane. The dashed lines show the position of the q=1 surface with and without the effect of the fast ion current.

Using a hybrid kinetic-MHD model, it can be shown [73, 75, 76] that a passing particle popula-

tion displaying strong asymmetry in velocity space brings a significant negative contribution to $\delta\hat{W}$ in eq. 3.26. In this framework the fast ions contribution to $\delta\hat{W}$ is:

$$\delta W_h = -\frac{1}{2}\int d^3x\boldsymbol{\xi}^* \cdot \left(-\nabla \cdot \overline{\overline{\delta P_h}}\right) \tag{3.28}$$

where $\boldsymbol{\xi}$ is the plasma displacement and $\overline{\overline{\delta P_h}}$ is the pressure tensor derived from the fast ion distribution function. It is shown in Ref. [73] that δW_h becomes strongly negative if the fast ion distribution displays a particular asymmetry in velocity space. The condition can be associated with a gradient in the fast passing ion current J_h. Indeed, it can be shown that when the resonance position approaches the $q = 1$ surface:

$$\delta W_h \propto -\frac{d}{dr}J_h \tag{3.29}$$

The fast passing ion current profile computed by SCENIC for the dipole phasing case is seen (see Fig. 3.10a) to possess such a favourable gradient for destabilisation. The outboard midplane velocity distributions at, and on both sides of the resonance position (also shown in Fig. 3.10) display strong asymmetry in particular in the passing region of phase-space.
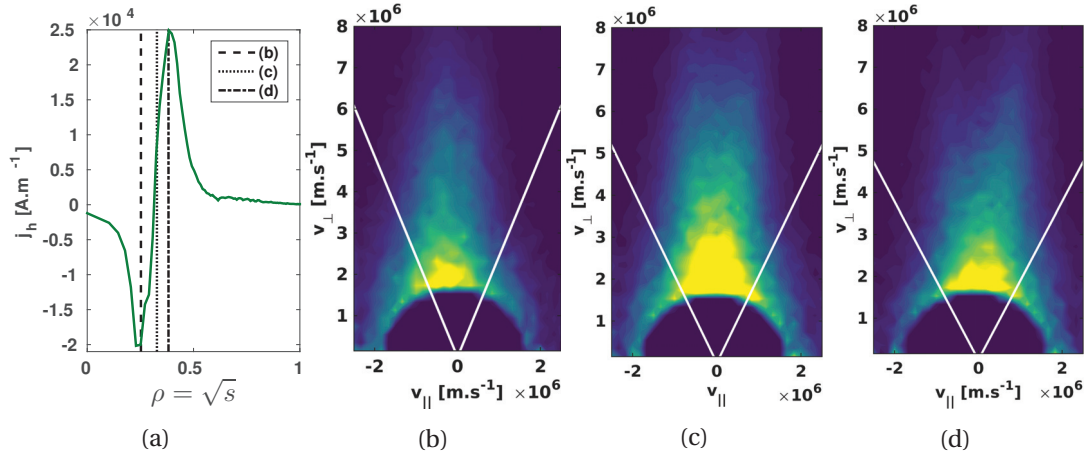
Figure 3.10: Current generated by the fast passing ions for the dipole phasing case. The positions for the computation of the contours of the distribution function are shown in (a). The straight white lines in the contour plot show the local trapped-passing boundary.

The destabilising contribution from the ICRF fast ions can be confirmed by appropriate stability calculations. The ICRF distribution obtained with SCENIC and the NBI distribution from TRANSP [77] for the +90° phasing case was passed to the stability code HAGIS [78] which computes the corresponding δW_h. Fig. 3.11 shows how δW_h varies as the resonance position is displaced with respect to the $q = 1$ surface. The MHD contribution was calculated with the MISHKA code [79]. It is seen that the ICRF fast (computed by SCENIC) bring a large destabilising contribution to the internal kink and is even stronger than the stabilisation from NBI ions around the resonance position. The ICRF distribution obtained with the SELFO code was also

used by HAGIS and displays also a strong destabilising component to the internal kink mode, and a useful benchmark between SCENIC and SELFO. Considering the current state of the known physics at stake here, these calculations indicate that the fast ion mechanism is a valid explanation for the experimental observations.
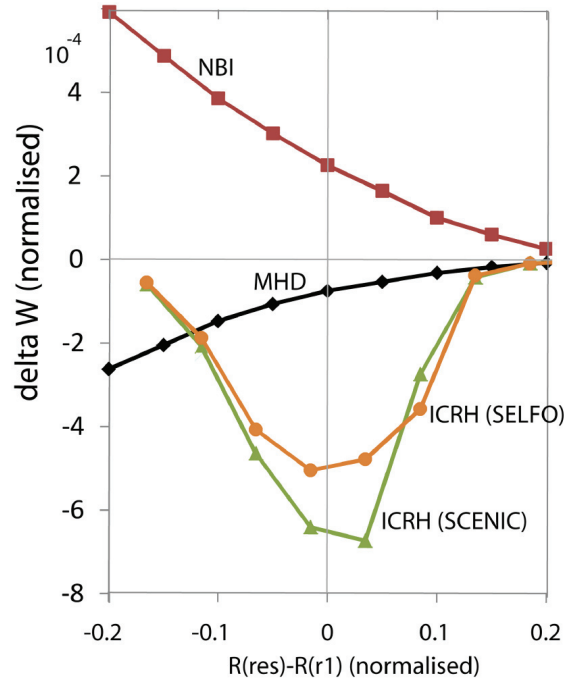

Figure 3.11: The contributions from the NBI ions, the ideal MHD and the ICRF fast ions to the internal kink mode stability as a function of the relative radial distance between the resonance and the $q = 1$ surface.

3.6 Summary

In this chapter the SCENIC package was applied to a JET axisymmetric tokamak case for the interpretation of experimental sawtooth control results. The modelling of the ICRF antenna in the SCENIC framework has been described and the crucial notion of antenna phasing, or equivalently the wave direction of propagation, for ICRF heating scenarios has been introduced. It was also seen that the physical dimension of the antenna (e.g. strap width and spacing, plasma-antenna distance) must be accounted for in ICRF modelling task because it determines the toroidal mode spectrum to consider. In the SCENIC simulations, only the dominant modes are taken into account in the wave calculation. It is important to mention that the selected toroidal mode for the wave calculation dictates the value of the parallel wave number $k_{\parallel}$, consequently influencing the width of the Doppler shifted resonance position given by the resonance condition $\omega_{ant} - k_{\parallel} v_{\parallel} - \Omega_c = 0$.

The JET plasma pulse #84497 was the basis of the simulations presented in this chapter. The

experimental data, in particular the safety factor profile and the shape of the LCFS, had to be adjusted in order to be used in the framework of SCENIC . It might be possible [80] to adapt the formulation of the wave solver LEMan to benefit from the advantages of the Boozer coordinate system regarding the wave equation while including more shaping effects (i.e. breaking the stellarator symmetry) in the equilibrium calculation. However, this rather challenging task, in particular from the numerical point of view, remains to be explored.

The self-consistent distribution functions with $-90°$, $+90°$ and dipole phasings were computed. A detailed analysis shows that a larger fast ion population is generated with the $-90°$. However, the RF-pinch effect which pushes the bounce tips of resonant trapped particles respectively inward (outward) for $+90°$ $(-90°)$. The radial profiles of velocity moments are more peaked and higher in amplitude at the resonance position when a $+90°$ phased wave is used. There does not seem to be a precise scaling for the prediction of the actual range energy to be reached by the fast ions with respect to the employed wave phasing. This question is worth investigating further. In particular, the resonance position and the shape of the thermal profile is expected to influence the wave electric field profile and also the Coulomb collision processes which in turn partly dictate the fast tail formation.

Finally, ICRF fast ion simulations performed with SCENIC show that the shear mechanism of Ref. [74] predicts stabilisation of the internal kink mode by fast ions in contradiction with the sawtooth control experimental observations. The coupling of these simulations with the stability code HAGIS showed that the asymmetry in the velocity distribution can explain the observed shortening of the sawteeth period. ICRF minority heating is therefore an efficient tool for controlling the sawtooth activity. Given some flexibility of the ICRF system apparatus in current and future tokamaks the destabilising contribution of the generated fast ions can be deposited on the $q = 1$ surface causing shorter and smaller sawtooth crashes and consequently avoiding the triggering of confinement degrading Neoclassical Tearing Modes. It should be noted that fast ion orbit widths, and the RF pinch effect, are crucial ingredients for this mechanism, making SCENIC the perfect tool for quantifying the effect.

4 Three-Dimensional configurations: Particle confinement and heating in the Wendelstein 7-X stellarator

In this chapter, the `SCENIC` package is used to study the confinement and the generation of fast ions in the Wendelstein 7-X stellarator. In section 4.1, we shortly review the stellarator concept and the various stellarator magnetic configurations that have been studied and built since the seminal work from L. Spitzer in the 1950s. The W7-X equilibrium configurations that were used in this thesis are presented in section 4.2. In addition, the concept of quasi-isodynamicity is discussed with mathematical considerations in order to better understand the confinement of collisionless particles in W7-X. In section 4.3, the mechanisms causing the losses of such particles are introduced. `VENUS–LEVIS` simulations of an NBI-like population are presented in section 4.4 and illustrates the loss channel previously described. In section 4.5, the possibility to generate a fast ion population in W7-X with an ICRF minority heating scenario is investigated. The particle losses under ICRF conditions are carefully studied.

4.1 Stellarator overview

The tokamak has been for a long time the most promising configuration for magnetic confinement fusion reactors. The construction of these machines are somewhat simplified by their inherent toroidal symmetry. As already mentioned in section 2.1.4, this symmetry also offers good collisionless particle confinement. However the confining helical magnetic field can exist in tokamaks only if a high current is circulating in the plasma. This current is in turn a source of large MHD instabilities and in case of rapid loss of confinement is the cause of deleterious disruption events. In his very famous paper published in 1958 [81], L. Spitzer exposed the stellarator concept which consists of generating the poloidal magnetic field component, and therefore a rotational transform, without the circulation of toroidal plasma current. The main advantages of this design compared to the tokamak is the intrinsic possibility of steady-state operation and the absence of most of confinement degrading MHD instabilities. The first machines built under the Matterhorn Project led by Spitzer in Princeton had the shape of a figure-8 and only used toroidal coils to generated the confining magnetic field. These machines inspired the construction of other stellarators outside the U.S., in particular in Germany and Japan. Various coil configurations were investigated. The twist of the magnetic field line

is generated in part by the use of continuous helical coils in heliotrons (Japan) and other classical stellarators of the Wendelstein series (Germany). A set of toroidal and poloidal coils can be arranged as shown in Ref. [82] in order to create the Heliac configuration on which the TJ-II stellarator in Spain is built.

It is seen that the magnetic configuration in all these devices leads to low machine performance and in particular a rather poor confinement of collisionless trapped particles. The high level neoclassical transport at low collisionality is caused by to the lack of symmetry in the equilibrium. It was shown in Ref. [83] that there exists, at least mathematically, a class of magnetic configurations in which all trapped particles are confined. In these so-called "omnigenous" configurations, the net radial drift of trapped particles would essentially be non-existing. The amplitude of a perfectly omnigenous magnetic field would only depend on the radial flux variable $B = B(\psi)$. However it was shown in Ref. [84] that such configurations do not exist in toroidal devices with closed magnetic surfaces and with a non-vanishing magnetic field on axis. Omnigenity therefore appears as a very constraining condition but there is another way to design stellarator fields with good confinement properties. It is formally shown in Ref. [85] that there exists a subset of omnigenous fields which is of particular interest for stellarators. These fields must display a certain symmetry that the three-dimensional configuration does not seem to allow at first glance. Such fields are usually mathematically constructed by the use of coordinate systems in which the field lines appear straight on flux surfaces and the guiding centre equations of motion only depend on the amplitude of the magnetic amplitude (and not on its direction). The Boozer coordinate system (s, θ, φ) mentioned in section 2.3.2 meets these criteria and is typically used for studying stellarator magnetic fields. In such a coordinate system, a magnetic field is omnigenous if it contains a symmetry of the type:

$$B = B(s, M\theta - N\varphi), \tag{4.1}$$

where, M and N are integers. This equation means that the magnetic field amplitude depends essentially on the radial variable and a helical angle $\chi = M\theta - N\varphi$. Therefore there is an ignorable variable which would ensure the confinement of trapped particles, similarly to axisymmetric tokamak field for which the cylindrical angle (toroidal angle of symmetry) is ignorable. This exact type of symmetry is however not possible to achieve in realistic machines. Therefore we usually refer instead to "quasi-symmetric" stellarators. Here, the prefix "quasi" has a dual meaning in the sense that (1) the symmetry of the field is in a way hidden in the Boozer representation while full three-dimensionality still appears in Cartesian representation, and that (2) the symmetry cannot be realised in the entire plasma volume [86]. The type of symmetry that one attempts to approach can be classified by the choice of the integers M and N in eq. 4.1. If $M = 0$, the magnetic field is quasi-poloidally symmetric and the spectrum of the Fourier decomposition given in eq. 2.46a is typically dominated by the components $B_{0,0}$, $B_{0,1}$, $B_{0,2}$. Since the non-poloidally symmetric components, e.g. $B_{1,1}$, are usually small but non vanishing, one understands the "quasi"-poloidally symmetric designation. The Quasi-Poloidal Stellarator (QPS) [87] which was designed at the University of Tennessee and the Oak Ridge National Laboratory was based on this concept. Similarly, quasi-axisymmetric

fields are obtained when one aims at approaching the configuration $N = 0$. The National Compact Stellarator eXperiment (NCSX) that was intended to be built in Princeton, was based on this configuration but its construction was halted in 2008. The Evolutive STELlarator of Lorraine (ESTELL) [88, 89], currently under design in France, is also based on the quasi-axisymmetric configuration. The Helically Symmetric eXperiment (HSX) [90], in operation in Madison, is a quasi-helically symmetric stellarator ($M = 1$, $N = 1$). This configuration was introduced in Ref. [91]. As already mentioned, perfectly quasi-symmetric field (in the sense of eq. 4.1) can not be achieved and small deviations from the symmetry can lead to substantial fast particle confinement degradation. Therefore it is preferential to relax the quasi-symmetric constraint and to optimise a reactor relevant stellarator field following precise criteria which are enumerated in Ref. [92]. The Helias configuration and subsequently the design of the Wendelstein 7-X (W7X) stellarator was obtained by such an optimisation procedure. A description of a typical W7-X equilibrium will be shown later in section 4.2.1 and it will be seen mathematically that W7-X is quasi-omnigenous, because the net radial drift of most of trapped particles can be shown to be vanishing in the vicinity of the magnetic axis. In addition, since these particles drift poloidally, as seen earlier in Fig. 2.8, W7-X belongs to the so-called quasi-isodynamic class of stellarators. Following the optimisation calculations described in Ref. [92], the quasi-isodynamic Helias configuration is therefore designed to display reactor relevant features such as steady-state operation, good fast particle confinement, good MHD stability and small bootstrap current. Extrapolations of the W7-X configuration are foreseen as a good candidates for stellarator fusion reactors [93].

4.2 The Wendelstein 7-X stellarator

4.2.1 Adiabatic invariant and quasi-isodynamicity

Due to the inherent problems of designing stellarator fields with quasi-symmetry, the quasi-isodynamic approach gives up on trying to find an ignorable (symmetric) helical angle, but instead optimises confinement over many bounce times. As will be seen in this section, cross field radial motion is cyclical, providing contours of the longitudinal invariant $\mathcal{J}$ are closed over a poloidal cross section. In stellarators, the confinement of energetic trapped particles is of special concern because their radial drift may cause them to escape the last closed flux surface (LCFS) before de-trapping occurs. For thermal particles the collision frequency would be sufficiently high to de-trap particles and change their orbit topology to a confined passing orbit. However assuming the typical collision time of fast particles like alphas in a reactor is long compared to their confinement time, their confinement mainly relies on minimising the radial drift averaged over many bounces. The drift optimisation is based on the calculation of the longitudinal adiabatic invariant, often, lowest order $\mathcal{J}_0$. This quantity is a function of phase space and one way to represent it is to consider the radial and poloidal locations

(ψ_b, θ_b) of the bounce or transit points for fixed E and B_{ref}:

$$\mathscr{I}(\psi_b, \theta_b, E, B_{ref}) = \oint v_\| \, \mathrm{d}l. \tag{4.2}$$

where the integral path is taken along a particles complete bounce(trapped) or transit(passing) trajectory. This quantity can also be expressed in the magnetic coordinate system (ψ, θ, φ) using an adiabatic expansion:

$$\mathscr{I}(\psi_b, \theta_b, E, B_{ref}) \simeq \mathscr{I}_0(\psi_b, \theta_b, E, B_{ref}) \tag{4.3}$$

As discussed in Ref [22], the lowest order in the guiding center approximation appropriate for $\mathscr{I}_0$, the element $\mathrm{d}l$ is calculated along the field line path. In an action-angle variable formalism, $\mathscr{I}_0$ contains information such as the bounce or transit time, but also the radial and poloidal deviation of the bounce or transit points from the field line. The bounce or transit time is simply:

$$T = \frac{\partial \mathscr{I}_0}{\partial E}. \tag{4.4}$$

The change in the variable ψ and θ after a complete bounce or a transit are then respectively:

$$\Delta\psi = \oint_{bounce} \mathrm{d}\varphi \frac{\mathrm{d}\psi}{\mathrm{d}\varphi} = \frac{\partial \mathscr{I}_0}{\partial \theta}, \tag{4.5}$$

$$\Delta\theta = \oint_{bounce} \mathrm{d}\varphi \frac{\mathrm{d}\theta}{\mathrm{d}\varphi} = -\frac{\partial \mathscr{I}_0}{\partial \psi}. \tag{4.6}$$

The radial and poloidal drift velocity over one bounce period is thus:

$$\langle \dot{\psi} \rangle_b = \frac{\Delta\psi}{T} = -\frac{\frac{\partial \mathscr{I}_0}{\partial \theta}}{\frac{\partial \mathscr{I}_0}{\partial E}}, \tag{4.7}$$

$$\langle \dot{\theta} \rangle_b = \frac{\Delta\theta}{T} = -\frac{\frac{\partial \mathscr{I}_0}{\partial \psi}}{\frac{\partial \mathscr{I}_0}{\partial E}}. \tag{4.8}$$

In an optimised stellarator such as W7-X, the longitudinal adiabatic invariant is almost a flux surface quantity for most of the trapped particles: $\frac{\partial \mathscr{I}_0}{\partial \theta} \simeq 0$. Therefore the radial drift along the bounce averaged motion of trapped particles vanishes to lowest order. In this approximation these particles mostly drift poloidally and remain confined on time scales larger that the typical slowing down time. There will nevertheless usually be some net radial excursion over one bounce time for fields that are not quasi-symmetric. Nevertheless, if $\partial\mathscr{I}_0/\partial\theta$ can itself be periodic, such that a particle undergoes periodic drift motion (without in that time leaving the plasma), the particle will be confined. All that is required is that a particle, over many bounces, executes an orbit such that $\mathscr{I}_0$ is closed in the poloidal plane.

In W7-X, drift optimised magnetic configurations are ensured by high thermal pressure. The expression for $\mathcal{J}_0$ for trapped particles is:

$$
\begin{aligned}
\mathcal{J}_0 &= \oint_{bounce} m v_\parallel \mathrm{d} l_f \\
&= \sqrt{2mE} \oint_{bounce} \sqrt{1 - \frac{B}{B_{ref}}} \mathrm{d} l_f.
\end{aligned}
\tag{4.9}
$$

Here $\mathrm{d} l_f$ is an infinitesimal field line element length which can be written from the field line equation:

$$
\frac{\mathrm{d} l_f}{B} = \frac{\mathrm{d}\varphi}{\boldsymbol{B} \cdot \nabla \varphi}.
\tag{4.10}
$$

As the toroidal magnetic flux is given by:

$$
\Phi_{tor}(\rho) = \int_{\rho'=0}^{\rho'=\rho} \int_{\theta=0}^{\theta=2\pi} \int_{\varphi=0}^{\varphi=2\pi} \sqrt{g}\, \boldsymbol{B} \cdot \nabla \varphi \mathrm{d}\rho' \mathrm{d}\theta \mathrm{d}\varphi,
\tag{4.11}
$$

in a straight field line flux coordinate system, the field line element length reads:

$$
\mathrm{d} l_f = \sqrt{g}\, B \frac{\mathrm{d}\varphi}{\Phi'_{tor}},
\tag{4.12}
$$

where, $\sqrt{g} = (\nabla s \times \nabla \theta \cdot \nabla \varphi)^{-1}$ is the coordinate system jacobian. It then follows:

$$
\begin{aligned}
\mathcal{J}_0 &= \sqrt{2mE} \oint_{bounce} \sqrt{1 - \frac{B}{B_{ref}}} \sqrt{g}\, B \frac{\mathrm{d}\varphi}{\Phi'_{tor}}
\tag{4.13} \\
&= 2\sqrt{2mE} \int_{\varphi_1}^{\varphi_2} \sqrt{1 - \frac{B}{B_{ref}}} \sqrt{g}\, B \frac{\mathrm{d}\varphi}{\Phi'_{tor}}.
\tag{4.14}
\end{aligned}
$$

where φ_1 and φ_2 are the toroidal position of the bounce points. From this expression it is possible to numerically evaluate the contours of $\mathcal{J}_0$ for different $\langle \beta \rangle$ as will be illustrated in the next section.

4.2.2 Magnetic configuration

W7-X has been optimised in part to confine energetic trapped particles over their slowing down time scale. Confinement has been designed to be best for a high $\langle \beta \rangle$ MHD equilibrium. The $\langle \beta \rangle$ limit for stability in W7-X is about 5% [24]. Therefore, operating at a high $\langle \beta \rangle$ value, i.e. around 4% would ensure both plasma stability and fast particle confinement. In such configurations, a given particle trapped in one of the five magnetic toroidal mirrors will mostly drift poloidally, the radial drift being low due to small geodesic curvature. The flexibility of the coil system on W7-X grants access to a broad range of magnetic equilibrium configurations, which are characterised by a mirror ratio value [94, 95] defined as :

$$mr = \frac{B_{\varphi=0} - B_{\varphi=\pi/5}}{B_{\varphi=0} + B_{\varphi=\pi/5}}. \tag{4.15}$$

Here we investigate the high-mirror magnetic configuration with mr=8.7%. The equilibrium used has been calculated using the fixed boundary version of the `ANIMEC` code [10, 11] having a volume-averaged β of 4%. Such a $\langle \beta \rangle$ value would be roughly consistent with a central density of $1.5 \times 10^{20} \, m^{-3}$ and a central temperature of 4keV as achieved in transport simulations for W7-X with ECRH input powers above 5MW (for an example with $\langle \beta \rangle = 4.5\%$ with 8MW ECRH, 140GHz O2-mode [96]). The density and temperature profiles used in this work are analytic estimations and are displayed in Fig.4.1.
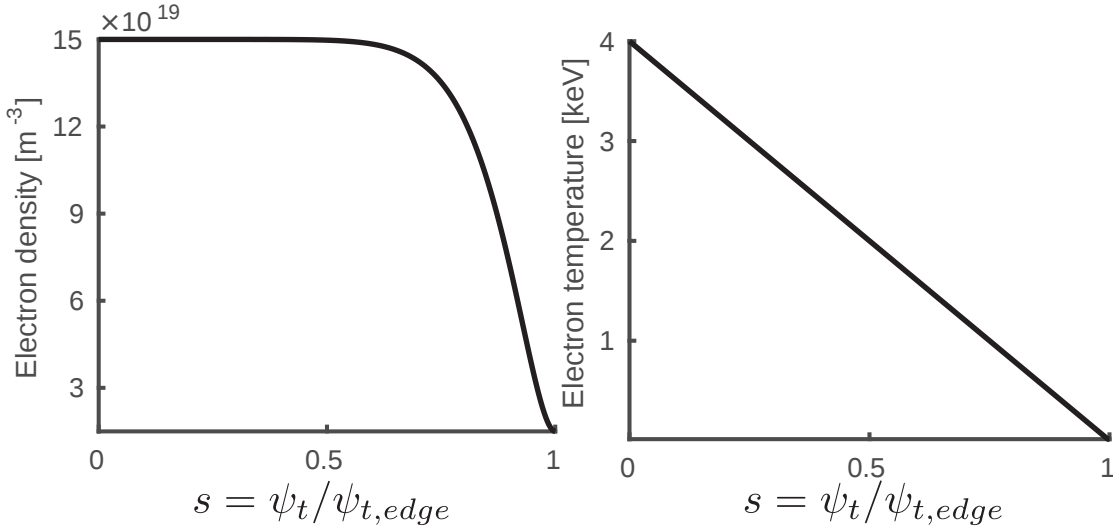
Figure 4.1: Density and temperature profiles used for the equilibrium reconstruction.

Poloidal cross sections of this equilibrium are displayed in Fig. 4.2 and show the toroidal variation of the equilibrium magnetic field amplitude. The `ANIMEC` code [10, 11] was used in order to reconstruct a high-mirror ($mr = 8.7\%$) and a standard ($mr = 4\%$) equilibrium. These configurations were chosen in order to emphasize the issues related to ICRF wave propagation

and absorption under particular toroidal variation of the equilibrium magnetic field. In particular, the amplitude of the toroidal gradient in the magnetic field amplitude can be such that the lowest $|B|$ value in the bean shaped cross section is higher than the highest $|B|$ value in the triangular cross section. Therefore, as seen in Fig. 4.2 for the high-mirror configuration, there is no particular $|B|$ value present at all toroidal positions. The consequence of this is that no ICRF wave frequency can be chosen such that a resonance will be found inside the plasma at all toroidal angles.
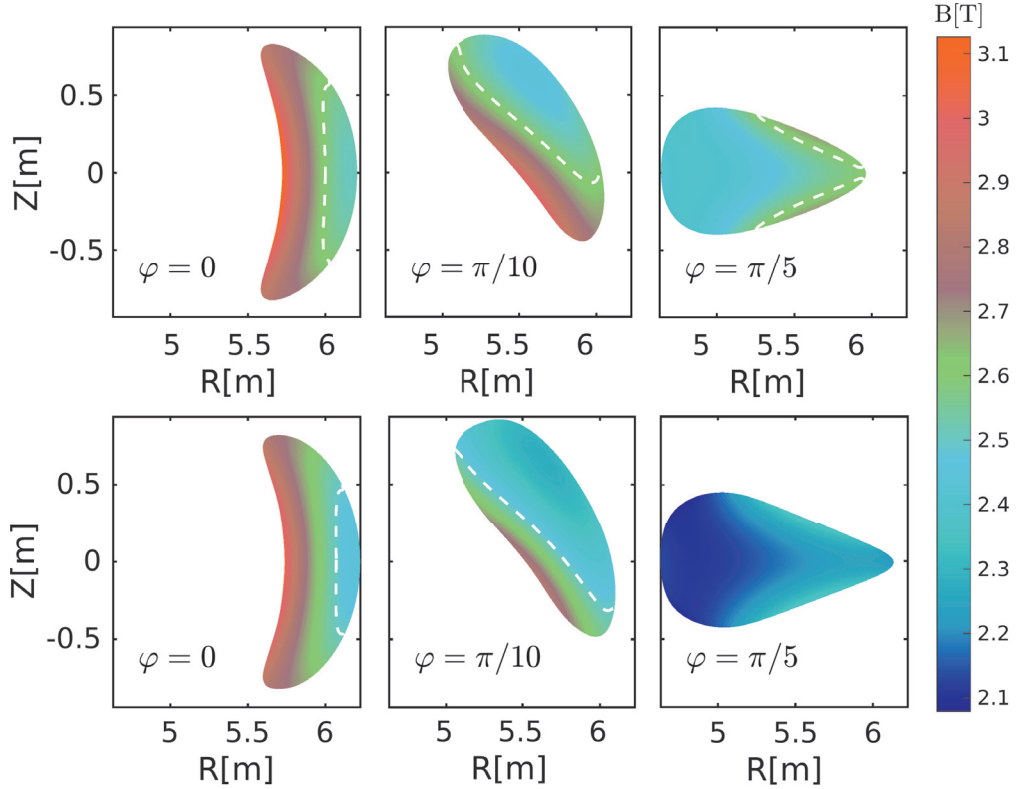
Figure 4.2: Poloidal cross sections of W7-X equilibria used (top: standard configuration, bottom: high-mirror configuration). Colours indicate the amplitude of the equilibrium magnetic field. Dashed white lines show the location of the iso-B surface corresponding to 2.6 T (top) and 2.5 T (bottom) respectively.

The high mirror configuration is considered to investigate the contours of $\mathcal{J}_0$ with a low and high $\langle \beta \rangle$ value and with $B_{ref} = 2.42$ T. Figure 4.3 shows the poloidal closure of $\mathcal{J}_0$ over most of the cross section for $\langle \beta \rangle = 4\%$ which leads to a reduction of trapped particle radial drifts. The contours for a $\langle \beta \rangle = 1\%$ is obtained by keeping the same pressure profile but reducing the central pressure. This low $\langle \beta \rangle$ case shows poor closure of $\mathcal{J}_0$. However it is impossible to ensure poloidal closure of $\mathcal{J}$ for all ranges of trapped particles, and over the entire plasma volume. As a consequence particle loss channels still exist and are described in the next section.
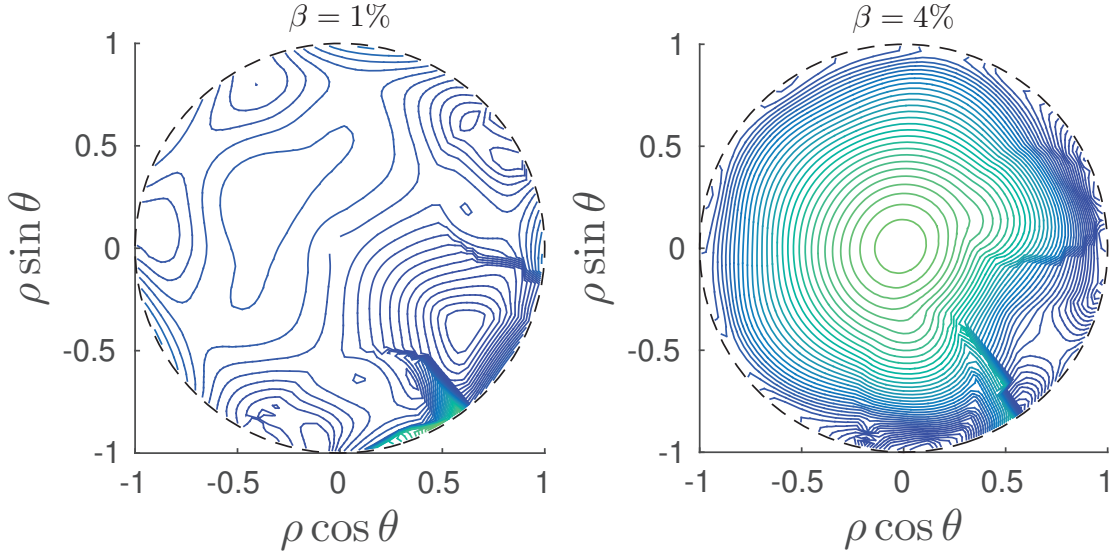
Figure 4.3: Contours of constant $\mathcal{J}_0$ for $B_{ref} = 2.42\,\text{T}$ and two values of $\langle \beta \rangle$.

4.3 Particle loss channels

Losses of alpha particles will be of primary concern for a future fusion reactor. Of most concern will be collsionless losses of particles still at or near their birth energy. Monte Carlo simulations of alpha particles in quasi-isodynamic and quasi-symmetric configurations were first presented in Ref. [97] and showed that the quasi-isodynamic design appears to be the best candidate for a reactor design. Additional efforts for understanding the collisionless dynamics of fast ions in quasi-isodynamic equilibria have been carried out. Losses induced by collisionless stochastic diffusion of fast ions was introduced in Ref. [97] and further developed in Ref. [23]. In addition, favourable conditions for unconfined collisionless orbits were discussed in Ref. [98]. The magnetic field curvature was shown to contribute significantly to the radial excursion of trapped particles. However, collisionality must also be considered in fast ion confinement studies since it is known to contribute to neoclassical transport of particles in general [99]. Recently, further numerical studies on fast ion confinement in W7-X configurations were presented in Ref. [95]. The latter work showed the effect of various magnetic equilibrium configurations on fast ions generated by neutral beam injection (NBI) at $\langle \beta \rangle = 2\%$. It was concluded that NBI may not be an efficient way to produce a fast particle population mostly because of rather poor beam penetration and rapid loss of injected particles. In this section, a description of the loss channels acting on a fast particle population is presented.

4.3.1 Stochastic diffusion losses

Stochastic diffusion of fast ions in optimised stellarators has been described in Ref. [23]. This diffusion process concerns transitioning particles, described in 2.1.3. The stochastic diffusion mechanism is as follows: a particle is able to change its orbit class (locally passing
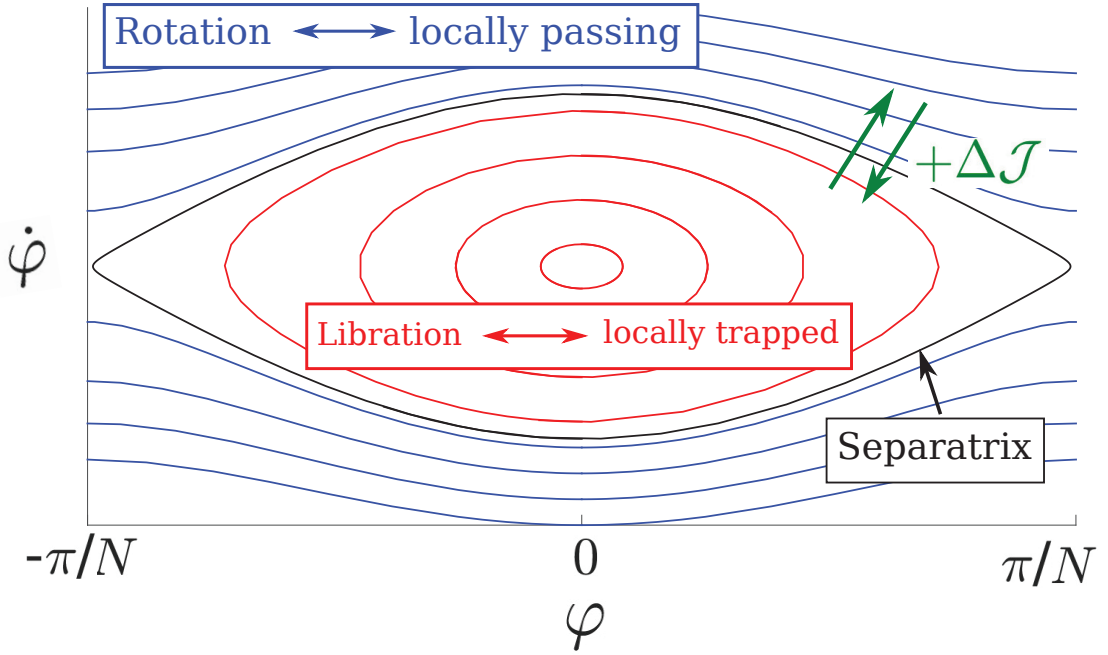
Figure 4.4: Phase portrait of locally passing/trapped particles in a given toroidal period of W7-X. Note that the features of a non-linear pendulum are retrieved.

to locally trapped or vice-versa) if it crosses the phase-space separatrix between libration (locally trapped) and rotation (locally passing) as illustrated by the schematic phase portrait in Fig. 4.4. This separatrix crossing implies a non adiabatic change in the particle motion [100]. However, an adiabatic treatment of the particle motion is still valid as long as the particle remains sufficiently far from the separatrix. In that case the particle motion can still be characterised by a longitudinal adiabatic invariant $\mathcal{J}$ for both the locally trapped and the locally passing motion. After multiple separatrix crossings, the adiabatic invariant associated with, for instance, the libration motion accumulates random jumps $\Delta\mathcal{J}$ which ultimately causes a stochastic diffusion in $\mathcal{J}$-space. In Ref [23] it was noted that each jump in $\mathcal{J}$ causes a radial displacement $\Delta\psi = \Delta\mathcal{J}\frac{\partial\psi}{\partial\mathcal{J}}$. This associated radial diffusion time is usually rather long compared to other loss mechanisms. Therefore it is expected that stochastic radial diffusion will act on initially well confined weakly collisional transitioning fast particles.

4.3.2 Drift induced losses

Inspection of eqs. (4.7) and (4.8) shows that reducing trapped particle losses can be achieved by ensuring that these particles avoid regions where $\langle\dot{\psi}\rangle_b$ is enhanced compared to $\langle\dot{\theta}\rangle_b$. The unfavourable regions can be identified in terms of equilibrium parameters. Considering no radial electric field and a static equilibrium field, the guiding centre of a particle of mass m

and charge q will drift perpendicularly to the magnetic field line with a drift velocity:

$$\boldsymbol{v_D} = \mathbf{b} \times \left(\frac{\mu}{q}\nabla B + v_\parallel \rho_\parallel B \boldsymbol{\kappa}\right)/B_\parallel^*. \tag{4.16}$$

Where $\rho_\parallel = mv_\parallel/qB$, $\boldsymbol{b} = \boldsymbol{B}/B$, $B_\parallel^* = \boldsymbol{b} \cdot \left(\boldsymbol{B} + \rho_\parallel \nabla \times \boldsymbol{B}\right)$ and $\boldsymbol{\kappa} = -\boldsymbol{b} \times (\nabla \times \boldsymbol{b}) = \boldsymbol{b} \cdot \nabla \boldsymbol{b}$ is the magnetic field line curvature. The latter can be used to relate the equilibrium configuration to the particle losses pattern. The field lines lie on curved magnetic flux surfaces, and in particular [14], the field line curvature is composed of a normal and a geodesic curvature. The field line curvature can be written :

$$\boldsymbol{\kappa} = \kappa_n \frac{\nabla s}{|\nabla s|} + \kappa_g \frac{\boldsymbol{B} \times \nabla s}{|\boldsymbol{B} \times \nabla s|}, \tag{4.17}$$

where $s = \Phi_{tor}/\Phi_{tor,edge}$ is a flux surface label and serves as radial coordinate in the magnetic coordinate system (s, θ, φ). From the definition of $\boldsymbol{\kappa}$ and assuming MHD force balance and nested flux surfaces, one can show that:

$$\boldsymbol{\kappa} = \frac{\nabla_\perp B}{B} + \mu_0 \frac{p'\nabla s}{B^2}, \tag{4.18}$$

with $p' = \frac{\mathrm{d}p}{\mathrm{d}s}$, so that the bounce averaged radial drift depends only on κ_g:

$$\oint_{bounce} \boldsymbol{v_D} \cdot \frac{\nabla s}{|\nabla s|} \mathrm{d}t = \oint_{bounce} -\left(\frac{\mu}{q} + v_\parallel \rho_\parallel\right) \frac{B}{B_\parallel^*} \kappa_g \mathrm{d}t, \tag{4.19}$$

$$\kappa_g = \frac{1}{\sqrt{g}\,B^2\sqrt{g^{ss}}} \left(\frac{\partial B}{\partial \theta}B_\varphi - \frac{\partial B}{\partial \varphi}B_\theta\right). \tag{4.20}$$

It appears clearly (as is well known) that particles with bounce trajectories mostly located in regions with negative geodesic curvature drift radially outwards and eventually escape the plasma if the geodesic curvature does not change sign over the particles trajectory before it reaches the edge. This reflects regions where $\mathscr{J}$ contours are not closed, i.e. geodesic curvature over the orbit does not complete a full period. Examples of such unconfined orbits are illustrated in Fig. 4.5. There are various types of "bad" curvature regions in W7-X. As seen in Fig. 4.5b, certain isosurfaces of B may exhibit narrow tubes with large radial extension and encapsulating a volume of negative curvature. In that case a trapped particle may fall into one of these tubes along its bounce trajectory and would quickly drift out of the plasma volume. Those tubes can be regarded as leaks in regions of phase space which mostly contain well confined particles. The avoidance of such tubes would mitigate this loss channel and might be worthwhile to be considered as an additional criterion in stellarator optimisation with respect to fast particle confinement.
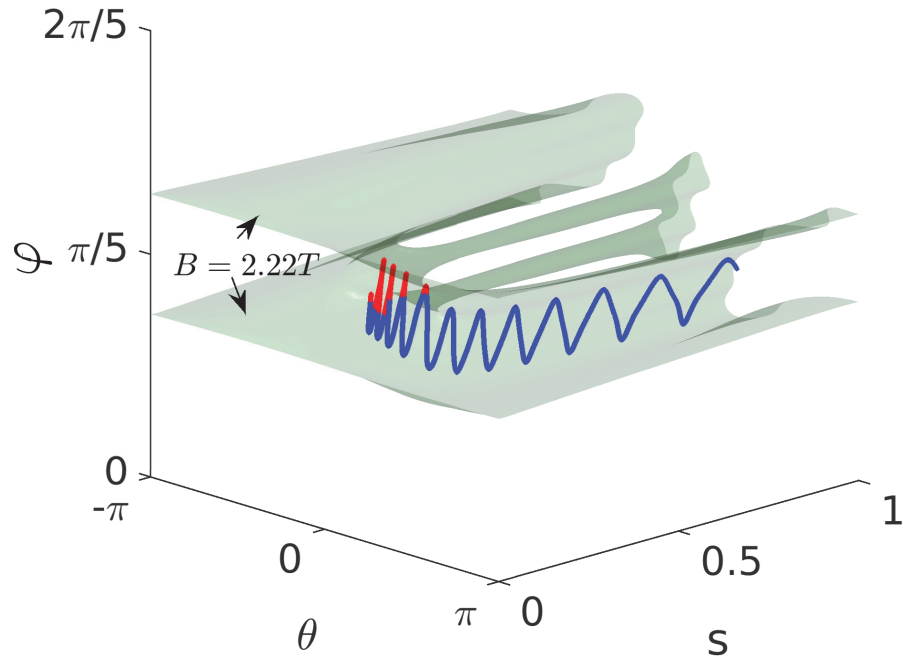
(a) Unconfined trapped particle running along lowest φ value of the $B = B_{ref} = 2.22\,\text{T}$ surface (shown in green).
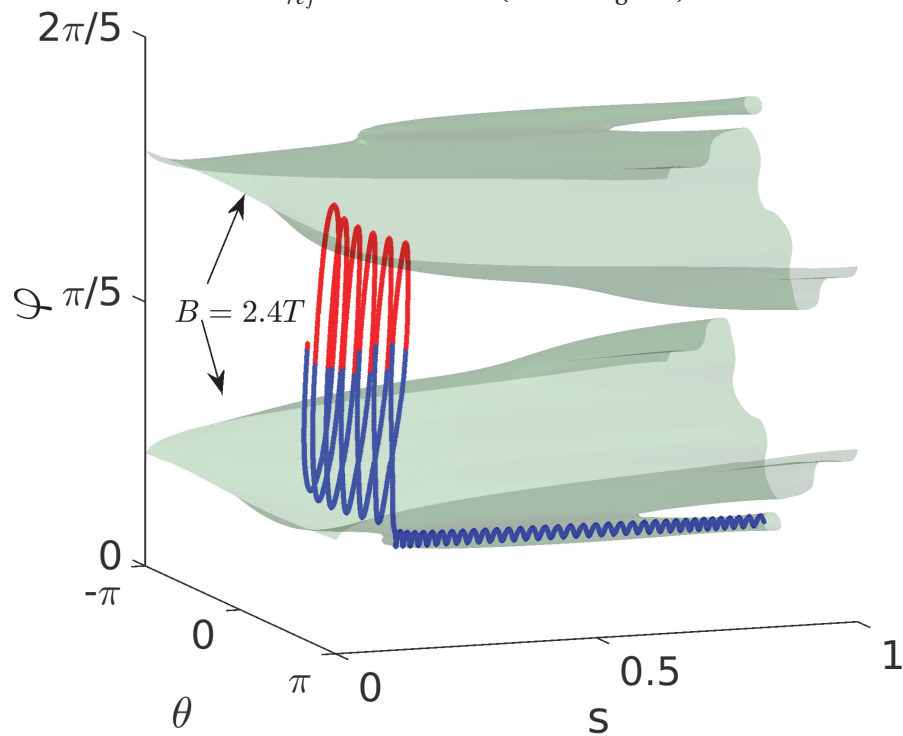
(b) Unconfined trapped particle running along lowest φ value of the $B_{ref} = 2.4\,\text{T}$ surface (shown in green).

Figure 4.5: Examples of unconfined localised particle orbits. The particle guiding centre drift trajectory is traced in each case and is seen to bounce between surfaces of constant $B = B_{ref}$. The color of the trajectory is representative of the local magnetic geodesic curvature sign (blue: $\kappa_g < 0$, red: $\kappa_g > 0$).

4.3.3 Effects of Coulomb collisions

In the presence of collisions, fast ions slow down on the background plasma, causing collisional transport that redistributes them radially. Additionally, as fast ions slow down by colliding with the thermal ions and electrons, they also experience pitch-angle scattering. Therefore a rearrangement of the distribution of particles in phase space occurs that leads to collisional trapping and de-trapping. Deeply trapped particles are expected to be generated by this process and before this particular fraction of the particle population can de-trap, they might experience a significant net outward radial drift because of the mechanism described in the previous subsection. In that sense, collisions give favourable conditions for drift induced losses. This mechanism will be clearly identified by simulations results in Section 4.4.

4.3.4 Effects of ICRF heating

The ICRF acceleration occurs via a diffusive process in velocity space that results in a net increase of the resonant particles energy and magnetic moment after crossing the resonant layer multiple times. It is recalled that for trapped particles, the amplitude of the ambient magnetic field for which the parallel velocity vanishes is given by:

$$B_{ref} = \frac{E}{\mu} = B\left(1 + \frac{v_{\parallel}^2}{v_{\perp}^2}\right). \tag{4.21}$$

After the wave-particle interaction, a resonant particle's perpendicular and parallel velocity is modified as:

$$v_{\parallel,\perp} \rightarrow v_{\parallel,\perp} + \Delta v_{\parallel,\perp}. \tag{4.22}$$

The ICRF wave-particle interaction occurs predominantly in the direction perpendicular to the magnetic field, so that after many interactions, in eq. (4.22): $\Delta_{net} v_{\perp} \gg \Delta_{net} v_{\parallel}$. Inspection of eq. (4.21) under this condition shows that the net energy transfer from the wave to the particle decreases its B_{ref} value until $B_{ref} = B_c = m\omega_{ant}/q$, where ω_{ant} is the wave frequency provided by the antenna excitation. Therefore the ICRF wave is a source of particle trapping and hence in typical 3D configurations, ICRF resonance leads to an enhancement of the drift induced losses. Most of these loss channels described in this section are observed in the VENUS-LEVIS simulations presented in 4.5.2.

4.4 NBI distribution function

In this section, the particle guiding centre orbit solver VENUS-LEVIS and its dedicated NBI module [101] are used to generate and evolve an NBI relevant population in a W7-X high mirror equilibrium. The distribution of lost particles is carefully analysed in order to identify the contribution of each of the loss channels previously discussed.

4.4.1 Initial distribution

In this section, VENUS-LEVIS simulations of fast ions generated by the dedicated NBI module [101] are presented. 147456 markers are generated by this module. Each marker's initial location in phase space (position and velocity) and weight are computed with respect to ionisation and charge exchange processes with the background plasma [102]. The guiding centre orbit solver of VENUS-LEVIS is then used to evolve these markers in time. The simulated particles are deuterium ions at 60keV, 30keV and 20keV and are followed for $1.92 \times 10^{-2} s$. The validity of the guiding centre approximation for such particles in the equilibrium presented in this work can be checked by evaluating the ratio of the particle gyroradius with the scale length of the magnetic field variation [103]. As shown on Fig. 3.7 of Ref. [104], this ratio barely exceeds 10% in most of the W7-X plasma for a 3.5MeV alpha particle. The guiding centre approximation can therefore be considered valid in this study. It is important to mention that it is not intended to model an NBI experiment which would involve continuous injection of fast ions. Instead, special attention is given to the dynamics of fast particles with energy representative of a neutral beam population. Furthermore, it is not intended that the model used should reproduce the W7-X NBI system in its exact geometry. However the injection angles (i.e. the angle between the $\varphi = 0$ plane and the beam line of sight) were set so that the initial distribution in pitch-angle $\lambda = v/v_{||}$ is relevant with the normal and tangential PINIs injecting in the co- and counter direction with respect to the equilibrium toroidal magnetic field, as seen in Fig. 4.6a. An important feature of the initial population for the loss channel analysis is shown by the distribution in $\mu/E = 1/B_{ref}$ plotted in Fig. 4.6b: the fraction of deeply trapped particles, i.e. with $1/B_{ref} > 1/min_{\varphi=0}B \simeq 0.4$ is almost vanishing. It is reminded that the locally passing-trapping boundary depends on the considered drift surface. As the initial marker distribution spans radially across the whole plasma volume, it is not possible to identify a unique passing-trapped boundary. However, an adequate way to estimate the proportion of deeply trapped and deeply passing particles is to consider the inverse of the minimum and of the maximum of the magnetic field amplitude in the bean shaped cross section. These values are plotted in Fig. 4.6b by the two dotted lines. Collisional trapping effects described in 4.3.3 will be easily emphasised simply by comparing the initial and the final fraction of particles with $1/B_{ref} > 1/min_{\varphi=0}B \simeq 0.4$. The initial spatial distribution of the markers is shown in Fig. 4.7.
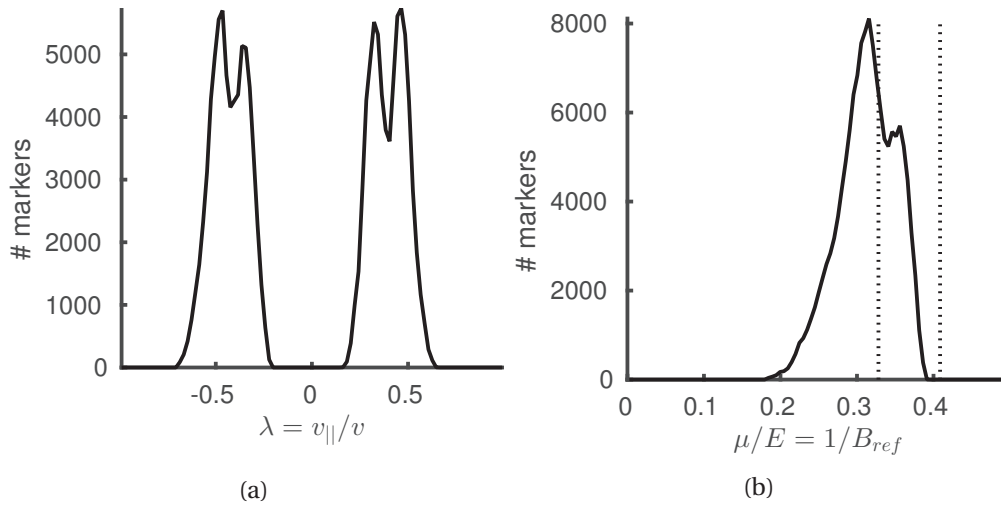
(a)

(b)

Figure 4.6: Initial pitch angle and $1/B_{ref}$ distribution. The dotted lines display the values corresponding to the minimum (left) and the maximum (right) of the magnetic field amplitude in the bean shaped cross section.
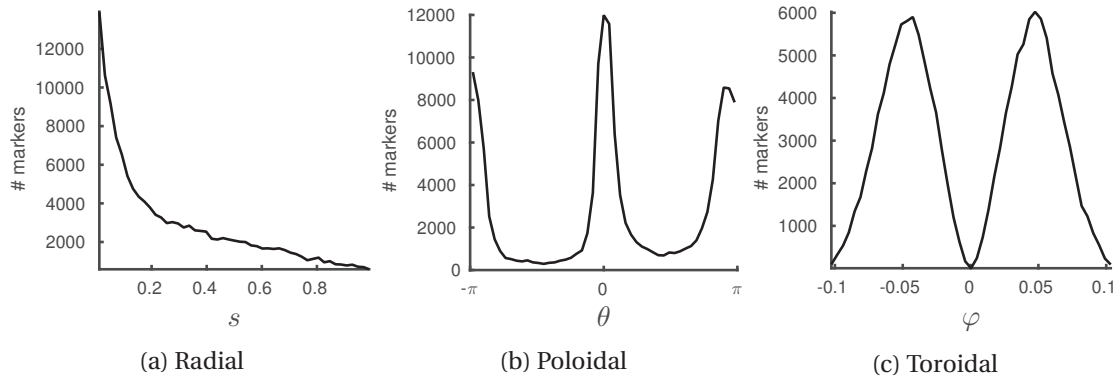

(a) Radial

(b) Poloidal

(c) Toroidal

Figure 4.7: Initial marker distribution in space resulting from the ionisation and charge exchange processes calculations.

4.4.2 Lost particle distribution analysis

The marker population is evolved under slowing down and pitch angle scattering conditions. In VENUS-LEVIS these processes come from the interaction between the fast ions and the background species, i.e no self collisions of the fast ions are considered. The simulation comprises only the confined plasma volume, and as such a marker is recorded as lost as soon as it crosses the LCFS. Figure 4.8 shows the cumulative number of lost markers over time. The loss history is similar for the three investigated initial energies. Markers that cross the LCFS before $t = 1$ms correspond to first orbit losses while losses after 1ms arise from a combination of the collisional and drift induced losses. The latter losses appear to be continuing steadily even after times comparable to the slowing down time of the fast ions. As we will see later, these thermalised particles are ultimately confined with the addition of a radial electric field.
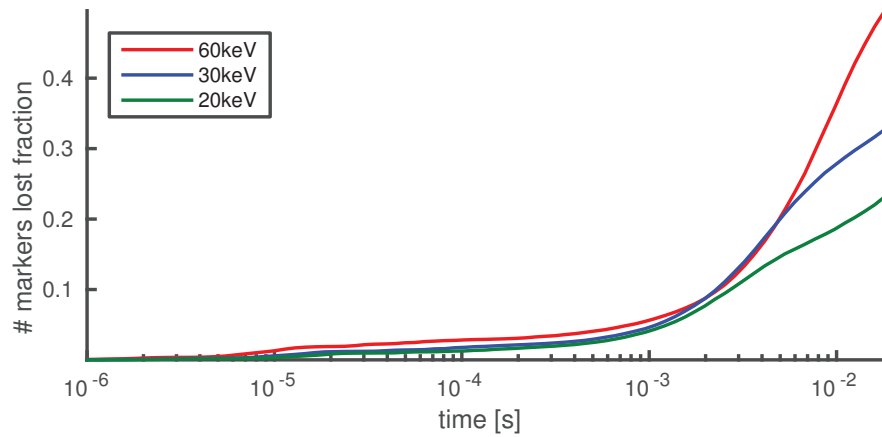
Figure 4.8: Particle losses over time for different injected energy. Two loss regimes appear: first orbit losses (<1ms) and collisional/drift losses (>1ms).

(a) 60 keV co-injected

(b) 60 keV Counter-injected
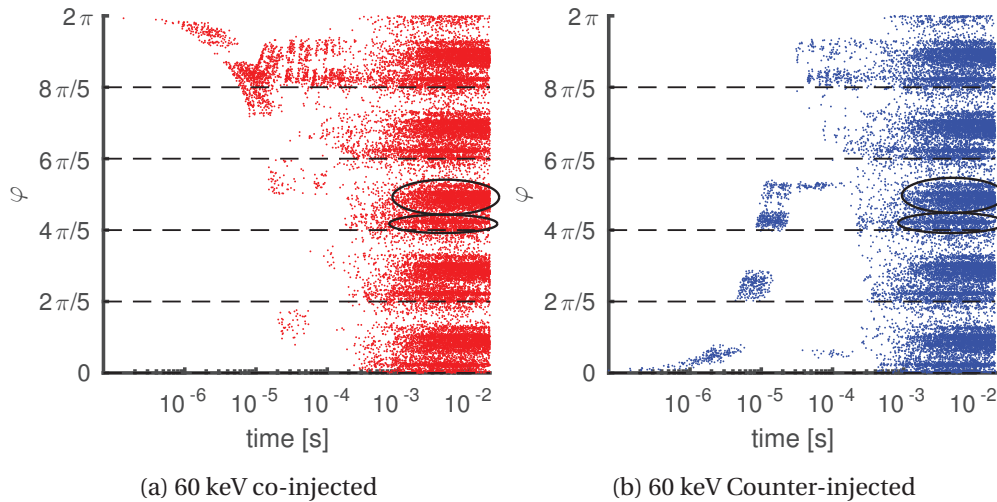
Figure 4.9: Toroidal position of lost markers over time in collisional conditions. First orbit losses clearly appear and display a different pattern for co- and counter- injected particles. After many bounce (or transit) times, the same loss pattern is observed in each toroidal period for a given energy injection. Dashed lines correspond to the boundaries between each toroidal period. Ellipses show examples of particular toroidal positions for loss of particles.

These distinct loss regimes can be also distinguished in Fig. 4.9 which displays the toroidal position at which a marker is lost with respect to its confinement time. These two types of losses are described separately.

First and multiple orbit losses. Fast particles born sufficiently close to the last closed flux surface and with a sufficiently large orbit width may escape the confined plasma volume during their bounce or transit motion. First orbit losses are observed when particles leave the confined volume before completing their bounce motion. In a mirror machine such as W7-X, one may also define multiple bounce (but early) losses since injected trapped particles

can have a positive bounce average radial drift and leave the plasma only after bouncing a few times. First and multiple orbit losses can be seen by the stripe pattern in Fig. 4.9 and illustrated in Fig. 4.10. Multiple orbit losses are typical for stellarator machines and cannot be observed in tokamaks because of the orbit symmetry.

Collisional and drift induced losses. Coulomb collisions with the thermal ions and electrons will not only be responsible for slowing down of particles but also for pitch angle scattering. Therefore collisions can be considered as a source of particle trapping and de-trapping. It is recalled that the fraction of initially deeply trapped particles is nearly vanishing, but as seen in Fig. 4.11 the population of particles lost after 1ms consists mostly of trapped particles.

(a) First orbit losses

(b) multiple orbit losses
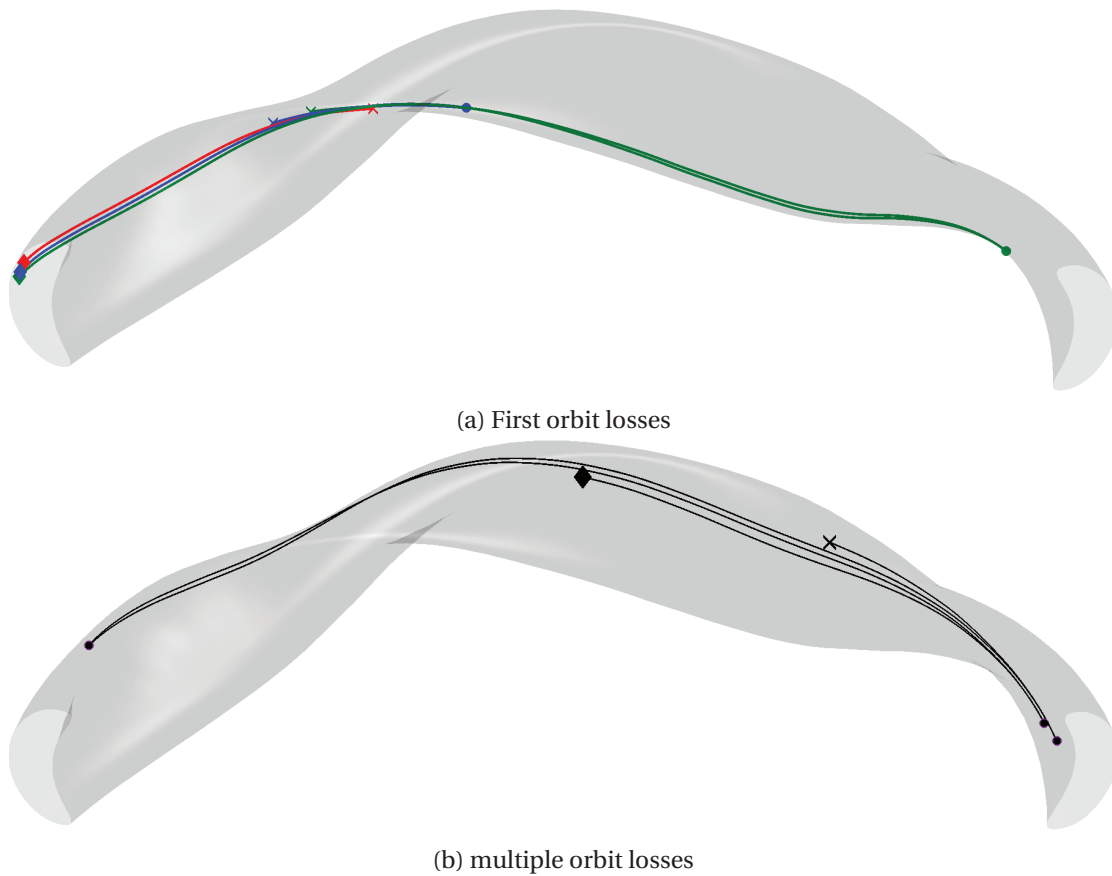
Figure 4.10: Example of first and multiple orbit losses. ♦: initial positions, •: bounce tips, ×: lost positions.
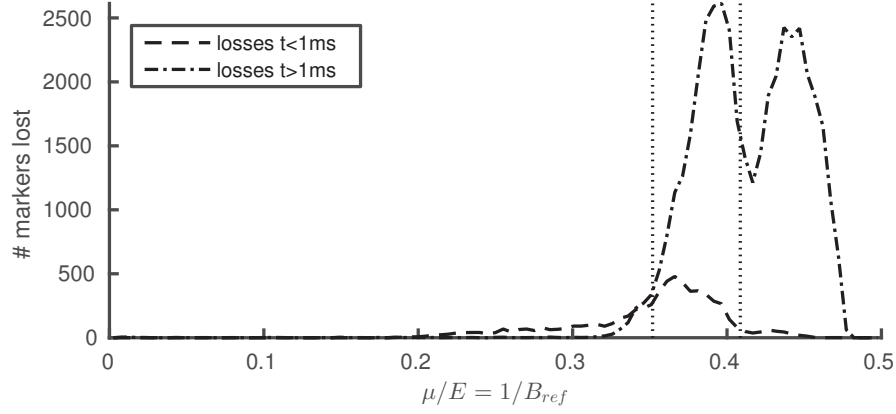
Figure 4.11: Particle losses as a function of their pitch angle variable μ/E.

Particles that can be identified as being in a deeply trapped state and being lost after 1ms represent 53% of the total number of losses after that time (the second peak on the dash-dotted line in Fig. 4.11). This means that not only will particles undergo collisional transport (diffusion in position space) but also wander in and out of the trapped region of phase space via pitch angle scattering (diffusion in velocity space). During the time in which particles remain deeply trapped they experience a net outward radial drift as described in 4.3.2. Additionally, the two peaks in Fig. 4.11 are retrieved at particular toroidal positions in Fig. 4.9 where dense clouds of points are observed in particular locations of each toroidal segment. These locations corresponds to local magnetic wells in which particles are locally trapped due to collisions and where they drift out until they exit the plasma. The losses located in the middle of each toroidal segment can be explained by the local magnetic variation around the triangle cross section as seen in Fig. 4.2. A second loss region appears at the entry of the toroidal segments. However, by virtue of the stellarator symmetry [49], local magnetic wells that are found around a (θ, φ) region appear also around $(-\theta, -\varphi)$ since:

$$I_0 B\left(\rho, \theta, \phi\right) = B\left(\rho, -\theta, -\phi\right),\tag{4.23}$$

where I_0 is the symmetry operator defined in Ref. [49]. This operator transforms the covariant components of $\boldsymbol{B}$, since it is a stellarator symmetric vector field as follow:

$$I_0\left[B_s, B_\theta, B_\varphi\right] = \left[-I_0 B_s, I_0 B_\theta, I_0 B_\varphi\right].\tag{4.24}$$

Partial derivatives are transformed as:

$$I_0\left[\frac{\partial}{\partial s}, \frac{\partial}{\partial \theta}, \frac{\partial}{\partial \phi}\right] B = \left[\frac{\partial}{\partial s}, -\frac{\partial}{\partial \theta}, -\frac{\partial}{\partial \phi}\right] I_0 B,\tag{4.25}$$

It then follows from (4.20),(4.24) and (4.25) that the geodesic curvature transforms under stellarator symmetry into:

$$\kappa_g\left(s, \theta, \varphi\right) = -\kappa_g\left(s, -\theta, -\varphi\right).\tag{4.26}$$

Hence, the toroidal asymmetry in the loss pattern can be explained by the changed sign of the geodesic curvature when moving from a local magnetic well location to its sellarator symmetric location. This is confirmed in Fig. 4.12 which shows the geodesic curvature map on the LCFS and the contours of $1/B$.
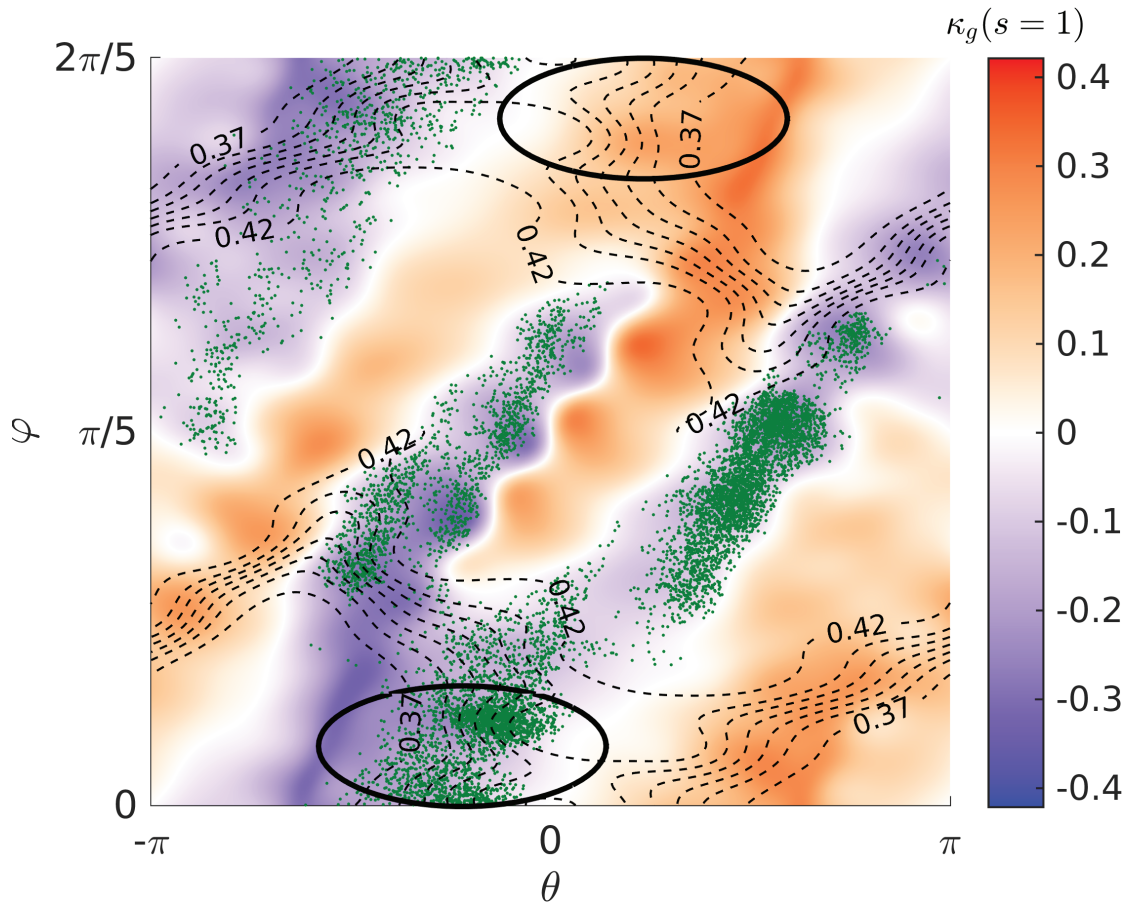

Figure 4.12: Lost particles position in a chosen toroidal segment in the $\theta - \varphi$ plane (green dots). Circles emphasise stellarator symmetric local magnetic wells. Colors show the geodesic curvature amplitude on the LCFS.

4.4.3   Effects of a radial electric field

In this section, the effects of a neoclassically resolved radial electric field are investigated. A radial electric field (E_r) arises from the ambipolarity condition for the neoclassical particle transport of background electrons and ions adding a predominantly poloidal $\boldsymbol{E} \times \boldsymbol{B}$ drift to the particles motion. Therefore it is expected that such an electric field will increase the poloidal drift motion of trapped particles and improve their confinement. The $\boldsymbol{E} \times \boldsymbol{B}$ induced velocity

drift reads as:

$$\boldsymbol{v}_{E\times B} = \frac{\boldsymbol{E}\times\boldsymbol{b}}{B_{\parallel}^*}$$

$$= \frac{E_r}{|\nabla s|BB_{\parallel}^*\sqrt{g}}\left(B_\theta\boldsymbol{e}_\varphi - B_\varphi\boldsymbol{e}_\theta\right) \tag{4.27}$$

Inspection of eqs. (4.27) and (4.16) indicates that the improvement in the particle confinement by the $\boldsymbol{E}\times\boldsymbol{B}$ poloidal drift is less effective for high energy particles. The radial electric field profile used in the following corresponds to the so-called ion-root regime [24] and is displayed in Fig. 4.13a. The profile is extracted from a NBI-heating scenario where 5.5MW of NBI-power is absorbed by a plasma with an electron density of $8\times10^{19}\,m^{-3}$ calculated with the 1-D transport code NTSS described in [105]. Note that the specific form of the radial electric field profile depends on the experimental scenario (heating scenario, density, anomalous transport). The specific E_r-profile here serves as an example to investigate its effect in principle. Figure 4.13b shows an example of how the inclusion of $\boldsymbol{v}_{E\times B}$ helps to confine a trapped particle that would otherwise escape the plasma if only the drifts (4.16) are resolved. The same initial fast ion population as in the previous section was evolved in the presence of this radial electric field.
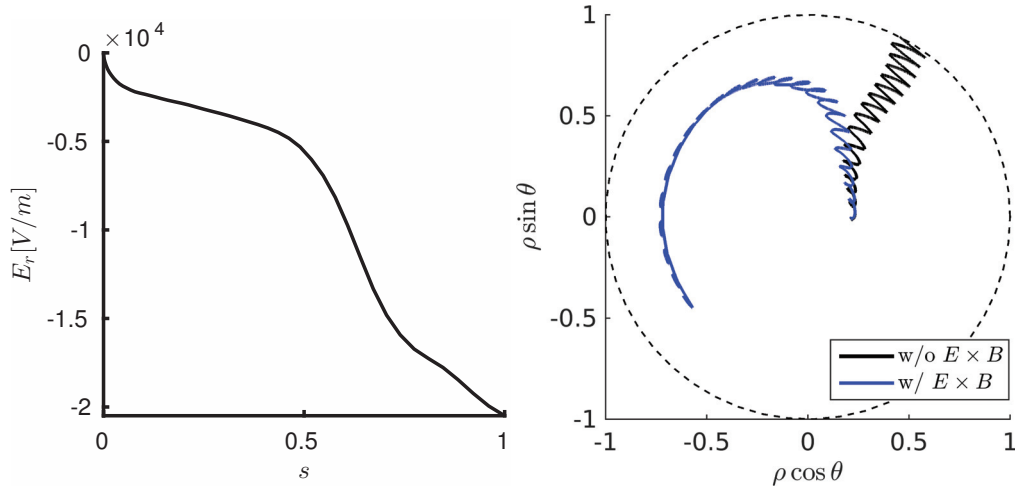
(a) Radial electric profile E_r resolved by neoclassical calculation.

(b) Confinement effect due to the $\boldsymbol{v}_{E\times B}$.

Figure 4.13: Radial electric field profile and its effect on a trapped particle orbit.

A scan in the radial electric field amplitude was performed in order to analyse its effect on the fast ion confinement. Figure 4.14 shows the particle loss fraction over time with varying radial electric field amplitude and initial energy (left to right). Here 100% E_r is the correct level of radial electric field according to neoclassical calculations. It is seen that the fast ion confinement is strongly enhanced. More precisely the number of lost particles saturates with time for a sufficiently high electric field amplitude. In particular, as expected, 20keV

ions experience a larger enhancement in their confinement, and for a realistic electric field amplitude the losses due to the 3D equilibrium configuration stop over times comparable with the particles slowing down time. Furthermore, the radial deposition profile of the injected fast ions is affected by the inclusion of E_r. As seen in Fig. 4.15, for larger electric fields the distribution is more peaked in the central region. Moreover, the edge distribution tends to drop with increasing E_r because of the reduced radial transport. Figures 4.14 and 4.15 show that the radial electric field has a strong influence on the fast ions dynamics in W7-X plasmas. As a concluding remark, this section has shown that future studies concerning fast ion confinement and generation (in particular in W7-X) should include a realistic equilibrium radial electric field at least if the energy of the typical particle is not very large. Indeed, the amplitude of the $\boldsymbol{E} \times \boldsymbol{B}$ drift is independant to the particles energy contrary to the ∇B and curvature drifts (see eqs. 2.20, 2.22 and 2.23). At high energy the effect of the radial electric field becomes negligible compared to the the ∇B and curvature drifts.

(a) 60 keV   (b) 30 keV   (c) 20 keV
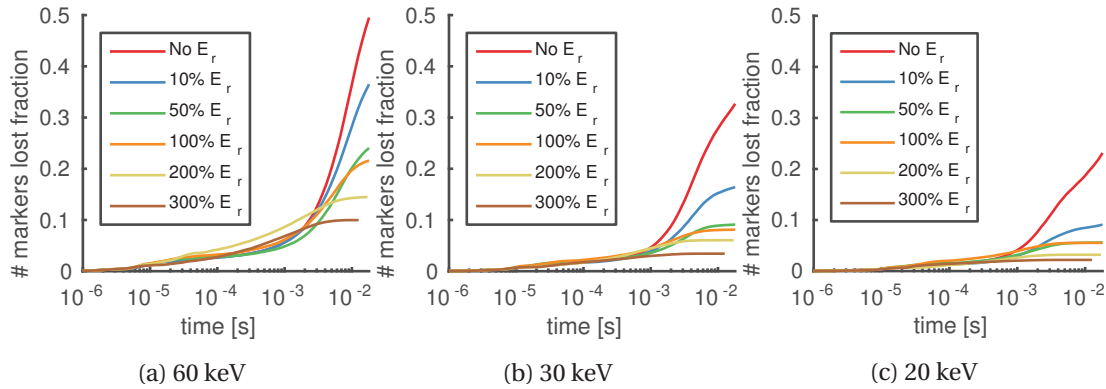
Figure 4.14: Particle lost fraction over time for various radial electric field amplitude and injection energy: a)60 keV, b)30 keV, c)20 keV.

(a) 60 keV   (b) 30 keV   (c) 20 keV
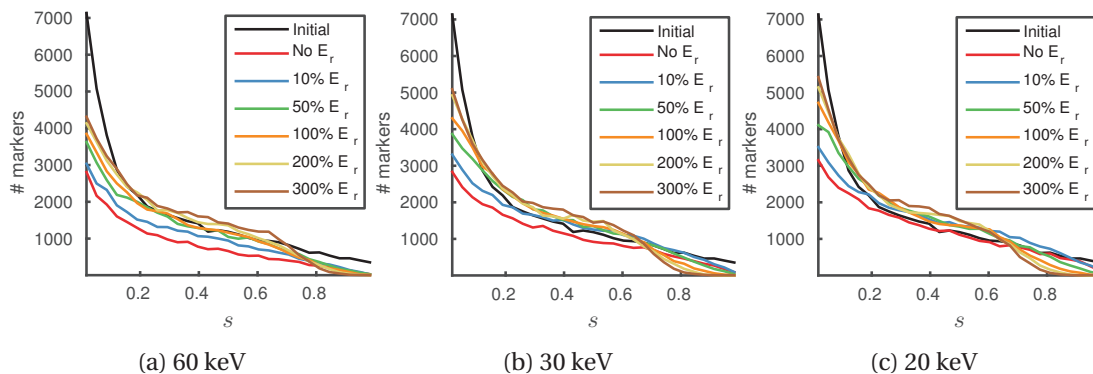
Figure 4.15: Radial deposition profile for various injection energy and radial electric field amplitude at $t = 1.92 \times 10^{-2} s$.

4.5 ICRF distribution function

Sustaining fusion reactions in a magnetic confinement device requires to maintain the plasma temperature to a few keV. In addition to the auxiliary plasma heating methods which are necessary to reach these temperatures, fusion born α particles represent a substantial source of heating. The confinement of these particles for a duration comparable to their slowing down is therefore of primary concern for the design of future fusion reactors. The quasi-isodynamic stellarator concept is seen as a suitable candidate for a future fusion reactor. The task W7-X is to demonstrate the good confinement of α particles. An auxiliary source of fast ions with energy between 50 to 100 keV is therefore required in W7-X. Indeed, ions in that range of energy would mimic the behaviour of α particles in a reactor-size quasi-isodynamic stellarator. In this section, the possibility of producing fast ions using an ICRF minority heating scheme in W7-X is addressed. A localised antenna model is adopted in order to account for the three-dimensional structure of the equilibrium. The analysis of the resulting ICRF particle distribution function provides an understanding of the particle loss mechanisms. The generation of tails associated with ICRF heating in W7-X standard and high-mirror configurations is investigated.

4.5.1 Antenna setup and wave deposition

In three-dimensional plasmas, the antenna treatment applied in section 3.1 cannot be performed because of the strong coupling that also exists between the toroidal modes. In this case, the antenna can be modelled with the following σ function:

$$\varsigma\left(s,\theta,\varphi\right) = \prod_{X=s,\theta,\varphi} \left(1 - \left(2\frac{X-X_1}{X_2-X_1} - 1\right)^2\right)^2 \mathscr{B}\left(\frac{X-X_1}{X_2-X_1}\right) \tag{4.28}$$

Such a model does not give as much flexibility on the current straps phasing as the model implemented for two-dimensional equilibrium, but allows the localisation of the antenna excitation with realistic geometry. The W7-X ICRF antenna system to be installed for operation phase (OP) 1.2 is described in Ref. [106] and is used to the model the current density in a realistic configuration. The excitation model is applied to solve for the fast wave deposition in a W7-X Deuterium rich plasma with 0.5% Hydrogen minority. The central density and temperature were respectively set to $n_0 = 1.55 \times 10^{20} m^{-3}$ and $T_0 = 4.5 keV$ for the standard equilibrium and $n_0 = 1.5 \times 10^{20} m^{-3}$ and $T_0 = 4 keV$ for the high-mirror configuration. These values of density and temperature were chosen in order to ensure a converged equilibrium with $\langle\beta\rangle \simeq 4\%$ for each configuration. The excitation frequency was respectively set to 38.1MHz and 39.6MHz for the high-mirror and standard mirror cases. The right-handed wave electric field amplitude around the midplane is displayed in Fig. 4.16. These wave fields were obtained from calculations with the LEMan code performed on the IFERC-HELIOS supercomputer in Rokkasho, Japan. The Fourier decomposition of the wave propagation problem with the localised antenna model (eq. 4.28) required the use of 1024 mode pairs. It is worth mentioning

that better resolved calculations would be obtain with increasing number of mode pairs but would involve increasing computational resource consumption. The computation of each wave field presented in Fig. 4.16 consumed 1152 node hours and used up to 256 GB of memory. As previously described in ref. [107], the localisation of the antenna excitation is seen in the toroidal dependency of the electric field. The modeled antenna is located in the toroidal period spanning the domain $\varphi = [0, 2\pi/5]$, and is the locus of the highest electric field amplitude. The other toroidal periods are further from the excitation source and display reduced electric field amplitude. The five-fold symmetry breaking is explained by considering the damping of the wave as it travels toroidally and crosses the resonant layers. Figure 4.16 also illustrates the effect of the magnetic configuration on the wave propagation. As mentioned in section 4.2.2, the resonance layer disappears from the confined plasma volume in certain regions of the high-mirror configuration. Therefore the wave is not absorbed continuously as it propagates toroidally, and as a result the amplitude is not strongly damped toroidally.
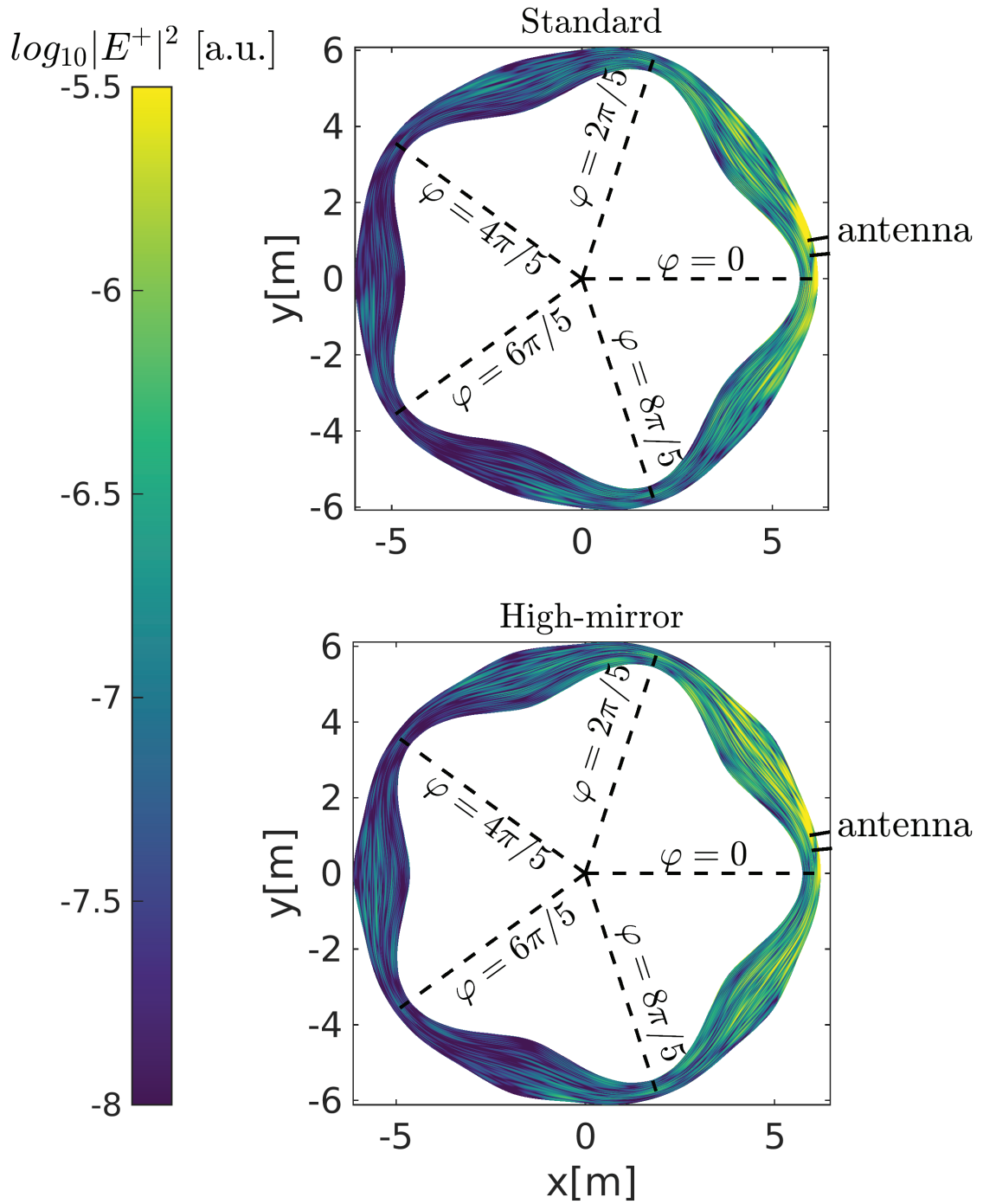
Figure 4.16: Right-handed electric field amplitude distribution (log scale) around the midplane [a.u.] for the standard (top) and the high-mirror (bottom) W7-X configuration.

4.5.2 Confined and lost particle distribution analysis

Confined particles

The VENUS-LEVIS code [19] is used to resolve the guiding centre orbits of the H minority ions. Monte Carlo operators [55] are implemented in order to compute the Coulomb collisions with the thermal ions and electrons and the ICRF wave-particle interaction [108]. The electric field and wave numbers computed by the `LEMan` code where the localised antenna model is used. The simulated ICRF power is set to 1.5MW which corresponds to a realistic power under the assumption of perfect antenna-plasma coupling. The energy transfer to and from the minority ions is given particular attention. It is important to state that the wave energy is considered to be absorbed uniquely by the minority species. However, given the minority concentration used (0.5%) and the choice of the plasma ion species, a non negligible fraction of the power is expected to be absorbed by the Deuterium ions by second harmonic wave-particle interaction. As mentioned earlier, it is not our intention to provide fully realistic ICRF heating scenario simulations but instead the principle of generating and confining a fast particle population with ICRF heating in a high density stellarator plasma is investigated. A thermal population of $2'097'152$ H markers is initialised in both equilibria. The minimum energy for the marker initialisation was set to 1keV because only the behaviour of supra-thermal particles are of interest in this work. These markers are evolved for a time equivalent to a fourth of a slowing down time. The resulting energy distribution functions are displayed in Fig. 4.17. A case that has been obtained from a `SCENIC` simulation of a JET plasma run for a fourth of a slowing down time with 1.5MW power is also shown comparison. As described in [108] and as illustrated in
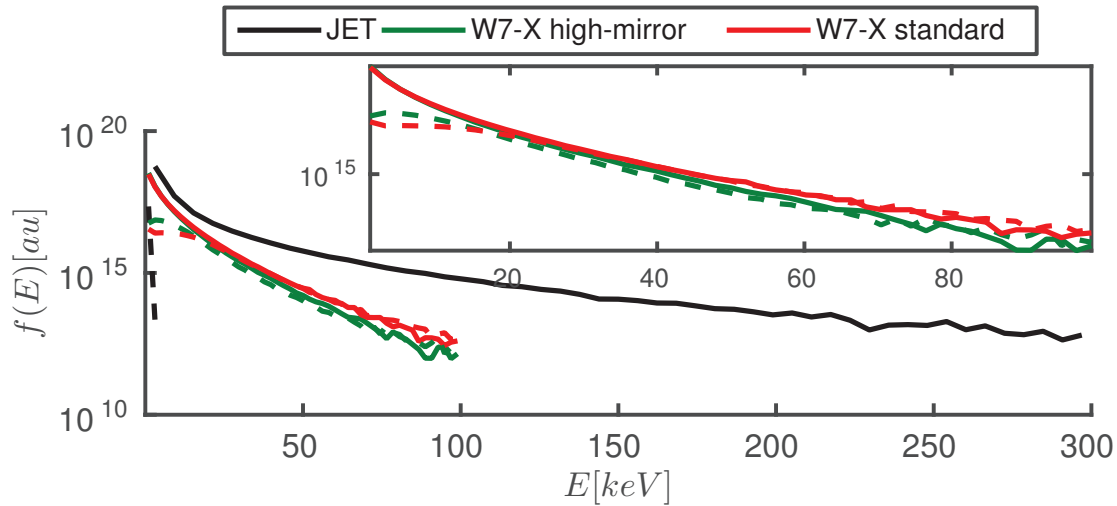
Figure 4.17: Distribution function in energy of confined vs lost minority ions for the two investigated W7-X configurations compared with a JET case. Dashed lines show the lost particle energy distribution, which for the JET case is seen to be negligible and comparable to the confined particles for the W7-X cases.

Fig. 4.18, a splitting of the tail and the thermal bulk of the final distribution can be performed

in minority ICRF heating scenarios. In typical SCENIC simulations, the hot component of the particle distribution is fitted to the bi-Maxwellian model described in Ref. [44], and the corresponding moments are then used to update the plasma equilibrium and the ICRF wave deposition consistently with the hot particle contribution [108]. Several iterations between the 3 components of the SCENIC package allows the computation of a self-consistent distribution function. However, the fast component of the distributions for the W7-X cases of Fig. 4.17
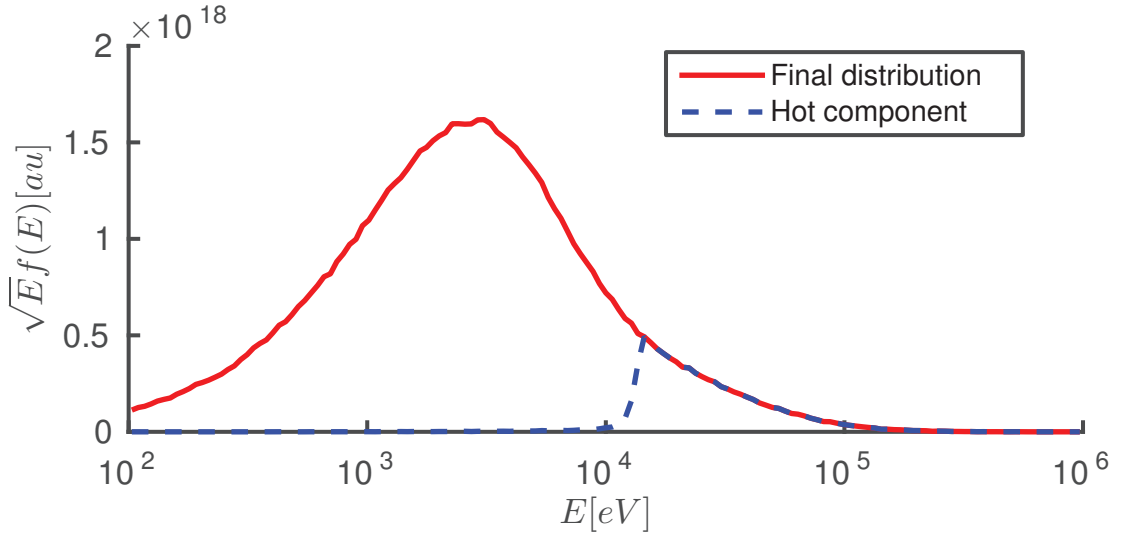
Figure 4.18: ICRF distribution and its corresponding hot component obtained from a JET equilibrium.

are nearly vanishing. This can mainly be explained by the high density of W7-X plasmas. It is known from [32] and [41] that the minority energy range scales like $1/n_e^2$. The SCENIC iteration scheme cannot straightforwardly be applied using the usual procedure applied for tokamaks, but the particle distribution can still be analysed. Moreover, it is seen in Fig. 4.17 that the distribution of lost particles, i.e. particles which cross the LCFS, represents a significant fraction of the initial distribution: $\sim 12\%$ of the markers are lost during those simulations. The markers have the same numerical weight, so that the fraction of lost markers represents the same number of lost particles. The amount of losses in a similar scenario applied to an axisymmetric JET tokamak plasma is nearly vanishing mainly because of the symmetry of trapped particle orbits in such a configuration. Note that changing the equilibrium from a standard to a high-mirror configuration seems only to affect the wave deposition pattern as seen in Fig. 4.16. Indeed, the change in the fast ion tail and the lost particle distribution appears to be negligible. Therefore, the analysis of the loss channels under ICRF conditions carried out in the next section focuses on the high-mirror configuration. It will be seen later however that the losses can be reduced significantly by including neoclassically resolved electric fields.

Lost particles

The most significant loss channels introduced in Section 4.3 act predominantly on trapped particles. Figure 4.19 correlates the amount of lost markers for a given pitch angle variable $1/B_{ref} = \mu/E$. In this figure, the vertical dotted lines locate the particular value $1/max\ B|_{\phi=0}$ and $1/min\ B|_{\phi=0}$. These lines give an estimation of the fraction of deeply passing and deeply trapped particles. As suggested in Section 4.3, pitch angle scattering produced by Coulomb collisions can generate deeply trapped particles which escape the confined volume via the drift induced loss mechanism. This mechanism explain the loss pattern observed when no ICRF heating is applied (dashed line in Fig. 4.19). It is seen that the losses practically do not affect passing particles. On the other deeply trapped particles localised around the triangular cross section experience significantly this loss mechanism as seen by the peak in the region $1/Bref > 1/min\ B|_{\phi=0}$. In addition to this effect, the ICRF wave absorption brings resonating particles into a locally trapped state, therefore increasing the fraction of particles experiencing drift induced losses. In Fig. 4.19, this is illustrated by the first (small) peak in the dash-dotted line. The corresponding B_{ref} value for this peak matches the chosen value of B_c for this simulation. This is caused by the alignment mechanism of the particles bounce tip with the resonant layers described in section 4.3.
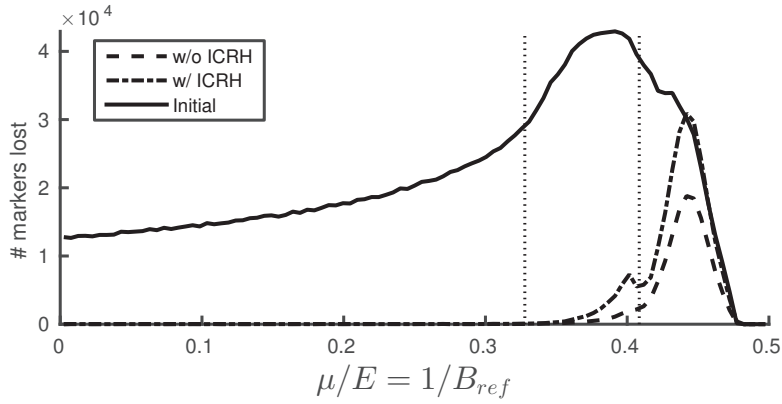
Figure 4.19: Number of lost markers as a function of their pitch angle variable μ/E. All markers located to the left (resp. right) of $1/max\ B|_{\phi=0}$ (resp. $1/min\ B|_{\phi=0}$) are deeply passing (resp. trapped). The peak on dash-dotted line at $\mu/E = 0.4$ corresponds to $1/B_c$.

The choice of B_c, and therefore of the ICRF frequency, has then a direct impact on the fraction of lost particles. Figure 4.20 compares the number of lost markers for different values of B_c, showing significant increases as B_c decreases from $2.5T$ to $2.4T$ and to $2.22T$. As expected from the trapping mechanism described earlier, the largest peak in the number of lost markers is observed at $1/B_{ref} = 1/B_c$.
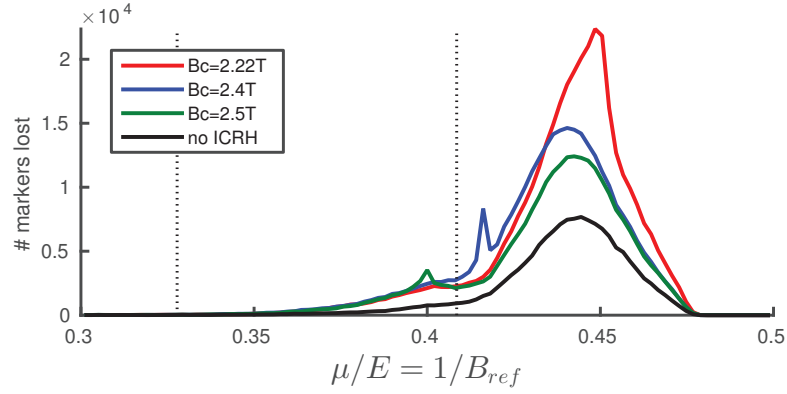
Figure 4.20: Number of lost markers as a function of their pitch angle variable μ/E for various ICRF frequencies. The location of peaks corresponding to enhanced particle losses due to ICRF moves from $\mu/E = 0.4$ ($B_c = 2.5\,T$) to $\mu/E \simeq 0.416$ ($B_c = 2.4\,T$) and to $\mu/E = 0.45$ ($B_c \simeq 2.22\,T$)

The change in the ICRF frequency also changes the toroidal region covered by the resonant layer which in turn influences the number of particles in the trapped region of phase-space. Indeed, for lower values of B_c, e.g. $2.22\,T$, the resonant layers are mostly located around the triangle cross section. In this case, the resonant particles' motion converts into a toroidally trapped state which causes these particles to bounce between two poloidally closed isosurfaces (i.e. that entirely cover the $\theta = [0, 2\pi]$ domain) at $B = B_c = B_{ref}$. These particles can strongly experience the drift induced loss channel described earlier. Locally passing particles are usually well magnetically confined as it has been previously described. On the other hand confining deeply trapped and energetic particles using only the magnetic equilibrium structure is one of the main challenges of the quasi-isodynamic stellarator configuration because their bounce averaged poloidal drift motion, especially at high energies, may not compensate their outward radial drift. As it was mentioned in section 4.3 where eq. (4.19) was defined, these deeply trapped particles are lost because their trajectory is mostly located in regions of negative geodesic curvature. On the other hand, higher values of B_c, e.g. $2.5\,T$, correspond to resonant layers mostly located around the bean-shaped cross section. As seen in Fig. 4.21, the isosurfaces $B = B_c = B_{ref}$ are poloidally open (isosurfaces that do not span the entire poloidal domain $\theta = [0, 2\pi]$) for $B_c = 2.5\,T$ at $s = 0.25$. Therefore particles interacting with the ICRF wave are moved towards a helically trapped state, i.e. they can become locally passing by collisionless de-trapping. The drift induced loss mechanism is consequently less efficient for this fraction of trapped particles, thus explaining the reduced number of lost markers with increasing value of B_c as observed in Fig. 4.20.

The loss patterns are also marked by the wave localisation. It is seen in Fig. 4.22 that the losses are enhanced in the toroidal period containing the antenna (and to a lesser extent the adjacent one) compared to the losses in the other periods. As expected from the drift induced loss mechanism, particle losses are toroidally localised around local magnetic wells as seen from the black curve in Fig. 4.22. It is expected that pitch-angle scattering provided by Coulomb collisions re-distributes particles in phase-space until they eventually trap in a local magnetic
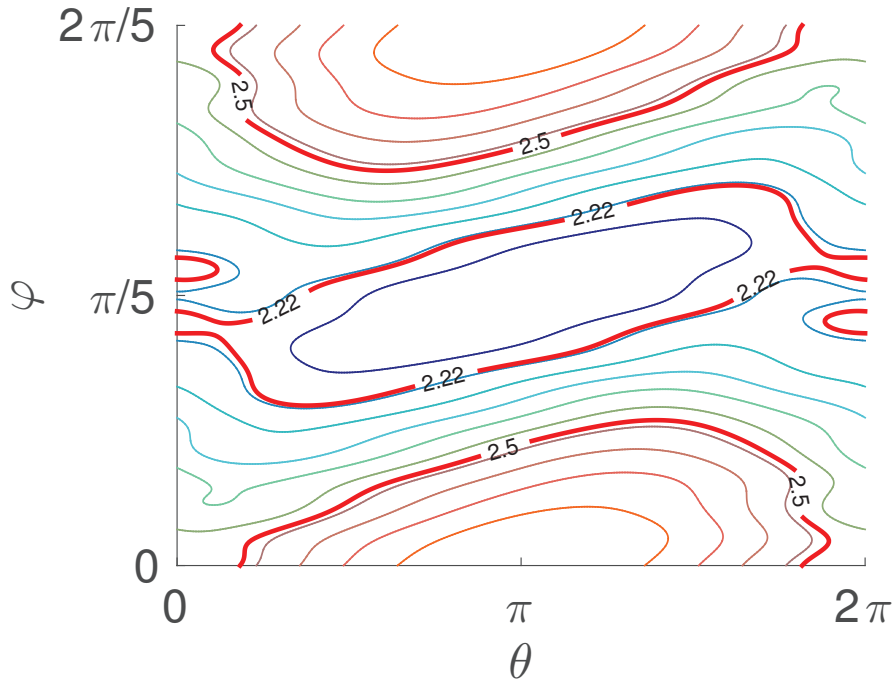
Figure 4.21: Contours of constant $|B|$ in the $\theta - \varphi$ plane at $s = 0.25$. The large peaks seen in figs. 4.19 and 4.20 correspond to particle trapped between poloidally closed isosurfaces of B (e.g. 2.22T).
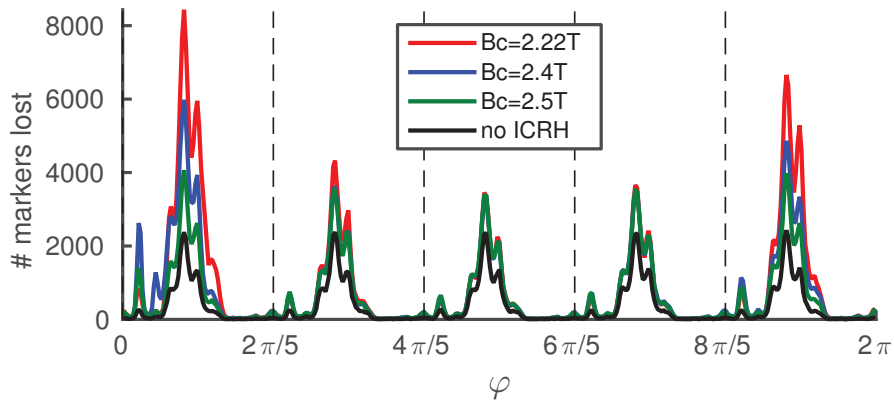

Figure 4.22: Number of lost markers with respect to their toroidal position. If the antenna was not localised, the total number of lost markers is expected to be higher than in the work presented here.

well and possibly drift out of the plasma. In addition to this redistribution, ICRF heating traps particles in particular magnetic wells which corresponds to the chosen frequency, or B_c value. Finally, there is a remarkable asymmetry in the loss patterns observed in each single period (e.g., a peak at the entrance of each period not found at the other end of the period) which was explained in Ref. [109] by the stellarator anti-symmetric feature of the geodesic curvature.

4.5.3 Effect of a radial electric field

The radial electric field profile introduced in section 4.4.3 is now used to study the principle effects of E_r on the distribution function of lost particles and the fast tail generation. The guiding centre simulation presented in section 4.5.2 with $B_c = 2.5 T$ is re-run with the inclusion of E_r. The high equilibrium background density and the relatively low ICRF heating power dictate that the minority ions remain mostly thermal and therefore undergo strong $\boldsymbol{E} \times \boldsymbol{B}$ drift. For low ICRF heating power (where energies and hence ∇B and curvature drifts are relatively small) such as 1.5 MW, the number of lost markers represents a negligible fraction of the initial markers population as seen in Fig. 4.23.
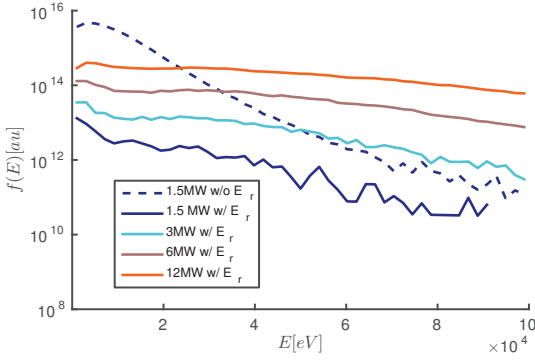
Figure 4.23: Distribution functions in energy of lost minority ions with various ICRF power levels in W7-X. The dashed blue case does not include E_r.
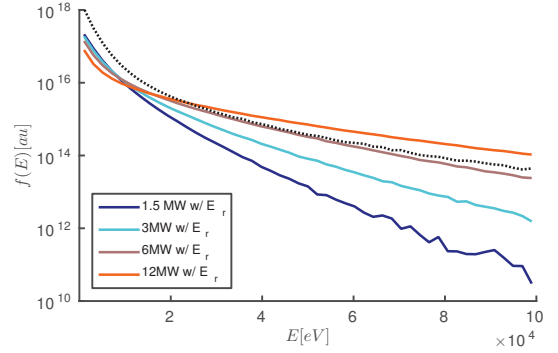
Figure 4.24: Distribution functions in energy of confined minority with various ICRF power levels in W7-X. The dotted line shows for comparison the distribution obtained the JET plasma simulation introduced in section 4.5.2 (with 1.5 MW of power).

The fraction of fast ions in the total minority species distribution function remains relatively low for 1.5 MW. As is well known [32], the energy range reached by the minority species scales with the coupled ICRF power P_{RF}. It is seen from Fig. 4.23 that the particle losses follow roughly the same scaling because higher kicks to the particles' perpendicular velocity increase inevitably the radial drift, see eq. (4.19). Distribution functions of confined particles resulting from the scan in P_{RF} is shown in Fig. 4.24. The possibility of generating fast ions at higher heating power is observed for these cases where the radial electric field assists confinement. As P_{RF} increases, the fast ion tail of the distribution grows and becomes similar to the JET-like simulation introduced in section 4.5.2 for $P_{RF} = 6$ MW. However, this amount of coupled power, under the assumption of perfect wave-plasma coupling, is well above the expected maximum available power during OP1.2 [106]. Therefore the minority ICRF heating scheme does not appear to be suitable for fast ion generation in W7-X.

4.6   Summary

In this chapter, the dynamics of fast ions produced by NBI and ICRF minority heating have been explored. Fast particle loss channels have been identified. First the stochastic radial diffusion described in Ref. [23] is expected to play a significant role for high energy (i.e. low collisional) particles confined for a long time. Losses of NBI populations were seen to exhibit two regimes. The first one involves first and multiple orbit losses. The second regime is explained by a drift induced loss mechanism. In this regime, Coulomb collisions will cause classical transport but more importantly will generate deeply trapped particles via pitch angle scattering. Trapped particles generated by this scattering process are mostly transported outside the plasma by the drift induced loss channel.

The possibility of generating a fast ion tail with minority ICRF heating has been assessed. The investigation of NBI ions helped to understand the particle losses observed under ICRF heating conditions. Simulations obtained with the 3D full-wave code `LEMan` show that the localisation of the antenna system induces a wave deposition that breaks the five fold periodicity of W7-X. This wave field has been used with the guiding centre orbit VENUS-LEVIS in order to resolve the wave-particle interaction. The particle loss patterns characterising the investigated ICRF heated W7-X plasma scenarios have been assessed. Particle losses are mostly due to a drift induced loss mechanism. Pitch angle scattering produced by Coulomb collisions is a source of particle trapping and de-trapping and consequently enhances the drift induced losses. ICRF heating is also found to enhance this loss channel because the wave-particle interaction in the perpendicular direction is a source of particle trapping. Consequently, the toroidal positions of lost particles are influenced by the wave localisation.

The effects of a radial electric computed by neoclassical transport simulations have been considered. The inclusion of the $E \times B$ drift leads to a more complete description of the particle dynamics and shows a strong reduction of the losses in both NBI and ICRF heating simulations. However, this does not appear to be sufficient for producing a fast ion tail distribution for experimental fast particle confinement studies with 1.5MW of coupled ICRF power. Regardless of the heating scheme, it seems reasonable that fast ions will be mostly located in the toroidal period containing the antenna and the one adjacent to it because of the RF trapping effect.

5 Exploring a new ICRF scenario : the three-ion species scheme

The most used ICRF scenario in fusion devices is known as the minority heating scheme [32]. Applied to JET tokamak plasmas, this scheme generates fast minority ions with energies above 100 keV as seen in chapter 2.4. ICRF waves are seen as a possible substantial source of fast ion generation in W7-X, potentially with typical energies (in the tail of the distribution) of around 50-100 keV. The possibility of using fundamental minority heating in W7-X was discussed in chapter 3.6. It was found that under relevant ICRF conditions (spatially localised antenna and 1.5 MW of input power) significant loss of particles are observed and the fast ion tail, usually found in axisymmetric tokamak scenarios, is nearly vanishing. Even though the particle losses were seen to significantly decrease in simulations by the inclusion of a radial electric field originating from the ambipolar diffusion of background electrons and ions, the formation of a fast ion tail remains hindered by the high plasma density. An important aspect to take into account in the elaboration of efficient ICRF fast ion generation scenarios is the waves electric field polarisation at the resonance position. In typical minority heating schemes, the polarisation is dictated by the ionic species, and thus limits the amount of coupled power to the minority ions as discussed in Ref. [41]. In the latter work, the three-ion species scheme was presented as a scenario that optimises the wave polarisation at the resonant species position and offers tremendous potential for fast generation with moderate input RF power. In this chapter we first present in section 5.1 the working principle of the three-ion species scheme. Numerical results obtained with the full wave code `LEMan` applied to an axisymmetric configuration are presented, and in particular display the key features of this ICRF scheme. In section 5.2, simulations of the three-ion species scheme obtained with the `SCENIC` package applied to an axisymmetric configuration are presented. The effect of varying the ICRF antenna phasing on the self-consistent ^{3}He ion distribution function is addressed. The possibility of generating fast ions with the three-ion species scheme applied to a high-mirror W7-X configuration is discussed in section 5.3. Conclusions are drawn in

section 5.4.

5.1 The three-ion species scheme

In this section, we review the working principles of the three-ion species scheme. As explained in Ref. [41] (to which the reader is referred for a detailed discussion about this scheme's principles and applications), this scheme requires the presence of two main ion species in the plasma. A third ion species, whose purpose is to absorb the wave energy at the fundamental ion-cyclotron resonance, is introduced in low concentration. The relative concentration of each species dictates the behaviour of the plasma dielectric tensor and hence of the local fast wave dispersion relation. If one defines as $n_\perp$ and $n_\parallel$ the refractive indices in the perpendicular and parallel direction to the magnetic field lines, ϵ_R, ϵ_L and ϵ_S the dielectric tensor elements as given by Stix in ref. [32], the dispersion relation for the fast wave reads:

$$n_\perp^2 = \frac{\left(\epsilon_R - n_\parallel^2\right)\left(\epsilon_L - n_\parallel^2\right)}{\left(\epsilon_S - n_\parallel^2\right)}. \tag{5.1}$$

In the vicinity of the L-cutoff, the term $\left(\epsilon_L - n_\parallel^2\right)$ approaches zero such that the electric field component E^- which rotates in the same direction as the electrons is almost vanishing. In this region, the electric field component E^+ which accelerates resonant ions therefore carries almost all of the wave energy. The fast wave L-cutoff position is mainly dependent on the ion species concentration. The prerequisite for maximising the absorbed power on the third ion species is then to find the appropriate plasma mixture such that this cutoff is located in the low-field side (LFS) vicinity of this species' fundamental cyclotron resonance position. A typical JET-like plasma equilibrium is initially chosen in order to verify that the full-wave code LEMan is able to model the scheme. The plasma modelled here consists mainly of a mixture of hydrogen and deuterium. The third species is ^{3}He with a concentration as low as 0.1%. The electron density and temperature profiles used result from analytic estimates and read: $n_e = [3.6 \times (1 - r^2) + 0.4] \times 10^{19}\,\text{m}^{-3}$, $T_e = [3 \times (1 - r^2)^{3/2} + 1]\,\text{keV}$ where r is the normalised minor radius. The magnetic axis is located at $R_0 = 2.96\,\text{m}$ and the central magnetic field strength is $B_0 = 3.2\,\text{T}$. We model the JET ICRF spectrum with a single toroidal wave mode number ($n_\varphi = 27$) which is propagating in the plasma at a frequency $f = 32.5\,\text{MHz}$. The choice of frequency yields an on-axis ^{3}He fundamental resonance. Figure 5.1 shows the fraction of power absorbed by each species in the plasma when varying the H concentration for this test case. A peak of ^{3}He absorption clearly appears around $[H] = \frac{n_H}{n_e} \simeq 70\%$ which is in accordance with optimal mix calculations established in [41].
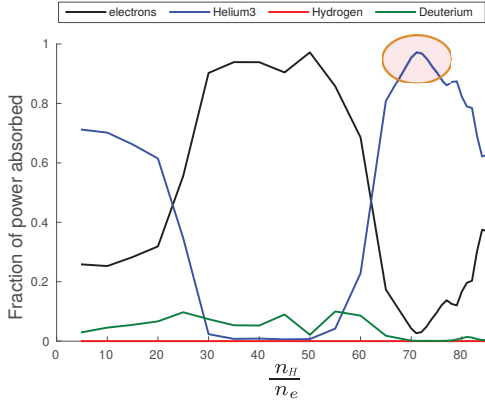
Figure 5.1: Fraction of power deposited on each species for varying H concentration.
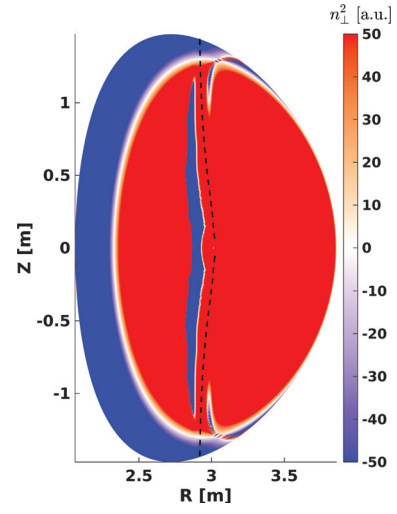

Figure 5.2: Local dispersion relation given by eq. 5.1. Evanescent and propagative regions respectively appear in blue and red. Cutoffs appears as white lines at the border of these regions. The black dashed lines shows the fundamental ^{3}He resonant position.

The full-wave code LEMan [50, 51] is used to compute the dispersion relation given by eq. (5.1) which is showed in fig. 5.2. The plasma mix in this case is $[H] = 68\%, [D] = 31.8\%, [^3He] = 0.1\%$. As seen in fig. 5.2, the ^{3}He fundamental cyclotron resonance position is in the vicinity of the L-cutoff confirming that this configuration is favourable for the three-ion species scheme. Fig. 5.1 also suggests that in the absence of other impurities, only electrons absorb a significant part of the RF power. As discussed in Ref. [41], an efficient absorption of RF power by ^{3}He ions was computed with the TORIC, EVE and TOMCAT codes. Therefore a scan in ^{3}He concentration is performed with the LEMan code and is shown in Fig. 5.3. It is important to mention that the LEMan code is missing the power absorption by electrons via Transit Time Magnetic Pumping [32]. Therefore it expected that the LEMan code underestimates the electron damping in scenarios where this branch is expected to dominate, typically for two-ion species scenarios with very low or high minority concentration. However, Fig. 5.3 is in good agreement with results from Ref. [41]: ^{3}He concentration for maximal power absorption is around 0.1%.
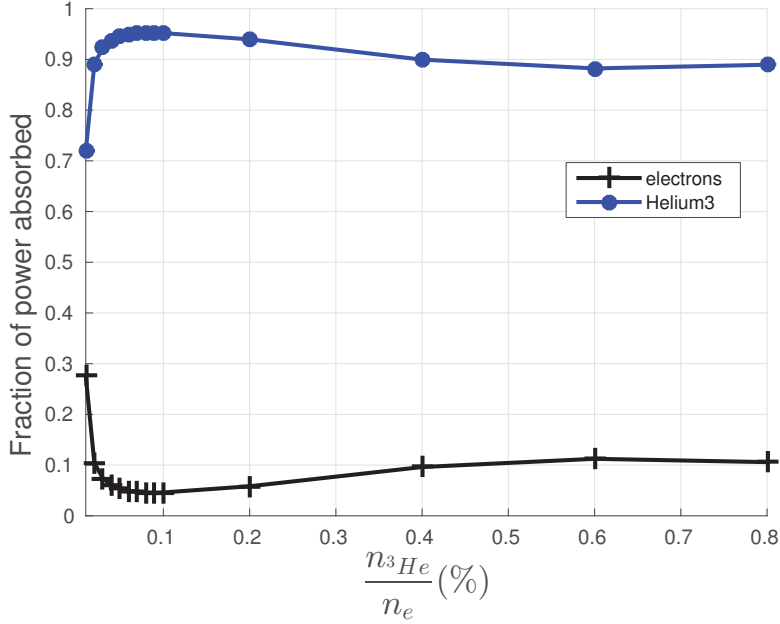
Figure 5.3: Fraction of absorbed power on ^{3}He and electrons with varying ^{3}He concentration.

5.2 Two-dimensional modelling: JET-like axisymmetric plasma

In this section, the SCENIC [53] package is applied to resolve fast ion distribution functions using the (^{3}He)-D-H ICRF scenario applied to a JET-like axisymmetric plasma. The VMEC/ANIMEC code [11] is used to construct an ideal MHD equilibrium based on typical JET tokamak plasma geometry and the density and temperature profiles mentioned in the previous section. We will apply two different antenna phasings. The phasing has been shown to play an important role in particular on the resonant ion orbits due to the RF particle pinch. This effect has been discussed in [57, 58], and experimental observations have been reported in [59, 60]. The direction of the RF-pinch (inward or outward) can be controlled by the use of a toroidally asymmetric excitation spectrum. The effect of this phasing on the energy range reached by the resonant ions and the type of orbits are described next.

5.2.1 Fast ion distribution function calculations

The interfacing of the codes composing the SCENIC package aims at solving iteratively the equilibrium state, the wave deposition, and the ^{3}He ion distribution function, until a self-consistent converged solution is obtained. The MHD equilibrium and the dielectric tensor calculations require some knowledge of the moments of the resonant ion distribution function. The heated ion distribution function usually develops a fast tail and therefore cannot be entirely modelled as a Maxwellian distribution. As described in more detail in Ref. [53], the resonant ion distribution function is split into thermal and fast components, which are respectively fitted onto a Maxwellian and a bi-Maxwellian model [44]. In the simulations
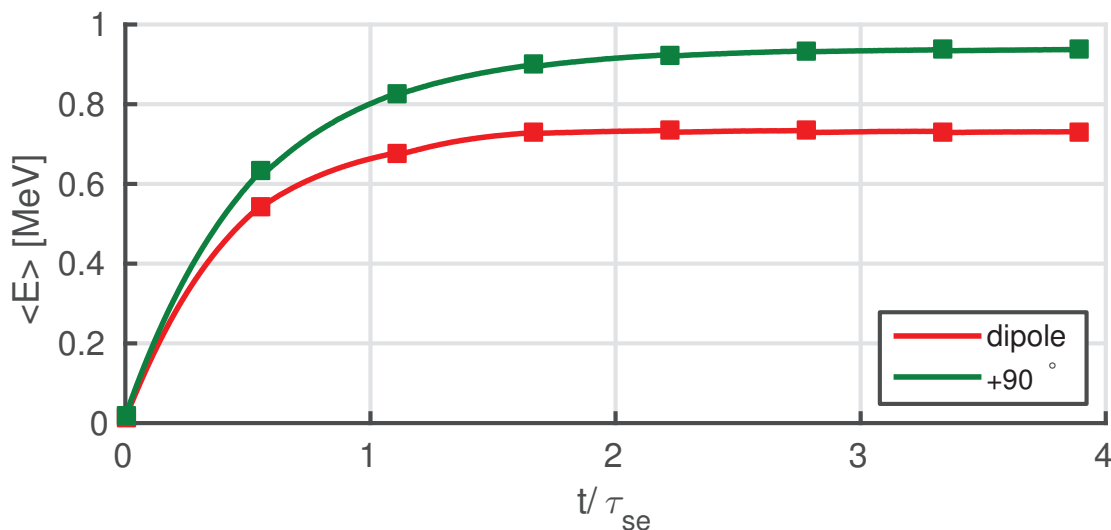
Figure 5.4: Mean energy per particle as a function of time normalised to the slowing down time on electrons $\tau_{se} = 0.18\,\text{s}$.

presented here, the fast ion tail represents the most significant part of the marker distribution. The thermal part is mainly comprised of particles that were numerically re-injected in the plasma in a thermal state after having crossed the last closed flux surface. Considering the fraction and the energy range of the fast ions, it is assumed that only the fast component of the distribution significantly affects the plasma equilibrium and dielectric tensor. Therefore, only this component has been taken into account in the iteration scheme. Saturated solutions have been obtained for the antenna phasings most relevant for typical JET ICRF scenarios: dipole ($n_\varphi = \pm27$) and +90° (co-current travelling wave: $n_\varphi = -13$). Figure 5.4 shows that the mean energy per ^{3}He particle saturates with time for each phasing after a few iterations, indicating a converged self-consistent distribution function is obtained. The converged ^{3}He distribution functions for the two antenna phasings obtained with SCENIC for 3 MW of ICRF power are shown in Fig. 5.5. It is seen that fast ions in the MeV range are generated in both cases. The distribution function of a typical minority heating (MH) scenario (deuterium rich plasma with 5% hydrogen minority) with the same equilibrium profiles and input power conditions is shown for comparison. The significant potential of generating fast ions with moderate ICRF power clearly appears.
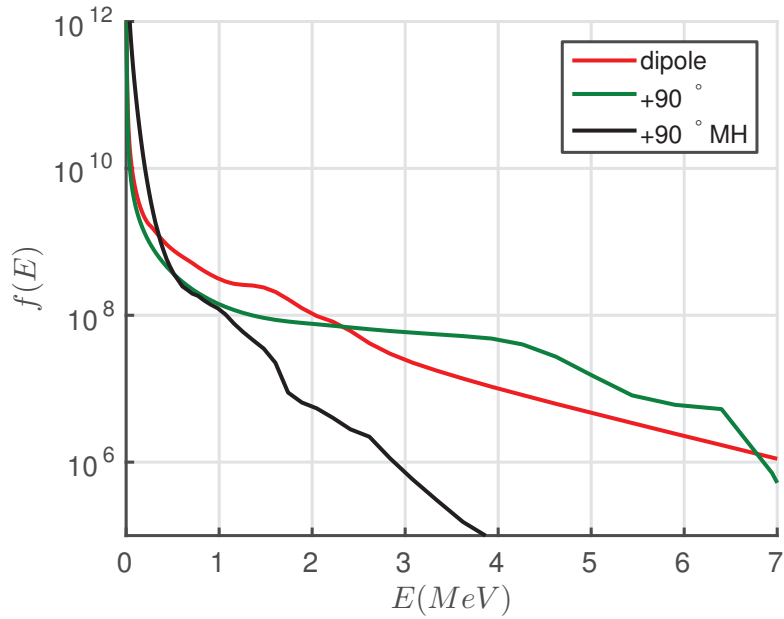
Figure 5.5: Saturated energy distribution functions of ^{3}He ions for dipole and +90° phasings using three-ion species scheme, and +90° phasing using a minority scheme in JET.
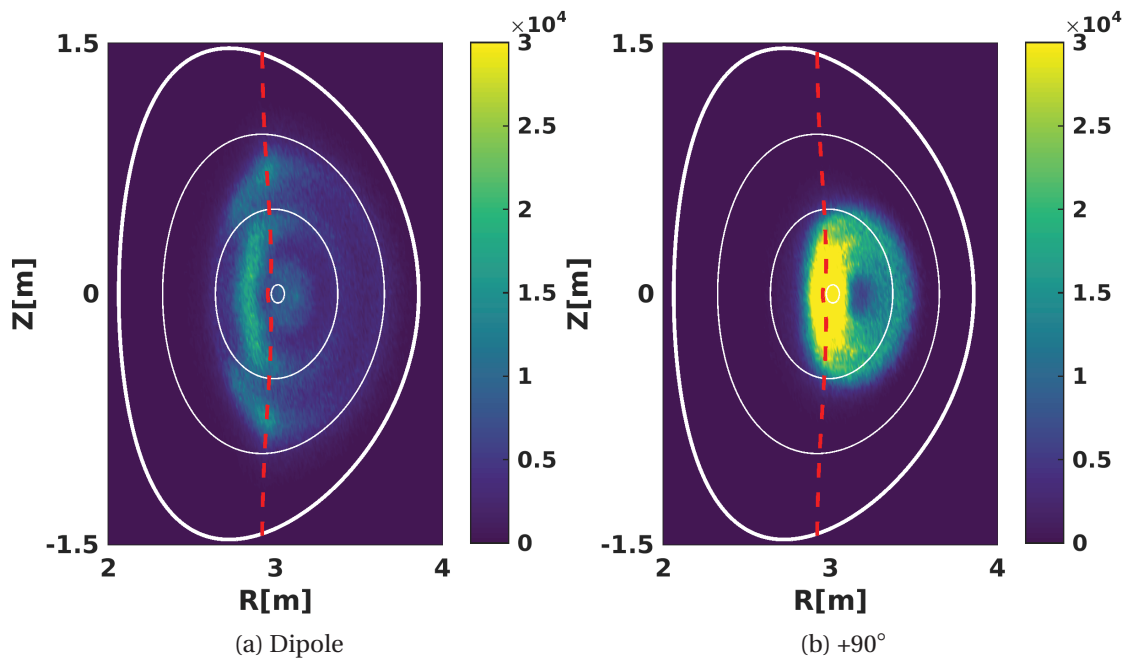

(a) Dipole

(b) +90°

Figure 5.6: Fast ion pressure profiles (Pa) for each investigated antenna phasing in JET. The red dashed line represents the unshifted resonance position for ^{3}He ions.

5.2.2 RF-pinch effect

It is seen from Figs. 5.4 and 5.5 that using $+90°$ phasing allows the generation of a larger fast ion tail than for dipole phasing. This can be explained mainly by two arguments. Firstly, the $+90°$ phased wave features a lower $|k_\parallel|$ value (which can be approximated by $|n_\varphi|/R$) than the dipole phased wave. Therefore the absorption layer width is smaller in the $+90°$ phasing case and consequently contains a higher power density than in the dipole case. Secondly, one has to consider the inward radial transport of resonant ions interacting with a co-current travelling ICRF wave. It was shown in Ref. [58] that RF wave-particle interaction not only result in kicks in the resonant particles' energy ΔE but also in the toroidal momentum $P_\varphi = -q\psi + mv_\parallel B_\varphi/B$ which reads:

$$\Delta P_\varphi = \frac{n_\varphi}{\omega}\Delta E \tag{5.2}$$

In eq. 5.2 ω is the RF wave frequency. In the VENUS-LEVIS code [19] which solves for the fast ion distribution function, the wave-particle interaction is resolved by Monte-Carlo operators that acts on the particles parallel and perpendicular velocities [53]. The kick in the parallel velocity reproduces the change in the toroidal momentum approximated by eq. 5.2. The magnetic moment of resonant particles is also affected by the interaction, such that on average resonant particles become trapped and their bounce tips align with the resonance layer. The change in the toroidal momentum subsequently results, on average, in a radial displacement of the trapped particles bounce tips along the resonance layer. It is seen from eq. 5.2, and the definition of P_φ, that co-current (resp. counter-counter) travelling waves induce an inward (outward) RF-pinch. The energy range reached by the fast ions (observable in Fig. 5.5) suggests a strong RF-pinch effect. As seen in Fig. 5.6, $+90°$ phasing produces strong on-axis peaking of the fast ion pressure, while dipole phasing spreads the fast ion pressure vertically along the resonance layer. In both cases, the pressure profile gives an insight into the classes of orbits that the resonant particles comprise. This can be addressed more precisely by collectively examining the resonant particles toroidal momentum P_φ and the pitch angle variable $\Lambda = \frac{\mu}{E}B_0$ (here Λ can be seen as a measure of a particles bounce tip position with respect to the on-axis magnetic field). In Refs. [110] and [20] these variables are used in order to draw a classification of guiding centre orbit types. Fig. 5.7 shows how the resonant particles are distributed in the $\Lambda - P_\varphi$ plane. The ICRF-induced particle trapping, and the resulting alignment of the particle bounce tips with the resonant layer causes the concentration of particles around the $\Lambda = 1$ line. It is seen in Fig. 5.7b that $+90°$ phasing pushes the particles to the left-hand side of the $\Lambda - P_\varphi$ plane bringing the particles bounce tips closer to the magnetic axis. A significant fraction of the resonant particles are then able to escape the trapped region and enter the barely passing region of phase space. These highly energetic particles are consequently well confined in the plasma. It is seen that for the dipole phasing simulation, more regions of the $\Lambda - P_\varphi$ diagram are populated. This can be explained by the fact that the wave-particle interaction with a dipole phased antenna is modelled by including two wave fields with a positive ($n_\varphi = 27$) and a negative mode number ($n_\varphi = -27$) carrying the same fraction of ICRF power. This wave modelling technique, described in Ref. [63], is made possible by the absence of coupling

between the wave toroidal mode numbers in axisymmetric configurations. The $n_\varphi = -27$ component acts in a similar way as the +90° phased wave, i.e. it induces an inward RF-pinch to particles, and thus is responsible for the population of barely passing particles seen in Fig. 5.7a. On the other hand, the $n_\varphi = 27$ component induces an outward RF-pinch of particles which causes an increase in the trapped particle population. In addition, this pinch effect tends to push resonant particles towards the right-hand side of the $\Lambda - P_\varphi$ plane causing the generation of trapped particles with large orbit width. These orbits potentially cross the last closed surface resulting in a higher particle loss rate compared to the +90° case. This combined effect of RF-pinch and finite orbit width on the distribution function in phase-space, and in particular on the lost fraction, shows the importance of accounting for finite orbit width in simulations of the three-ion species scheme. Simulations with a -90° phased wave, corresponding to $n_\varphi = 13$ were also conducted. However the significant particle loss rate produced by the outward RF pinch and the large orbit width brought difficulties in the convergence of the distribution function.

(a) Dipole   (b) +90°
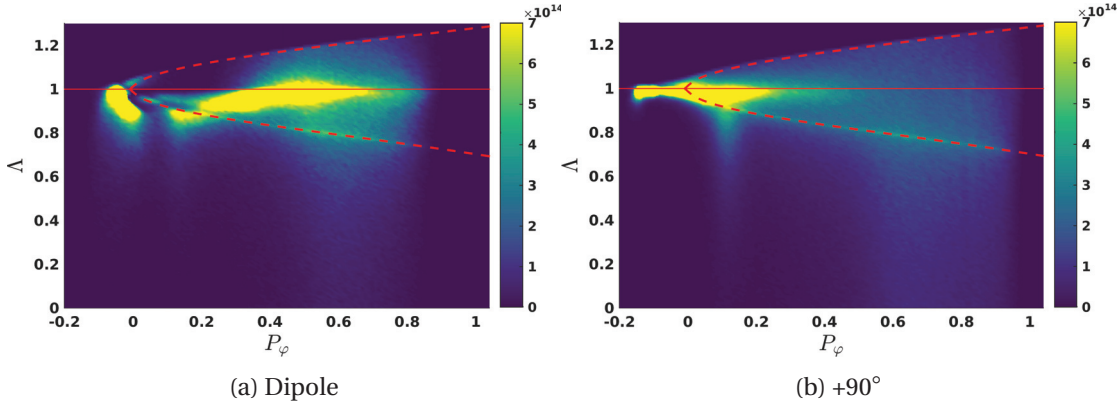
Figure 5.7: Distribution (#) of resonant ^{3}He particles in $\Lambda - P_\varphi$ plane. Note that P_φ has been normalised for plotting convenience (q is the particles charge and ψ_0 is the poloidal flux on axis). The dashed and solid lines highlight respectively the trapped-passing boundary and the $\Lambda = 1$ position.

5.2.3   Collisional power transfer

The guiding centre orbit following code VENUS-LEVIS [19] includes the Coulomb interactions between the fast ions and the background electrons and ions. The interaction time between the ^{3}He markers and the background species computed by VENUS-LEVIS relies on the derivation of the associated Monte Carlo operator based on Ref. [55]. Figure 5.8 shows the energy dependency of the interaction time between ^{3}He ions and background electrons, hydrogen and deuterium ions. It was seen in the previous section that the energy of the simulated ^{3}He ions are mostly above 1 MeV. In that energy range, slowing down on electrons is the dominant Coulomb interaction. In comparison, the pitch angle scattering process on background species is around two orders of magnitude slower. This also suggests that the fast ion tail of the

distribution functions is highly anisotropic. Moreover, and as expected, Figure 5.9 indicates that most of the collisional power resulting from slowing down interactions is transferred to background electrons. The collisional power deposition profile (Fig. 5.9) and the ICRF power deposition profile (Fig. 5.10) are noticeably affected by the RF-pinch effect on fast ions. It is seen that the ICRF power, and consequently the collisional power density transferred to electrons, are strongly peaked on axis for +90° phasing compared to the dipole case. Figure 5.9 already suggests that the dipole scheme can be used in tokamak plasma experiments to peak the central electron temperature. The fast ion simulations presented here could be coupled to transport calculations in order to estimate more quantitatively the impact of this scenario on the background thermal profiles. The peaking of the electron temperature profile can be beneficial for instance for enhancing the transport of impurities, such as Tungsten, out of the plasma core [111].
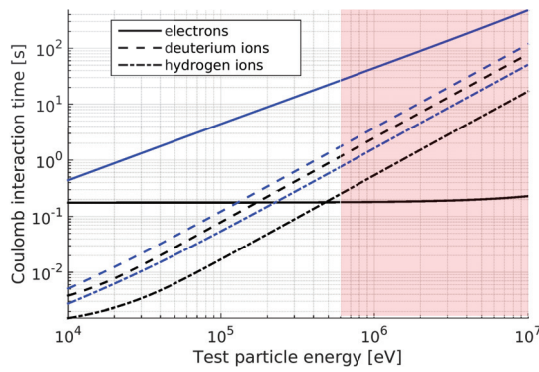
Figure 5.8: Interaction time for slowing down (black lines) and pitch angle (blue lines) scattering of ^{3}He ions on background species.
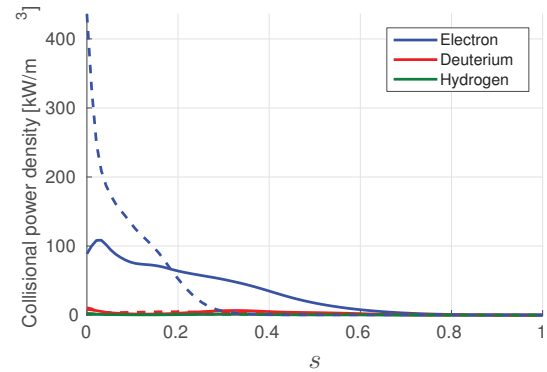
Figure 5.9: Density of collisional power on each species. Dashed lines: +90° phasing; solid lines: dipole phasing.

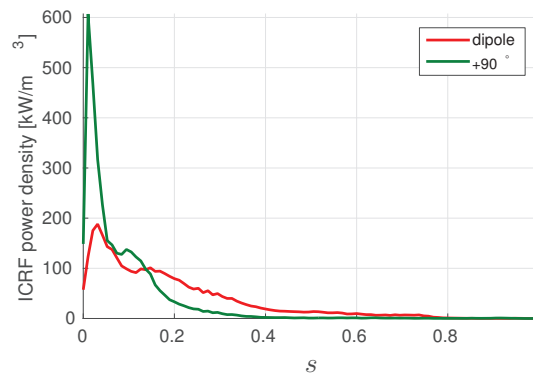Figure 5.10: Density of ICRF power on the ^{3}He ions for each investigated antenna phasing.
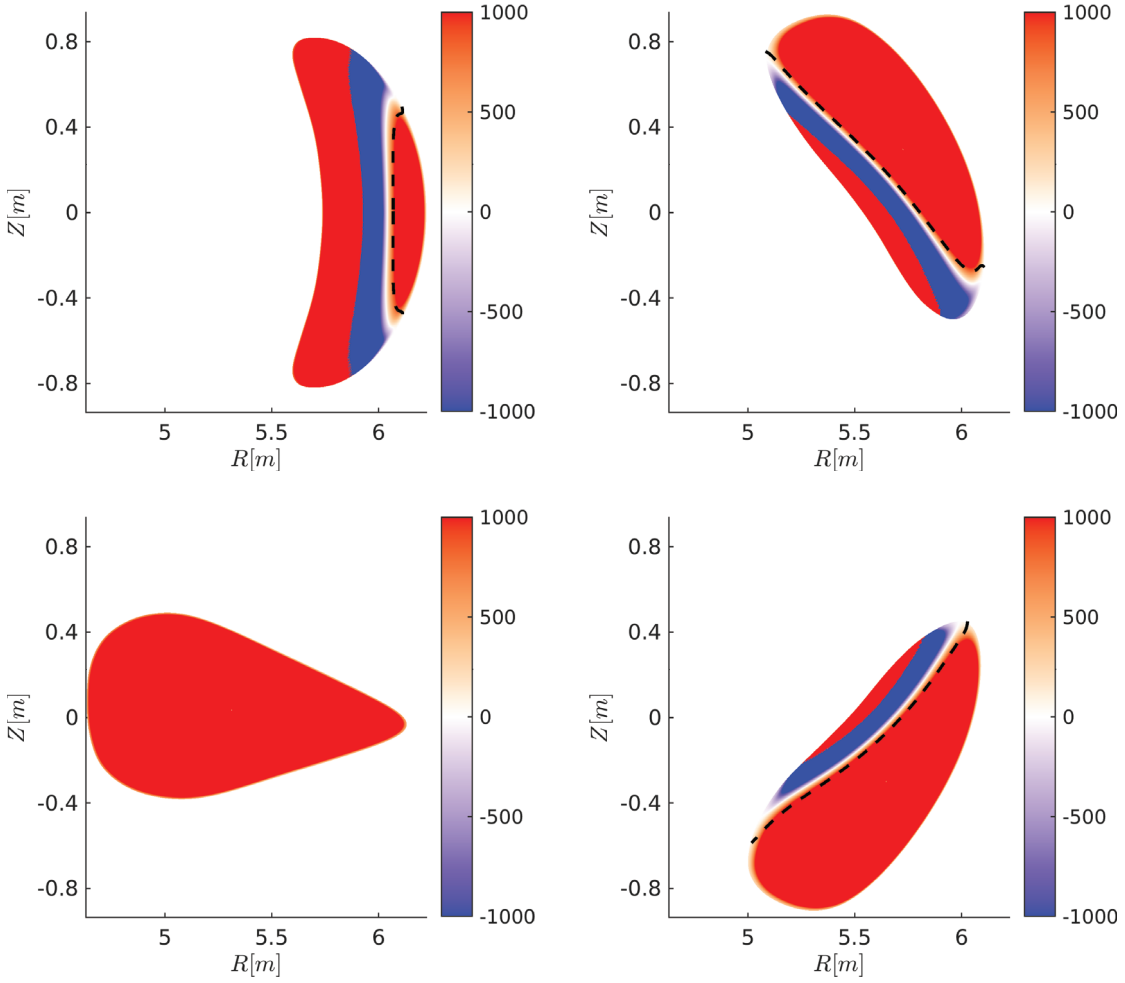
Figure 5.11: Dispersion relation ($n_\perp^2$ given by eq. 5.1 obtained with the three-ion species applied to W7-X

5.3   Three-dimensional modelling: Wendelstein 7-X plasma

As previously mentioned, it was shown in Ref. [112] that minority heating scenarios may not be suitable for generating a large fast ion population mainly because of the high collisionality which prevents tail formation. In this section, the SCENIC code package is applied to a W7-X configuration in order to assess the possibility to use the three-ion species scheme as an alternative to minority heating. A high-mirror magnetic equilibrium is considered with the following density and temperature profiles expressed in terms of normalised toroidal flux s: $n_e = 1.5 \times 10^{20} \left(0.9 \times (1 - s^{10})^2 + 0.1 \right)$ [m^{-3}] and $T_e = 4 \times 10^3 (1 - s)$ [eV]. These profiles ensure that $\langle \beta \rangle \simeq 4\%$ which is necessary to achieve a quasi-omnigeneous equilibrium and consequently good fast particle confinement.

As suggested in Refs. [109, 112], a radial electric field arising from an ion-root regime [96] is included in the following calculations in order to assist the confinement of the heated ions. A

favourable plasma mix for the three-ion species scheme has been identified [41] as $[H] = 68\%$, $[D] = 31.8\%$, $[^3He] = 0.1\%$. The corresponding dispersion relation is given in Fig. 5.11 and shows that, as required by the scheme, the L-cutoff is in the vicinity of the ^{3}He resonance position. This three-ion pecies scenario will be compared with a minority heating scheme that uses the same thermal profiles and MHD equilibrium. Previous [112] SCENIC calculations of minority heating in a D-rich W7-X plasma featured H minority with $[H] = 0.5\%$. However, lowering $[H]$ for increasing the efficiency of fast-ion generation is restricted by degeneracy between the resonance frequency for H minority and second harmonic D majority ions: $\omega_{cH} = 2\omega_{cD}$. In fact, in high-density plasmas of W7-X most of the RF power is absorbed by D majority ions instead of H minority ions, reducing further the potential of this scenario for fast-ion studies. In contrast, using 3He as a minority (as it is done in the following minority scheme) has an advantage of avoiding the degeneracy with the harmonic resonance for majority ions. Minority heating of ^{3}He in H or ^{4}He plasmas cannot be made effective at arbitrarily low ^{3}He concentrations. The efficiency of the single-pass plasma absorption strongly depends on the 3He concentration. TOMCAT modelling suggests that the single-pass damping by ions is maximised at $[^3He] \simeq 2\%$.

Figure 5.12a compares the energy distribution functions obtained for both scenarios. No clear fast ion tail comparable to what is usually observed in tokamak calculations appears in either of these scenarios. As a consequence, the contribution from the fast ion to the ideal MHD equilibrium and the wave propagation could not clearly be assessed and the usual iterative procedure of the SCENIC package could not be applied in the calculations presented in this section. It is nevertheless seen that the three-ion species scheme produces a fast ion tail which reaches energy range above 100 keV. In contrast, the minority heating distribution function is mostly thermal and the fast ion tail $(50 - 100\text{keV})$ is nearly non-existent. Precisely, the number of particles above 50 keV obtained with the minority heating scenario reaches 3.36×10^{14}, whereas 6.40×10^{15} particles are recorded in this range for the three-ion species scheme. Particle orbits with energy below 50 keV are largely affected by the $\boldsymbol{E} \times \boldsymbol{B}$ drift arising from the inclusion of the radial electric field. Therefore diffusion of thermal particles is the main loss channel in this case. Figure 5.12b shows the energy distribution of the recorded lost particles in the case where the three-ion species scheme is applied. It is seen that the energy range of lost particles is well above thermal energy. This suggests that the resonant particles are sufficiently accelerated such that their kinetic energy becomes large enough to overcome confinement. As a final remark, even if these calculations show indications that the three-ion species is more suitable than minority heating scenarios for the task of generating fast ions in W7-X, it is emphasised that the fast ions of the confined distribution still represent, in both cases, a small fraction of the total distribution function. It seems that for the case of W7-X the typical thermal profiles, and the three-dimensional structure of the equilibrium significantly influence the tail formation process and consequently the heated ion distribution function in velocity space. More detailed analysis and conclusions on these aspects will be given in future work.
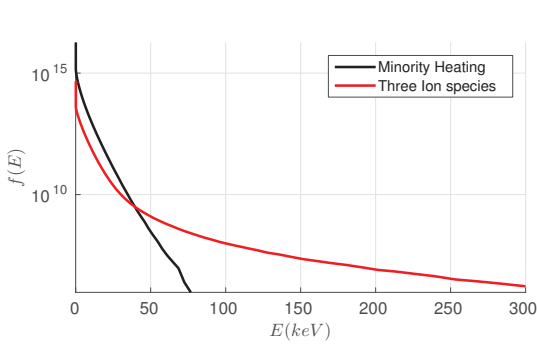
(a) Comparison of the ^{3}He ions distribution functions obtained with the minority heating and three-ion species schemes in W7-X.
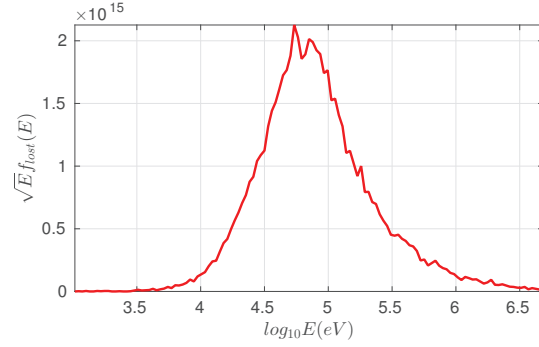
(b) Lost particle energy distribution function obtained with the three-ion species scheme in W7-X.

5.4 Summary and conclusions

The work presented here shows modelling of the three-ion species scheme that was first introduced in [41]. Two- and three-dimensional plasma equilibria were considered in order to asses the potential of the three-ion species scheme in JET and W7-X plasmas. The SCENIC code package has been used and its suitability for the modelling of this scheme has been successfully demonstrated. It was shown that in a JET-like plasma, fast ions easily reach the MeV range of energy. As expected, varying the antenna phasing changes the direction of the RF induced particle pinch. This effect is even more pronounced for the low ^{3}He concentration used in this scheme, implying large energy transfer during the resonant wave-particle interaction. It was seen that for co-current travelling ICRF waves is employed, the inward pinch causes the orbits of resonant trapped ions to typically convert into passing orbits (which are better confined). Consequently the establishment of the fast ion tail is assisted by the pinching of the fast ions towards the magnetic axis where the collisionality is lower and the wave absorption is higher. Estimation of the collisional power distribution indicates that co-travelling wave schemes may be used for the peaking of electron temperature profile (via localisation of the heated particules and Coulomb energy transfer) and may consequently help to increase the outward impurity transport. On the other hand using a dipole phased wave applies in addition an outward pinch to resonant particles. Such a finite orbit effect can cause the loss of resonant particles as they receive energy from the wave. The outward drift and the high loss rate reduce the mean energy of the resonant ion distribution and also causes the collisional power on the background species to be deposited in non-central plasma regions. Overall the fast ion distribution generated for both considered phasings show a more significant potential for fast ion generation than a typical minority heating scheme. SCENIC simulations indicate that the three-ion species scheme in W7-X high mirror plasma would be more appropriate than a minority heating scheme for the generation of fast ions in this stellarator.

6 Summary and outlook

6.1 Summary

The numerical resolution of an auxiliary generated fast ion population in two- and three-dimensional configurations has been addressed. The `SCENIC` code package is a flexible tool for solving self-consistently the MHD equilibrium, the ICRF wave propagation and the fast ion distribution. In this section we shall summarise the main results found in the previous chapters.

The physical concepts necessary for the description the `SCENIC` code package and the understanding of the results obtained throughout this thesis were explained in chapter 1.4. This was followed by chapter 2.4 where `SCENIC` was used for the study of ICRF minority heating scenario in an axisymmetric JET tokamak plasma. It was seen that the toroidal symmetry of the configuration greatly simplifies the modelling of the ICRF antenna excitation. The absence of coupling between the waves toroidal modes allows the simulation of each of these modes separately. In practice one can only consider the modes that dominate the power spectrum. Full `SCENIC` simulations were performed with various antenna phasings (+90°, −90° and dipole). The converged ICRF distribution functions were passed on to the `HAGIS` code in order to study the stability of the $m = n = 1$ internal kink mode. `SCENIC` and `HAGIS` calculations showed that the shear mechanism usually invoked could not explain the sawteeth triggering observed in the dedicated JET experiments. These numerical results indicate that the asymmetry in the fast ion distribution function is more likely to be responsible for the destabilisation of the internal kink mode and consequently of the shortening of the sawteeth period.

The loss channels acting on fast particles in the Wendelstein 7-X stellarator were explained in chapter 3.6. Low collisional and transitioning particles are expected to experience stochastic radial diffusion. As we mainly focused on NBI-like ion populations with moderate energy, and the generation of fast ions with ICRF heating from a thermal population, this loss channel does not play a significant role in the presented work. The drift induced losses caused by the magnetic fields three-dimensional structure, i.e. the combined effect of negative geodesic

curvature and magnetic field amplitude oscillations, is seen to be the main channel of particle losses. Coulomb collisions are found to enhance this mechanism via pitch-angle scattering. The application of ICRF heating increases also the particle losses because the trapped fraction is enhanced. These ICRF induced losses can be decreased when the resonance position is displaced so that it is predominantly located towards the bean-shaped cross-section of the equilibrium. In such a configuration, the fraction of localised particles, i.e. trapped between the main mirrors, is decreased. It was also seen that the inclusion of a radial electric field, which restores the ambipolar diffusion of background electrons and ions, reduces significantly the particle losses observed in ICRF and NBI simulations. It is important to keep in mind that the induced $E \times B$ drift will affect the trajectory of fast particles up to a certain energy level. Indeed the amplitude of this drift does not depend on the particles energy contrary to the ∇B and curvature drifts. It is therefore crucial to include such an effect in a numerical investigation into the generation of fast ions from an initially thermal population in W7-X. However an important point to note is that α particles in a reactor sized Helias stellarator are not expected to be affected by this radial electric field. Finally the high plasma density required to obtain a quasi-isodynamic equilibrium is a major hindrance to the high energy tail formation. In the simulations presented here, no significant fast ion population was observed with a minority heating scheme.

The newly developed three-ion species ICRF scheme was simulated for the first time with SCENIC and the results were presented in chapter 4.6. It was verified that the LEMan code is able to retrieve the key features of this scheme. The three-ion species scenario was tested in a JET-like tokamak plasma. It was found that MeV ions are easily produced with +90° and dipole phasings. The RF induced particle pinch is particularly strong due to high energy wave-particle interaction. The inward pinch caused by the +90° phased wave tends to convert the energetic resonant particles from trapped to passing. The confinement of energetic particles is seen to be enhanced in this case. The application to a W7-X plasma showed that the three-ion species produces more fast ions than a typical minority heating scheme. Though it is stated that a three-ion species scheme should be considered in the experimental campaign, the high energy ions produced suffer from enhanced losses due to the weakening effect of the $E \times B$ drift, and the fact that W7-X is not perfectly optimised.

6.2   Outlook

As described at the beginning of this thesis and illustrated in the previous chapters, the SCENIC code package is composed of three main numerical codes. Each of these codes deals with different aspects of plasma physics (MHD equilibrium, ICRF wave propagation, fast particle motion) that SCENIC interconnects. Therefore, developments and benchmarking of various kinds can easily be foreseen for the near future.

The ANIMEC code offers the possibility of calculating free-boundary equilibria. This feature would become particulary interesting for the investigation of the effects of ICRF heating on

the last closed flux surface (LCFS). Indeed, the ICRF heat deposition can in some cases be strongly localised in the vicinity of the LCFS, e.g. ICRF minority heating in a high-mirror W7-X configuration. A significant increase of the fast ion pressure is to be expected in these regions and consequently some modification of the local MHD equilibrium. However if such calculations were to be performed with the full `SCENIC` iteration procedure, particular care should be taken regarding the mapping of the markers position in the curvilinear coordinate system.

As seen in section 4.5.1 concerning the ICRF modelling in W7-X configurations, the spatial localisation of the antenna breaks the periodicity of the machine in terms of wave deposition. In addition to the consequences of this on plasma heating in general, the improvements to the ICRF model taking into account such toroidal variation, e.g. in the equilibrium and the dielectric tensor via a modification to the bi-Maxwellian function (eq. 2.44), should be considered in the future.

In the particle losses study presented in chapter 3.6, particles crossing the LCFS were considered as lost and no re-entry calculation was performed. This limitation is inherent to the flux coordinate system in which the `SCENIC` package is written. Some preparatory work is in progress in order to extend the simulated volume in the vacuum region and up to the first wall. Such an extension will allow the calculation of heat deposition by fast particle losses on plasma-facing components. In addition, some particles crossing the LCFS will then be able to re-enter the plasma in a realistic manner. These calculations is an important feature of the `ASCOT` code and comparitive studies would be very useful for the validation of the `SCENIC` implementation. Moreover, the antenna model in the `LEMan` code could then be placed in the vacuum region and no longer within an edge region of the plasma as it is currently done. In that case, as the vacuum region is evanescent for the fast wave, it will be possible to model the tunnelling of the fast wave from the antenna into the plasma.

Such simulations could be also coupled to transport calculation modules in order to estimate the self-consistent radial electric field in ICRF heated W7-X plasmas.

Recent comparisons with similar wave codes indicate that the `LEMan` code strongly underestimates the ICRF wave absorption by electrons. This is typically observed in a minority heating scheme with very low concentration ($\leq 1\%$) where electron damping computed by wave codes such `TOMCAT` or `TORIC` dominates over minority damping. This can be partly explained by the fact that `LEMan` only includes electron Landau and ion cyclotron damping in the power deposition calculations. Inclusion of Transit Time Magnetic Pumping (TTMP) effects may help to resolve discrepancies in the absorbed power calculations. A benchmark exercise with other wave codes will therefore be necessary in order to validate the correct implementation of TTMP damping in `LEMan` .

The dielectric tensor implementation in `LEMan` is also being revised in order to take into account higher cyclotron harmonic damping. Such an extension will allow the modelling of e.g. second harmonic majority plasma heating. This kind of important code upgrade will also

require significant benchmarking.

A benchmark effort against the SELFO was initiated after the first implementation of the ICRF Monte Carlo operator. This comparitive study must be extended in particular to include relevant boundary conditions to the quasi-linear diffusion coefficient implemented in SELFO as described in Ref. [57].

Peculiar features of the minority ions energy distribution function were seen during the modelling of ICRF scenarios where the power absorbed is particularly high (minority heating with low concentration ($\simeq 1\%$) and high power ($\simeq 12\,\mathrm{MW}$), and three-ion species scheme in tokamak plasma). Indeed, secondary fast ion tails are observed and display a bump-on-tail feature in the energy distribution. These kinds of numerical results indicate that the quasi-linear theory from which the ICRF Monte Carlo operator is derived, is no longer valid for the considered scenario. Proper investigation on the limit of validity of the quasi-linear model should be performed. Development of adequate modelling of ICRF scenarios for which the quasi-linear is not applicable, is therefore required. Two possible modelling methods are foreseen:

1. One could exploit the capacity of VENUS-LEVIS to resolve the full-orbit motion of fast ions and include directly in the corresponding equation of motions the RF wave electric field. This task may be hindered by numerical issues since full-orbit resolution calculations are not as numerically efficient in Boozer coordinates as in ANIMEC coordinates. In the case where the numerical precision in Boozer coordinates cannot be improved, full-orbit simulations should be run in ANIMEC coordinates. This would require the projection of the RF wave field from Boozer to ANIMEC coordinates. Here again, some numerical precision issues may be expected.

2. A novel implementation for the resolution of the ICRF wave-particle interaction was proposed in Ref. [113]. A so-called $5^{1/2}$-D model gives, in addition to the time evolution of the guiding centre coordinates ($\boldsymbol{X}_{gc}, \rho_{\parallel}$), equations for the time evolution of the resonant particles magnetic moment and the phase difference between the particles gyro-phase and the RF wave electric field phase. This model requires the expansion of the guiding centre drift equation to the second order in Larmor radius. Conveniently, second order corrections were recently implemented in the VENUS-LEVIS code [114].

The development of scenarios for auxiliary generation of fast ions in the W7-X stellarator should be continued. The three-ion species scheme was shown in chapter 4.6 to be a very promising tool to generate a large fast ion tail in such high density plasmas. Investigations of this scenario in W7-X configurations should be pursued. In addition, it would be worth exploring the possibility of generating fast ion via RF beam acceleration. This scenario could be first modelled in an axisymmetric plasma for validation. The full SCENIC iterative process could be applied since the beam population can be well approximated by the bi-Maxwellian as soon as slowing down and RF absorption are established.

In addition to the study of fast ion generation scenarios, it is important to characterise in detail the tail formation process in W7-X. Indeed, it appears that the tail formation process in W7-X is not only hindered by the high plasma density but also fundamentally affected by the three-dimensionnal nature of the equilibrium, i.e. the inherent wave propagation issues and particle loss channels. Techniques enhancing the formation of significant fast ion tails in W7-X should be further investigated.

Acknowledgements

Bibliographie

[1] Francis F. Chen. *Introduction to Plasma Physics and Controlled Fusion.* Springer US, 1984. (Cited on pages 1 and 14.)

[2] J D Lawson. Some criteria for a power producing thermonuclear reactor. *Proceedings of the Physical Society. Section B*, 70(1) :6, 1957. (Cited on page 2.)

[3] H. Grad and H. Rubin. Hydromagnetic equilibria and force-free fields. *Proceedings of the 2nd UN Conf. on the Peaceful Uses of Atomic Energy, Geneva : IAEA*, 31 :190, 1958. (Cited on page 11.)

[4] V.D. Shafranov. Plasma equilibrium in a magnetic field. *Reviews of Plasma Physics, New York : Consultants Bureau*, 2 :103, 1966. (Cited on page 11.)

[5] D.P. O'Brien, L.L. Lao, E.R. Solano, M. Garribba, T.S. Taylor, J.G. Cordey, and J.J. Ellis. Equilibrium analysis of iron core tokamaks using a full domain method. *Nuclear Fusion*, 32(8) :1351, 1992. (Cited on pages 11 and 48.)

[6] M. Brix, N. C. Hawkes, A. Boboc, V. Drozdov, S. E. Sharapov, and JET-EFDA Contributors. Accuracy of efit equilibrium reconstruction with internal diagnostic information at jeta). *Review of Scientific Instruments*, 79(10), 2008. (Cited on pages 11 and 48.)

[7] H. Lütjens, A. Bondeson, and O. Sauter. The chease code for toroidal mhd equilibria. *Computer Physics Communications*, 97(3) :219 – 260, 1996. (Cited on page 11.)

[8] A. Reiman and H. Greenside. Calculation of three-dimensional {MHD} equilibria with islands and stochastic regions. *Computer Physics Communications*, 43(1) :157 – 167, 1986. (Cited on page 12.)

[9] S. R. Hudson, R. L. Dewar, G. Dennis, M. J. Hole, M. McGann, G. von Nessi, and S. Lazerson. Computation of multi-region relaxed magnetohydrodynamic equilibria. *Physics of Plasmas*, 19(11), 2012. (Cited on page 12.)

[10] S. P. Hirshman and J. C. Whitson. Steepest-descent moment method for three-dimensional magnetohydrodynamic equilibria. *Phys. Fluids*, 26(12) :3553, 1983. (Cited on pages 12, 30, and 64.)

Bibliographie

[11] W. A. Cooper, S. P. Hirshman, P. Merkel, J. P. Graves, J. Kisslinger, H. F G Wobig, Y. Narushima, S. Okamura, and K. Y. Watanabe. Three-dimensional anisotropic pressure free boundary equilibria. *Comput. Phys. Commun.*, 180(9) :1524–1533, September 2009. (Cited on pages 12, 30, 32, 64, and 92.)

[12] Robert G. Littlejohn. Hamiltonian formulation of guiding center motion. *Physics of Fluids*, 24(9) :1730–1749, 1981. (Cited on pages 15 and 35.)

[13] Robert G. Littlejohn. Variational principles of guiding centre motion. *Journal of Plasma Physics*, 29 :111–125, 2 1983. (Cited on page 16.)

[14] W. D'Haeseleer. *Flux coordinates and magnetic field structure : a guide to a fundamental tool of plasma structure*. Springer series in computational physics. Springer-Verlag, 1991. (Cited on pages 16 and 68.)

[15] J. Carlsson, L.-G. Eriksson, and T. Hellsten. Fido, a code for calculating the velocity distribution function of a toroial plasma during icrh. *Theory of Fusion Plasma (Proc. Joint Varenna-Lausanne Int. Workshop Varenna, 1994)*, page 351, 1998. (Cited on page 16.)

[16] E. Hirvijoki, A. Snicker, T. Korpilo, P. Lauber, E. Poli, M. Schneller, and T. Kurki-Suonio. Alfvén eigenmodes and neoclassical tearing modes for orbit-following implementations. *Computer Physics Communications*, 183(12) :2589 – 2593, 2012. (Cited on page 16.)

[17] G J Kramer, R V Budny, a Bortolon, E D Fredrickson, G Y Fu, W W Heidbrink, R Nazikian, E Valeo, and M a Van Zeeland. A description of the full-particle-orbit-following SPIRAL code for simulating fast-ion experiments in tokamaks. *Plasma Phys. Control. Fusion*, 55(2) :025013, February 2013. (Cited on page 16.)

[18] M. Drevlak. Thermal load on the w7-x vessel from nbi losses. *36th EPS Conf. on Plasma Phys. (Sofia, 26 June-3 July 2009) Europhys. Conf. Abstracts (ECA)*, 33E(ECA) :4.211, 2009. (Cited on page 16.)

[19] D. Pfefferlé, W.A. Cooper, J.P. Graves, and C. Misev. Venus-levis and its spline-fourier interpolation of 3d toroidal magnetic field representation for guiding-centre and full-orbit simulations of charged energetic particles. *Computer Physics Communications*, 185(12) :3127 – 3140, 2014. (Cited on pages 16, 35, 36, 82, 95, and 96.)

[20] L-G Eriksson and F Porcelli. Dynamics of energetic ion orbits in magnetically confined plasmas. *Plasma Phys. Control. Fusion*, 43(4) :R145–R182, 2001. (Cited on pages 18 and 95.)

[21] A Gibson and J B Taylor. Single Particle Motion in Toroidal Stellarator Fields. *Phys. Fluids*, 10(12) :2653–2659, 1967. (Cited on page 18.)

[22] John R. Cary, C. L. Hedrick, and J. S. Tolliver. Orbits in asymmetric toroidal magnetic fields. *Phys. Fluids*, 31(6) :1586, 1988. (Cited on pages 18 and 62.)

[23] C. D. Beidler, Ya. I. Kolesnichenko, V. S. Marchenko, I. N. Sidorenko, and H. Wobig. Stochastic diffusion of energetic ions in optimized stellarators. *Phys. Plasmas*, 8(6) :2731, 2001. (Cited on pages 19, 66, 67, and 88.)

[24] P Helander, C D Beidler, T M Bird, M Drevlak, Y Feng, R Hatzky, F Jenko, R Kleiber, J H E Proll, Yu Turkin, and P Xanthopoulos. Stellarator and tokamak plasmas : a comparison. *Plasma Phys. Control. Fusion*, 54(12) :124009, December 2012. (Cited on pages 22, 64, and 77.)

[25] Roscoe B White. *Theory of tokamak plasmas*. Elsevier, 2013. (Cited on page 23.)

[26] P. Helander and D.J. Sigmar. *Collisional Transport in Magnetized Plasmas*. Cambridge University Press, 2001. (Cited on page 23.)

[27] A. A. Galeev, R. Z. Sagdeev, H. P. Furth, and M. N. Rosenbluth. Plasma diffusion in a toroidal stellarator. *Phys. Rev. Lett.*, 22 :511–514, Mar 1969. (Cited on page 24.)

[28] H.E. Mynick and W.N.G. Hitchon. Effect of the ambipolar potential on stellarator confinement. *Nuclear Fusion*, 23(8) :1053, 1983. (Cited on page 24.)

[29] Darwin D.M. Ho and Russell M. Kulsrud. Neoclassical transport in stellarators. *Physics of Fluids*, 30(2) :442–461, 1987. (Cited on page 24.)

[30] Thomas H. Stix. *Waves in Plasmas*. Springer Science & Business Media, 1992. (Cited on pages 25, 26, and 34.)

[31] J. Vaclavik and K. Appert. Theory of plasma heating by low frequency waves : Magnetic pumping and alfvén resonance heating. *Nuclear Fusion*, 31(10) :1945, 1991. (Cited on page 26.)

[32] T H Stix. Fast-wave heating of a two-component plasma. *Nuclear Fusion*, 737, 1975. (Cited on pages 27, 83, 87, 89, 90, and 91.)

[33] R Koch. Wave–particle interactions in plasmas. *Plasma Phys. Control. Fusion*, 48(12B) :B329–B345, December 2006. (Cited on page 27.)

[34] D.F.H. Start, J. Jacquinot, V. Bergeaud, V.P. Bhatnagar, S.W. Conroy, G.A. Cottrell, S. Clement, G. Ericsson, L.-G. Eriksson, A. Fasoli, V. Fuchs, A. Gondhalekar, C. Gormezano, G. Gorini, G. Grosshoeg, K. Guenther, P.J. Harbour, R.F. Heeter, L.D. Horton, A.C. Howman, H.J. Jäckel, O.N. Jarvis, J. Källne, C.N. Lashmore Davies, K.D. Lawson, C.G. Lowry, M.J. Mantsinen, F.B. Marcus, R.D. Monk, E. Righi, F.G. Rimini, G.J. Sadler, G. Saibene, R. Sartori, B. Schunke, S.E. Sharapov, A.C.C. Sips, M.F. Stamp, M. Tardocchi, and P. van Belle. Bulk ion heating with icrh in jet dt plasmas. *Nuclear Fusion*, 39(3) :321, 1999. (Cited on page 28.)

[35] M. J. Mantsinen, L. G. Eriksson, M. García-Muñoz, R. Bilato, Vl Bobkov, H. U. Fahrbach, J. M. Noterdaeme, and W. Schneider. Analysis of ICRF-accelerated ions in ASDEX upgrade. *AIP Conf. Proc.*, 933 :99–102, 2007. (Cited on page 28.)

[36] T. Mutoh, R. Kumazawa, T. Seki, T. Watari, K. Saito, Y. Torii, D. A. Hartmann, Y. Zhao, M. Sasao, M. Isobe, M. Osakabe, A. V. Krasilnikov, T. Ozaki, K. Narihara, Y. Nagayama, S. Inagaki, F. Shimpo, G. Nomura, M. Yokota, K. Akaishi, N. Ashikawa, P. de Vries, M. Emoto, H. Funaba, A. Fukuyama, M. Goto, K. Ida, H. Idei, K. Ikeda, N. Inoue, K. Itoh, O. Kaneko, K. Kawahata, S. Kado, A. Komori, T. Kobuchi, S. Kubo, S. Masuzaki, T. Morisaki, S. Morita, J. Miyazawa, S. Murakami, T. Minami, S. Muto, Y. Nakamura, H. Nakanishi, N. Noda, K. Nishimura, K. Ohkubo, N. Ohyabu, S. Ohdachi, Y. Oka, H. Okada, B. J. Peterson, A. Sagara, K. Sato, S. Sakakibara, R. Sakamoto, H. Sasao, M. Sato, T. Shimozuma, M. Shoji, S. Sudo, H. Suzuki, Y. Takeiri, K. Tanaka, K. Toi, T. Tokuzawa, K. Tsumori, K. Y. Watanabe, T. Watanabe, H. Yamada, I. Yamada, S. Yamaguchi, K. Yamazaki, M. Yokoyama, Y. Yoshimura, Y. Hamada, O. Motojima, and M. Fujiwara. Ion heating and high-energy-particle production by ion-cyclotron heating in the large helical device. *Phys. Rev. Lett.*, 85 :4530–4533, Nov 2000. (Cited on page 28.)

[37] S Murakami, a Fukuyama, T Akutsu, N Nakajima, V Chan, M Choi, S.C Chiu, L Lao, V Kasilov, T Mutoh, R Kumazawa, T Seki, K Saito, T Watari, M Isobe, T Saida, M Osakabe, M Sasao, and Lhd Experimental Group. A global simulation study of ICRF heating in the LHD. *Nucl. Fusion*, 46(7) :S425–S432, July 2006. (Cited on pages 28 and 36.)

[38] J. Jacquinot, V.P. Bhatnagar, J.G. Cordey, L.D. Horton, D.F.H. Start, R. Barnsley, P. Breger, J.P. Christiansen, S. Clement, S.J. Davies, J.K. Ehrenberg, L.-G. Eriksson, G.M. Fishpool, M. Gadeberg, P.J. Harbour, H.J. Jäckel, K. Lawson, J. Lingertat, C.G. Lowry, C.F. Maggi, G.F. Matthews, R.D. Monk, D.P. O'Brien, E. Righi, G. Saibene, R. Sartori, B. Schunke, A.C.C. Sips, M.F. Stamp, D. Stork, J.D. Strachan, A. Tanga, K. Thomsen, and JET Team. Overview of iter physics deuterium-tritium experiments in jet. *Nuclear Fusion*, 39(2) :235, 1999. (Cited on page 28.)

[39] M.J. Mantsinen, M.-L. Mayoral, D. Van Eester, B. Alper, R. Barnsley, P. Beaumont, J. Bucalossi, I. Coffey, S. Conroy, M. de Baar, P. de Vries, K. Erents, A. Figueiredo, A. Gondhalekar, C. Gowers, T. Hellsten, E. Joffrin, V. Kiptily, P.U. Lamalle, K. Lawson, A. Lyssoivan, J. Mailloux, P. Mantica, F. Meo, F. Milani, I. Monakhov, A. Murari, F. Nguyen, J.-M. Noterdaeme, J. Ongena, Yu. Petrov, E. Rachlew, V. Riccardo, E. Righi, F. Rimini, M. Stamp, A.A. Tuccillo, K.-D. Zastrow, M. Zerbini, and JET EFDA contributors. Localized bulk electron heating with icrf mode conversion in the jet tokamak. *Nuclear Fusion*, 44(1) :33, 2004. (Cited on page 28.)

[40] M.-L. Mayoral, P. U. Lamalle, D. Van Eester, P. Beaumont, E. De La Luna, P. De Vries, C. Gowers, R. Felton, J. Harling, V. Kiptily, K. Lawson, M. Laxåback, E. Lerche, P. Lomas, M. J. Mantsinen, F. Meo, J.-M. Noterdaeme, I. Nunes, G. Piazza, M. Santala, and JET-EFDA Contributors. Icrf heating for the non-activated phase of iter : From inverted minority to mode conversion regime. *AIP Conference Proceedings*, 787(1) :122–129, 2005. (Cited on page 28.)

[41] Ye.O. Kazakov, D. Van Eester, R. Dumont, and J. Ongena. On resonant ICRF absorption in three-ion component plasmas : a new promising tool for fast ion generation. *Nucl. Fusion*, 55 :032001, 2015. (Cited on pages 28, 83, 89, 90, 91, 99, and 100.)

[42] R. O. Dendy, R. J. Hastie, K. G. McClements, and T. J. Martin. A model for ideal m=1 internal kink stabilization by minority ion cyclotron resonant heating. *Physics of Plasmas*, 2(5) :1623–1636, 1995. (Cited on page 29.)

[43] J. P. Graves, K. I. Hopcraft, R. O. Dendy, R. J. Hastie, K. G. McClements, and M. Mantsinen. Sawtooth evolution during jet ion-cyclotron-resonance-heated pulses. *Phys. Rev. Lett.*, 84 :1204–1207, Feb 2000. (Cited on page 29.)

[44] W.A Cooper, J.P Graves, S.P Hirshman, T Yamaguchi, Y Narushima, S Okamura, S Sakakibara, C Suzuki, K.Y Watanabe, H Yamada, and K Yamazaki. Anisotropic pressure bi-Maxwellian distribution function model for three-dimensional equilibria. *Nucl. Fusion*, 46(7) :683–698, July 2006. (Cited on pages 29, 30, 83, and 92.)

[45] J. P. Graves, W. A. Cooper, S. Coda, L.-G. Eriksson, T. Johnson, and JET-EFDA Contributors. Modelling iccd experiments for sawtooth control in jet. *AIP Conference Proceedings*, 871(1) :350–355, 2006. (Cited on page 32.)

[46] Harold Grad. Velocity gradient instability. *Physics of Fluids*, 9(3) :498–513, 1966. (Cited on page 32.)

[47] Allen H. Boozer. Plasma equilibrium with rational magnetic surfaces. *Physics of Fluids*, 24(11) :1999–2003, 1981. (Cited on page 32.)

[48] D.V. Anderson, W.A. Cooper, R.Gruber, S. Merazzi, and U. Schwenn. Methods for the efficient calculation of the mhd stability properties of magnetically confined fusion plasmas. *International Journal of High Performance Computing Applications*, 4(3) :34–47, September 1990. (Cited on page 32.)

[49] R.L. Dewar and S.R. Hudson. Stellarator symmetry. *Physica D : Nonlinear Phenomena*, 112(1–2) :275 – 280, 1998. Proceedings of the Workshop on Time-Reversal Symmetry in Dynamical Systems. (Cited on pages 33 and 75.)

[50] P. Popovich, W. A. Cooper, and L. Villard. A full-wave solver of the Maxwell's equations in 3D cold plasmas. *Comput. Phys. Commun.*, 175(4) :250–263, August 2006. (Cited on pages 34, 43, 44, and 91.)

[51] N. Mellet, W. A. Cooper, P. Popovich, L. Villard, and S. Brunner. Convolution and iterative methods applied to low-frequency waves in 3D warm configurations. *Comput. Phys. Commun.*, 182(3) :570–589, March 2011. (Cited on pages 34 and 91.)

[52] Nicolas Mellet. *Propagation and absorption of low frequency waves in two and three dimensional warm plasmas*. PhD thesis, SB, Lausanne, 2009. (Cited on page 34.)

[53] M. Jucker, J. P. Graves, W. A. Cooper, N. Mellet, T. Johnson, and S. Brunner. Integrated modeling for ion cyclotron resonant heating in toroidal systems. *Comput. Phys. Commun.*, 182(4) :912–925, April 2011. (Cited on pages 34, 35, 36, 37, 38, 51, 92, and 95.)

[54] Martin Jucker. *Self-Consistent ICRH Distribution Functions and Equilibria in Magnetically Confined Plasmas.* PhD thesis, SB, Lausanne, 2010. (Cited on page 34.)

[55] A.H. Boozer and G. Kuo-Petravic. Monte Carlo evaluation of transport coefficients. *Phys. Fluids*, 24(5) :851, 1980. (Cited on pages 36, 82, and 96.)

[56] C. F. Kennel and F. Engelmann. Velocity space diffusion from weak plasma turbulence in a magnetic field. *Physics of Fluids*, 9(12) :2377–2388, 1966. (Cited on page 36.)

[57] T. Johnson, T. Hellsten, and L. G. Eriksson. Analysis of a quasilinear model for ion-cyclotron interactions in tokamaks. *AIP Conf. Proc.*, 787(7) :54–57, July 2005. (Cited on pages 36, 41, 42, 92, and 104.)

[58] Liu Chen, J. Vaclavik, and G.W. Hammett. Ion radial transport induced by icrf waves in tokamaks. *Nuclear Fusion*, 28(3) :389, 1988. (Cited on pages 37, 41, 52, 53, 92, and 95.)

[59] L.-G. Eriksson, M. Mantsinen, D. Borba, a. Fasoli, R. Heeter, S. Sharapov, D. Start, J. Carlsson, a. Gondhalekar, T. Hellsten, and a. Korotkov. Evidence for a Wave-Induced Particle Pinch in the Presence of Toroidally Asymmetric ICRF Waves. *Phys. Rev. Lett.*, 81(6) :1231–1234, 1998. (Cited on pages 41 and 92.)

[60] M. J. Mantsinen, L. C. Ingesson, T. Johnson, V. G. Kiptily, M.-L. Mayoral, S. E. Sharapov, B. Alper, L. Bertalot, S. Conroy, L.-G. Eriksson, T. Hellsten, J.-M. Noterdaeme, S. Popovichev, E. Righi, and A. A. Tuccillo. Controlling the profile of ion-cyclotron-resonant ions in jet with the wave-induced pinch effect. *Phys. Rev. Lett.*, 89 :115004, Aug 2002. (Cited on pages 41 and 92.)

[61] R. Maggiora, G. Vecchi, V. Lancellotti, and V. Kyrytsya. Efficient 3d/1d self-consistent integral-equation analysis of icrh antennae. *Nuclear Fusion*, 44(8) :846, 2004. (Cited on page 42.)

[62] M Brambilla. Numerical simulation of ion cyclotron waves in tokamak plasmas. *Plasma Physics and Controlled Fusion*, 41(1) :1, 1999. (Cited on page 42.)

[63] R.J. Dumont and D. Zarzoso. Heating and current drive by ion cyclotron waves in the activated phase of iter. *Nuclear Fusion*, 53(1) :013002, 2013. (Cited on pages 42 and 95.)

[64] A. Kaye, T. Brown, V. Bhatnagar, P. Crawley, J. Jacquinot, R. Lobel, J. Plancoulaine, P.-H. Rebut, T. Wade, and C. Walker. Present and future jet icrf antennae. *Fusion Engineering and Design*, 24(1) :1 – 21, 1994. (Cited on page 45.)

[65] J.W. Connor and J.G. Cordey. Effects of neutral injection heating upon toroidal equilibria. *Nuclear Fusion*, 14(2) :185, 1974. (Cited on page 49.)

[66] V.P. Bhatnagar, D.F.H. Start, J. Jacquinot, F. Chaland, A. Cherubini, and F. Porcelli. Local magnetic shear control in a tokamak via fast wave minority ion current drive : theory and experiments in jet. *Nuclear Fusion*, 34(12) :1579, 1994. (Cited on page 49.)

[67] M. N. Bussac, R. Pellat, D. Edery, and J. L. Soule. Internal kink modes in toroidal plasmas with circular cross sections. *Phys. Rev. Lett.*, 35 :1638–1641, Dec 1975. (Cited on page 54.)

[68] B.B. Kadomtsev. Disruptive instability in tokamaks. *Soviet Journal of Plasma Physics*, 1 :389–391, 1975. (Cited on page 54.)

[69] S. von Goeler, W. Stodiek, and N. Sauthoff. Studies of internal disruptions and $m = 1$ oscillations in tokamak discharges with soft—x-ray tecniques. *Phys. Rev. Lett.*, 33 :1201–1203, Nov 1974. (Cited on page 54.)

[70] R.J. Buttery, T.C. Hender, D.F. Howell, R.J. La Haye, S. Parris, O. Sauter, C.G. Windsor, and JET-EFDA Contributors. On the form of ntm onset scalings. *Nuclear Fusion*, 44(5) :678, 2004. (Cited on page 54.)

[71] I.T. Chapman, R.J. Buttery, S. Coda, S. Gerhardt, J.P. Graves, D.F. Howell, A. Isayama, R.J. La Haye, Y. Liu, P. Maget, M. Maraschek, S. Sabbagh, O. Sauter, the ASDEX Upgrade, DIII-D, HL-2A, JT-60U, MAST, NSTX, TCV, Tore Supra Teams, and JET-EFDA Contributors. Empirical scaling of sawtooth period for onset of neoclassical tearing modes. *Nuclear Fusion*, 50(10) :102001, 2010. (Cited on page 54.)

[72] D. J. Campbell, D. F. H. Start, J. A. Wesson, D. V. Bartlett, V. P. Bhatnagar, M. Bures, J. G. Cordey, G. A. Cottrell, P. A. Dupperex, A. W. Edwards, C. D. Challis, C. Gormezano, C. W. Gowers, R. S. Granetz, J. H. Hammen, T. Hellsten, J. Jacquinot, E. Lazzaro, P. J. Lomas, N. Lopes Cardozo, P. Mantica, J. A. Snipes, D. Stork, P. E. Stott, P. R. Thomas, E. Thompson, K. Thomsen, and G. Tonetti. Stabilization of sawteeth with additional heating in the jet tokamak. *Phys. Rev. Lett.*, 60 :2148–2151, May 1988. (Cited on page 54.)

[73] J. P. Graves, I. Chapman, S. Coda, L.-G. Eriksson, and T. Johnson. Sawtooth-control mechanism using toroidally propagating ion-cyclotron-resonance waves in tokamaks. *Phys. Rev. Lett.*, 102 :065005, Feb 2009. (Cited on pages 55 and 56.)

[74] F Porcelli, D Boucher, and M N Rosenbluth. Model for the sawtooth period and amplitude. *Plasma Physics and Controlled Fusion*, 38(12) :2163, 1996. (Cited on pages 55 and 58.)

[75] J P Graves, M Lennholm, I T Chapman, E Lerche, M Reich, B Alper, V Bobkov, R Dumont, J M Faustin, P Jacquet, F Jaulmes, T Johnson, D L Keeling, Yueqiang Liu, T Nicolas, S Tholerus, T Blackman, I S Carvalho, R Coelho, D Van Eester, R Felton, M Goniche, V Kiptily, I Monakhov, M F F Nave, C Perez von Thun, R Sabot, C Sozzi, and M Tsalas. Sawtooth control in jet with iter relevant low field side resonance ion cyclotron resonance heating and iter-like wall. *Plasma Physics and Controlled Fusion*, 57(1) :014033, 2015. (Cited on page 55.)

Bibliographie

[76] J.P. Graves, I.T. Chapman, S. Coda, M. Lennholm, M. Albergante, and M. Jucker. Control of magnetohydrodynamic stability by phase space engineering of energetic ions in tokamak plasmas. *Nat. Commun.*, 3 :624, January 2012. (Cited on page 55.)

[77] R.V. Budny, M.G. Bell, H. Biglari, M. Bitter, C.E. Bush, C.Z. Cheng, E.D. Fredrickson, B. Grek, K.W. Hill, H. Hsuan, A.C. Janos, D.L. Jassby, D.W. Johnson, L.C. Johnson, B. Le-Blanc, D.C. McCune, D.R. Mikkelsen, H.K. Park, A.T. Ramsey, S.A. Sabbagh, S.D. Scott, J.F. Schivell, J.D. Strachan, B.C. Stratton, E.J. Synakowski, G. Taylor, M.C. Zarnstorff, and S.J. Zweben. Simulations of deuterium-tritium experiments in tftr. *Nuclear Fusion*, 32(3) :429, 1992. (Cited on page 56.)

[78] S.D. Pinches, L.C. Appel, J. Candy, S.E. Sharapov, H.L. Berk, D. Borba, B.N. Breizman, T.C. Hender, K.I. Hopcraft, G.T.A. Huysmans, and W. Kerner. The hagis self-consistent nonlinear wave-particle interaction model. *Computer Physics Communications*, 111(1) :133 – 149, 1998. (Cited on page 56.)

[79] I. T. Chapman, S. E. Sharapov, G. T. A. Huysmans, and A. B. Mikhailovskii. Modeling the effect of toroidal plasma rotation on drift-magnetohydrodynamic modes in tokamaks. *Physics of Plasmas*, 13(6), 2006. (Cited on page 56.)

[80] W.A. Cooper. Private communication. (Cited on page 58.)

[81] Lyman Spitzer. The stellarator concept. *Physics of Fluids*, 1(4) :253–264, 1958. (Cited on page 59.)

[82] Allen H. Boozer. What is a stellarator ? *Physics of Plasmas*, 5(5) :1647–1655, 1998. (Cited on page 60.)

[83] D. Palumbo. Some considerations on closed configurations of magnetohydrostatic equilibrium. *Il Nuovo Cimento B (1965-1970)*, 53(2) :507–511, 1968. (Cited on page 60.)

[84] M. P. Bernardin, R. W. Moses, and J. A. Tataronis. Isodynamical (omnigenous) equilibrium in symmetrically confined plasma configurations. *Physics of Fluids*, 29(8) :2605–2611, 1986. (Cited on page 60.)

[85] John R. Cary and Svetlana G. Shasharina. Omnigenity and quasihelicity in helical plasma confinement systems. *Physics of Plasmas*, 4(9) :3323–3333, 1997. (Cited on page 60.)

[86] D. A. Garren and A. H. Boozer. Existence of quasihelically symmetric stellarators. *Physics of Fluids B*, 3(10) :2822–2834, 1991. (Cited on page 60.)

[87] B.E. Nelson, R.D. Benson, L.A. Berry, A.B. Brooks, M.J. Cole, P.J. Fogarty, P.L. Goranson, P. Heitzenroeder, S.P. Hirshman, G.H. Jones, J.F. Lyon, P.K. Mioduszewski, D.A. Monticello, D.A. Spong, D.J. Strickler, A.S. Ware, and D.E. Williamson. Design of the quasi-poloidal stellarator experiment (qps). *Fusion Engineering and Design*, 66–68 :205 – 210, 2003. 22nd Symposium on Fusion Technology. (Cited on page 60.)

[88] F. Brochard. Physics and engineering design of estell quasi-axisymmetric stellarator. *41st EPS Conf. on Plasma Phys. (Berlin, 23-27 June 2014) Europhys. Conf. Abstracts (ECA)*, 38F(ECA) :2.081, 2014. (Cited on page 61.)

[89] M. Drevlak, F. Brochard, P. Helander, J. Kisslinger, M. Mikhailov, C. Nührenberg, J. Nührenberg, and Y. Turkin. Estell : A quasi-toroidally symmetric stellarator. *Contributions to Plasma Physics*, 53(6) :459–468, 2013. (Cited on page 61.)

[90] J. N. TALMADGE, F. S. B. ANDERSON, D. T. ANDERSON, C. DENG, W. GUTTENFELDER, K. M. LIKIN, J. LORE, J. C. SCHMITT, and K. ZHAI. Experimental tests of quasisymmetry in hsx. *Plasma and Fusion Research*, 3 :S1002–S1002, 2008. (Cited on page 61.)

[91] J. Nührenberg and R. Zille. Quasi-helically symmetric toroidal stellarators. *Physics Letters A*, 129(2) :113 – 117, 1988. (Cited on page 61.)

[92] W Lotz, J Nührenberg, and C Schwab. Optimization, mhd mode and alpha particle confinement behaviour of helias equilibria. In *Proc. 13th Int. Conf. on Plasma Phys. and Controlled Nucl. Fusion Research*, page 603, 1990. (Cited on page 61.)

[93] C.D. Beidler, E. Harmeyer, F. Herrnegger, Yu. Igitkhanov, A. Kendl, J. Kisslinger, Ya.I. Kolesnichenko, V.V. Lutsenko, C. Nührenberg, I. Sidorenko, E. Strumberger, H. Wobig, and Yu.V. Yakovenko. The helias reactor hsr4/18. *Nuclear Fusion*, 41(12) :1759, 2001. (Cited on page 61.)

[94] J Geiger, H Maassberg, and C. D. Beidler. Investigation of Wendelstein 7-X Configurations with Increased Toroidal Mirror. *35th EPS Conference on Plasma Phys. Hersonissos*, 32D :5–8, June 2008. (Cited on page 64.)

[95] M. Drevlak, J. Geiger, P. Helander, and Y. Turkin. Fast particle confinement with optimized coil currents in the W7-X stellarator. *Nuclear Fusion*, 54(7) :073002, 2014. (Cited on pages 64 and 66.)

[96] Y. Turkin, C. D. Beidler, H. Maaßberg, S. Murakami, V. Tribaldos, and A. Wakasa. Neoclassical transport simulations for stellarators. *Physics of Plasmas*, 18(2), 2011. (Cited on pages 64 and 98.)

[97] W Lotz, P Merkel, J Nuehrenberg, and E Strumberger. Collisionless alpha -particle confinement in stellarators. *Plasma Phys. Control. Fusion*, 34(6) :1037–1052, 1992. (Cited on page 66.)

[98] Horst Wobig. Theory of advanced stellarators. *Plasma Phys. Control. Fusion*, 41(3A) :A159–A173, 1999. (Cited on page 66.)

[99] H. E. Mynick. Transport optimization in stellaratorsa). *Physics of Plasmas*, 13(5) :–, 2006. (Cited on page 66.)

[100] J. R. Cary, D.F. Escande, and J.L. Tennyson. Adiabatic-invariant change due to separatrix crossing. *Physical Review A*, 34(5), 1986. (Cited on page 67.)

Bibliographie

[101] D. Pfefferlé, J.P. Graves, W.A. Cooper, C. Misev, I.T. Chapman, M. Turnyanskiy, and S. Sangaroon. Nbi fast ion confinement in the helical core of mast hybrid-like plasmas. *Nuclear Fusion*, 54(6) :064020, 2014. (Cited on pages 70 and 71.)

[102] Mattia Albergante. *Interaction Between Fast Ions and Microturbulence in Thermonuclear Devices.* PhD thesis, SB, Lausanne, 2011. (Cited on page 71.)

[103] D Pfefferlé, J P Graves, and W A Cooper. Hybrid guiding-centre/full-orbit simulations in non-axisymmetric magnetic geometry exploiting general criterion for guiding-centre accuracy. *Plasma Physics and Controlled Fusion*, 57(5) :054017, 2015. (Cited on page 71.)

[104] David Pfefferlé. *Energetic ion dynamics and confinement in 3D saturated MHD configurations.* PhD thesis, SB, Lausanne, 2015. (Cited on page 71.)

[105] Yu. Turkin, H. Maassberg, C. D. Beidler, J. Geiger, and N. B. Marushchenko. Current control by eccd for w7-x. *Fusion Science and Technology*, 50(3) :387–394, October 2006. (Cited on page 77.)

[106] J. Ongena, A. Messiaen, D. Van Eester, B. Schweer, P. Dumortier, F. Durodie, Ye. O. Kazakov, F. Louche, M. Vervier, R. Koch, A. Krivska, A. Lyssoivan, M. Van Schoor, T. Wauters, V. Borsuk, O. Neubauer, O. Schmitz, G. Offermans, Y. Altenburg, C. Baylard, D. Birus, S. Bozhenkov, D. A. Hartmann, J. P. Kallmeyer, S. Renard, R. C. Wolf, and T. Fülöp. Study and design of the ion cyclotron resonance heating system for the stellarator Wendelstein 7-X. *Phys. Plasmas*, 21(6) :061514, June 2014. (Cited on pages 79 and 87.)

[107] J. M. Faustin, W. A. Cooper, J. Geiger, J. P. Graves, and D. Pfefferlé. Applications of the SCENIC code package to the minority ion-cyclotron heating in Wendelstein 7-X plasmas. *AIP Conference Proceedings*, 1689(1), 2015. (Cited on page 80.)

[108] M. Jucker, W.A. Cooper, and J.P. Graves. Integrated modelling of ICRH in a quasi-axisymmetric stellarator. *Nucl. Fusion*, 52(1) :013015, January 2011. (Cited on pages 82 and 83.)

[109] J.M. Faustin, W.A. Cooper, J.P. Graves, D. Pfefferlé, and J. Geiger. Fast particle loss channels in wendelstein 7-x. *Nuclear Fusion*, 56(9) :092006, 2016. (Cited on pages 86 and 98.)

[110] C. T. Hsu and D. J. Sigmar. Alpha-particle losses from toroidicity-induced alfvén eigenmodes. part i : Phase-space topology of energetic particle orbits in tokamak plasma. *Physics of Fluids B*, 4(6) :1492–1505, 1992. (Cited on page 95.)

[111] E. Lerche, M. Goniche, P. Jacquet, D. Van Eester, V. Bobkov, L. Colas, C. Giroud, I. Monakhov, F.J. Casson, F. Rimini, C. Angioni, M. Baruzzo, T. Blackman, S. Brezinsek, M. Brix, A. Czarnecka, K. Crombé, C. Challis, R. Dumont, J. Eriksson, N. Fedorczak, M. Graham, J.P. Graves, G. Gorini, J. Hobirk, E. Joffrin, T. Johnson, Y. Kazakov, V. Kiptily, A. Krivska, M. Lennholm, P. Lomas, C. Maggi, P. Mantica, G. Mathews, M.-L. Mayoral, L. Meneses,

J. Mlynar, P. Monier-Garbet, M.F. Nave, C. Noble, M. Nocente, I. Nunes, J. Ongena, G. Petravich, V. Petrzilka, T. Pütterich, M. Reich, M. Santala, E.R. Solano, A. Shaw, G. Sips, M. Stamp, M. Tardocchi, M. Tsalas, M. Valisa, and JET Contributors. Optimization of icrh for core impurity control in jet-ilw. *Nuclear Fusion*, 56(3) :036022, 2016. (Cited on page 97.)

[112] J M Faustin, W A Cooper, J P Graves, D Pfefferlé, and J Geiger. Icrh induced particle losses in wendelstein 7-x. *Plasma Physics and Controlled Fusion*, 58(7) :074004, 2016. (Cited on pages 98 and 99.)

[113] Gunyoung Park and C. S. Chang. A 5-1/2-dimensional theory for fast and accurate evaluation of the cyclotron resonance heating using a real-space wave representation. *Phys. Plasmas*, 14(5) :052503, 2007. (Cited on page 104.)

[114] Lanthaler S., Graves J. P., and Pfefferlé D. Higher order larmor radius corrections to guiding-centre equations and application to fast ion equilibrium distributions. *to be submitted to Plasma Physics and Controlled Fusion*, 2016. (Cited on page 104.)

Jonathan FAUSTIN

PERSONAL DATA

PLACE AND DATE OF BIRTH:	Versailles, France | 17 May 1988
ADDRESS:	Rue du centre 2 bis, 1025 Saint Sulpice, Suisse
PHONE:	+41 78 841 20 19
EMAIL:	jonathan.faustin@epfl.ch

WORK EXPERIENCE

Current
PhD candidate at the Swiss Plasma Center, Ecole Polytechnique Fédérale de Lausanne, Switzerland
"Self-consistent interaction of fast particles and ICRF waves in 3D applications of fusion plasma devices."

Numerical investigation of the particle distribution function interacting with ICRF waves in tokamak and stellarator plasmas. Assessment of the possible ICRF scheme for fast ion generation in Wendelstein 7-X. Identification of the fast particles loss channels in Wendelstein 7-X under NBI and ICRH conditions.

Advisors: Dr. Jonathan GRAVES and Dr. Anthony COOPER

FEV-SEP 2012
Master thesis at the Iter Organization, Saint Paul lez Durance, France
"Investigation of the pedestal conditions which may lead to small ELM losses."

ITER relevant linear MHD simulations with the equilibrium and edge stability codes HELENA and MISHKA. Investigation of operational regions in which the widths of the most unstable peeling-ballooning modes decrease significantly.

Advisors: Dr. Guido Huijsmans and Dr. Alberto Loarte

FEV-AUG 2011
Engineering work placement at Electricité de France, Villeurbanne, France
"Study of the fretting wear on nuclear fuel rods for Pressurized Water Reactors."

Re-qualification a numerical model used for simulations of the wear phenomenon of nuclear fuel rods. Identification of a relevant indication of the wear risk.

Advisor: Corentin RICHARD

JUN-AUG 2010
Laboratory work placement at the University Cuza, Iasi, Romania
"Diagnostic methods for a magnetron plasma used for thin flim deposition."

Investigation of the plasma parameters influence on the thin film deposition process. Experimental data were obtained with Langmuir probe, emissive probe, optical emission spectroscopy and fast ICCD imaging.

Advisor: Dr. Claudiu COSTIN

EDUCATION

2011 - 2012
Master Degree in FUSION SCIENCES, **Université de Lorraine**, Nancy, France
Courses: MHD stability and equilibrium, plasma heating, energy and particle transport, plasma-wall interactions, numerical methods for fusion.

2008 - 2011
Engineer Degree in NUCLEAR TECHNOLOGIES **Ecole des Mines de Nantes**, Nantes, France
Courses: neutronics, nuclear core simulation with MCNP, nuclear fuel cycle, reactors thermal hydraulics, safety and radiation protection.

2009 - 2010
Erasmus student at **Danmarks Tekniske Universitet**, Lyngby, Denmark
Courses: electromagnetics, quantum mechanics, statistical physics, radioactive isotopes, numerical methods for physicists.

2006 - 2008
Preparatory classes at **Lycée "Leconte de Lisle"**

LANGUAGES

FRENCH:	Mother tongue
ENGLISH:	Professional proficiency
SPANISH:	Basic Knowledge

Computer Skills

Scientific softwares:	MATLAB, MATHEMATICA, MPICH2, HDF5, LaTeX
Programming languages:	FORTRAN, JAVA, C++, PYTHON, BASH

Interests and Activities

Swimming, roller-blading
Ukulele, Guitar
Cooking, Travelling

Scientific publications

First author

- J M Faustin et al. "Fast particles loss channels in Wendelstein 7-X." Accepted for publication in Nuclear Fusion, 2016.

- J M Faustin et al. "ICRH induced particle losses in Wendelstein 7-X." Plasma Physics and Controlled Fusion, 58(7) p.074004, 2016.

Co-author

- W A Cooper et al. "Three-dimensional magnetohydrodynamic equilibrium of quiescent H-modes in tokamak systems." Plasma Physics and Controlled Fusion, vol. 58, num. 6, p. 064002, 2016.

- W A Cooper et al. "Saturated ideak kink/peeling formations described as three-dimensional magnetohydrodynamic tokamak equilibrium states." Physics of Plasmas, vol. 23, num. 4, p. 040701, 2016.

- W A Cooper et al. "Free boundary equilibrium in 3D tokamaks with toroidal rotation." Nuclear Fusion, vol. 55, num. 6, p. 063032, 2015.

- J P Graves et al. "Sawtooth control in JET with ITER relevant low field side resonance ion cyclotron resonance heating and ITER-like wall." Plasma Physics and Controlled Fusion, 57 p.014033, 2014.

- C. Costin et al. "Fast Imaging Investigation on Pulsed Magnetron Discharge", IEEE Transactions on Plasma Science 39, 2011.

Conference proceedings

- J M Faustin et al. "Modelling of ICRF fast ion generation in 2D and 3D plasma configurations", contributed talk at the 43rd European Physical Society conference on Plasma Physics, Leuven, Belgium and conference proceeding, 2016.

- J M Faustin et al. "Self-consistent modelling of plasma heating and fast ion generation using Ion-Cyclotron Range of Frequency waves in 2D and 3D devices", contributed talk at the Platform for Advanced Scientific Computing conference, Lausanne, Switzerland, 2016.

- J M Faustin et al. "Fast ion loss channel in Wendelstein 7-X plasmas", contributed poster at the 20th International Stellarator-Heliotron Workshop, Greifswald, Germany, 2015.

- J M Faustin et al. "ICRH induced particle losses in Wendelstein 7-X", contributed talk at the 597th WEH Seminar on Stochasticity in Fusion Plasmas, Bad Honnef, Germany (2015).

- J M Faustin et al. "Applications of the SCENIC code package to the minority ion-cyclotron heating in Wendelstein 7-X plasmas", contributed poster at the 21st Topical Conference on Radio Frequency Power in Plasmas, Lake Arrowhead, USA and AIP Conference Proceedings, (1689), p.060003, 2015.

- J M Faustin et al. "Modeling of ion-cyclotron resonant heating in Wendelstein 7-X equilibrium", contributed poster at the Theory of Fusion Plasmas conference, Varenna ,Italy, and Journal of Physics Conference Series (561) p.012006, 2014.

- J M Faustin et al. "SCENIC : a self-consistent tool for the study of ion-cyclotron resonance heating in fusion plasma devices", contributed talk at the Swiss Physical Society conference, Fribourg, Switzerland, 2014.

- J M Faustin et al. "SCENIC : a self-consistent tool for the study of ion-cyclotron resonance heating in 3D fusion plasma devices run on a hybrid HPC architecture", contributed poster at the Platform for Advanced Scientific Computing conference, Zürich, Switzerland, 2014.